Master's thesis

NTNU
Norwegian University of Science and Technology
Faculty of Engineering
Department of Mechanical and Industrial Engineering

Endre Verlo Nes

Effect of building orientation on mechanical properties of Ti6Al4V produced with powder bed fusion (PBF-LB/M)

Master's thesis in Mechanical Engineering
Supervisor: Knut Sørby

February 2021

NTNU
Norwegian University of
Science and Technology

Endre Verlo Nes

Effect of building orientation on mechanical properties of Ti6Al4V produced with powder bed fusion (PBF-LB/M)

Master's thesis in Mechanical Engineering
Supervisor: Knut Sørby
February 2021

Norwegian University of Science and Technology
Faculty of Engineering
Department of Mechanical and Industrial Engineering

NTNU
Norwegian University of
Science and Technology

Abstract

Most published literature on testing the effect of build orientations with PBF-LB/M, focus on the difference between horizontal (0°) and vertical (90°) orientations. In this thesis a study with seven build orientations was performed. This was to investigate the effect of different build orientations on mechanical properties of Ti6Al4V built with PBF-LB/M. There were printed specimens in 0°, 15°, 30°, 45°, 60°, 75° and 90° orientations. Two sets of tensile specimens and two sets of Charpy specimens were tested, with a total of 28 specimens. All the tensile tests were machined after printing. Of the Charpy specimens one set was left with an as-built surface and one set was machined. All specimens were heat treated at 850°C to improve mechanical properties. To investigate the fracture surface, SEM was performed.

Test results of tensile specimens showed isotropic yield strength, UTS and elastic modulus with respect to build orientations. The elongation was anisotropic and showed a trend, but statistically the differences could not be differentiated. A similar trend was found in absorbed energy in the Charpy specimens. These trends were not found described in published literature. Literature on pores, microstructure and Melt Pool Boundaries (MPBs) was investigated to explain the obtained results.

Few pores were found on the fracture surfaces. These were mostly spherical and there were no elongated pores due to insufficient melting. The impact of pores on the mechanical properties with respect to build orientation, was found to be insignificant. Based on previous research it is likely that MPBs and columnar prior β-grains are not a deciding factor in the trends observed. The trends observed in elongation and impact toughness could not be explained by the experiments performed and published research. It was therefore concluded that more research is needed.

Sammendrag

De fleste publiserte forskningsartiklene om PBF-LB/M som omhandler effekten av bygningsorienteringer, fokuserer på forskjellen mellom horisontale (0°) og vertikale (90°) bygningsorienteringere. I denne oppgaven ble det utført en studie med syv bygningsorienteringer. Dette ble gjort for å undersøke effekten av ulike bygningsorienteringer på de mekaniske egenskapene til Ti6Al4V bygget med PBF-LB/M. Det ble bygget testeksemplarer i de følgende orienteringene; 0°, 15°, 30°, 45°, 60°, 75° og 90°. Totalt 28 prøver ble testet, fordelt på to sett med strekkprøver og to sett Charpy-prøver. Alle strekkprøvene ble maskinert etter PBF-LB/M produksjonen. Av Charpy-prøvene beholdt ett sett den PBF-LB/M produserte overflaten og ett sett ble maskinert. Alle prøvene ble varmebehandlet ved 850°C for å forbedre de mekaniske egenskapene. For å undersøke bruddoverflaten ble det utført SEM.

Testresultatene fra strekkprøvene viste isotropi for flytegrense, strekkfasthet og elastisitetsmodul. Bruddforlengelsen var anisotropisk og viste en trend, men statistisk kunne ikke forskjellene skilles. Skårslagprøving viste en lignende anisotropisk trend i absorbert energi som den funnet i bruddforlengelsen. Lignende trender ble ikke funnet beskrevet i publisert forskningslitteratur. Som ledd i å forklare de observerte resultatene ble forskningslitteratur med fokus på porer, mikrostruktur og smeltebadgrenser gjennomgått.

Det ble funnet få porer på bruddflatene og disse var hovedsakelig sfæriske. Det ble ikke funnet lange porer som skyldtes utilstrekkelig smelting. Effekten av porene på de mekaniske egenskapene med hensyn til bygningsorientering var ubetydelige. Basert på litteratur er det sannsynlig at smeltebadgrenser og avlange β-korn utgjør en avgjørende faktor i de observerte anisotropiske trendene i bruddforlengelse og slagfasthet. Eksperimentene utført, sammen med publisert litteratur, var ikke nok til å forklare de observerte trendene. Det konkluderes derfor med at det behøves mer forskning på dette feltet.

Acknowledgements

First and foremost I want to give huge thanks to Sandvik Additive Manufacturing, professor Knut Sørby and Even W. Hovig for letting me take part in their ongoing project, and providing me with the test specimens. Moreover, I am deeply thankful for professor Knut Sørby and Even W. Hovig for help, guidance and shearing of knowledge. They have motivated me and helped me enhance my work. Their help has been greatly appreciated and they have been a important resource for this thesis.

Thank you to Dr. Cristian Torres for help and training in SEM, and to him and professor Seyed M. J. Razavi for general help and guidance.

I wish to thank the employees at the workshops at Valgrinda and Perleporten at NTNU for help and equipment.

Last, but not least, I want to express gratitude to my family, friends and colleagues for support and good times while writing this thesis. Thanks for standing by me, bringing joy and keeping my spirits high throughout the prolonged writing sessions. A special thanks to Stine T. Årethun for her immense support and for always checking in on me.

List of Figures

List of Tables

Acronyms

AM Additive Manufacturing. 1, 4

ANOVA Anlysis of variance. vi, 48, 49

DIC Digital Image Correlation. iv, 5, 6

MPBs Melt Pool Boundaries. i, ix, 12–16, 25, 49, 54–56, 58

PBF-LB/M laser-based powder bed fusion of metals. i, ii, iv, 1, 2, 8–10, 12, 13, 16, 18, 25, 27, 49, 57, 58

SEM Scanning Electron Microscope. i–iii, v, 2, 7, 23, 24, 29, 41–43, 45, 50, 58

UTS Ultimate Tensile Strength. i, 6, 8–10, 17, 48, 49, 57, 58

Contents

Chapter 1

Introduction

"Additive Manufacturing (AM)) is a process of joining materials to make parts from 3D model data" [17]. The AM production method increases design freedom, manufacturing flexibility and product customization. It also enables shorter time to market, fast prototyping, direct repair of metallic parts and decreases the traditional economy-of-scale constraints [16]. Laser-based powder bed fusion of metals (PBF-LB/M), often referred to in literature as selective laser melting (SLM), is one of the AM technologies that has received a lot of attention due to its ability to produce geometrical complex metallic structures. One of the challenges in PBF-LB/M is the inability to generate repeatable mechanical properties with different build orientations [14].

PBF-LB/M of Ti6Al4V without post heat treatment is inherently anisotropic. This is due to the formation of martensite (α'), which has preferred slip systems dependent on the build orientation [49]. The martensite is brittle and thus lead to pore ductility and low toughness [6, 7, 28, 46, 50, 51, 54]. Heat treatment above 800°C have shown to completely decompose the martensite, improving the ductility and remove the anisotropy introduced by martensite [14, 45, 54].

With respect to build, PBF-LB/M built Ti6Al4V is influenced by columnar β-grains that occurs because of epitaxial growth [29, 32, 36–40, 42, 52, 54]. These grains become equiaxed and their anisotropy eliminated for temperatures above 995°C, however at the loss of mechanical properties [40, 42, 54]. Kumar et al.[21] found that with the right scanning parameters the effect of columnar β-grains on mechanical properties could be mitigated, without the use of heat treatments.

Most published literature on the effect of build orientations of Ti6Al4V built with AM do consider few orientations, often are only the horizontal (0°) and vertical (90°) orientations considered. In some cases the 45° is also considered. In this thesis the effect of build orientations on mechanical properties is investigated in seven different build orientations. Both tensile and Charpy test are performed in the following build orientations 0°, 15°, 30°, 45°, 60°, 75° and 90°. The specimens are built with the same scan parameters as in Kumar et al. [21] and they are post heat treated at 850°.

The purpose of this thesis is to broaden the understanding of the effect of build orientations in PBF-LB/M of Ti6Al4V. This has been done by examining and presenting published literature on the subject, performing tensile and Charpy tests in the previously mentioned orientations, examining the fracture surface of the tested specimen with Scanning Electron Microscope (SEM) and at the end discussing the results with findings from literature.

Chapter 2

Methodology

2.1 Material and methods

A total of 14 tensile and 14 Charpy specimens were built, in seven different angles, two for each angle: 0°, 15°, 30°, 45°, 60°, 75° and 90°. 0° is horizontal and 90° is parallel with the building direction (vertical). Seven of the Charpy specimens, one of every built angle, were machined. The other seven, were left with an as-built surface. All the 14 tensile specimens were machined. Apart from this, all the samples were treated equally. Problems occurred with the tensile testing machine, causing one of the 30° specimens becoming work hardened. The result for this specimen was therefore discarded. All other tests were performed correctly.

2.1.1 Material

The material was supplied by Sandvik Additive Manufacturing. The chemical composition is provided in table 2.1.

Table 2.1: Chemical composition of the Ti6Al4V

Element	C	N	O	Al	Ti	V	Fe
wt-%	0,009	0,0165	0,109	6,2	89,5	4	0,2

2.1.2 Manufacturing, process parameters

All of the specimens were manufactured in an EOS M290 machine by Sandvik Additive Manufacturing. The process parameters for the machine was chosen by Sandvik Additive Manufacturing and are summarised in table 2.2. They were used together with an alternating bidirectional 67° rotation scan strategy.

Table 2.2: Processing parameters

Laser power [W]	280		Scan velocity [mm/s]	1200
Layer thickness [μm]	30		Hatch spacing [μm]	140
Substrate temperature [°C]	80		Atmosphere	Argon

2.1.3 Post heat treatment

All the specimens were stress relieved in an Argon atmosphere for two hours at 850°C and then air cooled.

2.1.4 Tensile specimens

The dimensions of the tensile specimens are not standard. They are based on the ASTM E8/E8M, but adapted for AM: To minimize the powder usage, the specimens were made as small as possible, without the thickness affecting the results. The ASTM E8/E8M standard was used to get the right ratio between the dimensions (width, height, thickness and radius). The dimensions of the specimens are shown in figure 2.1. To calculate the true area of each specimen, the mean of the measurements was used. This was later used in calculations of the tensile strength. There were no large deviations of the dimension measurements. The measurements can be seen in appendix A.

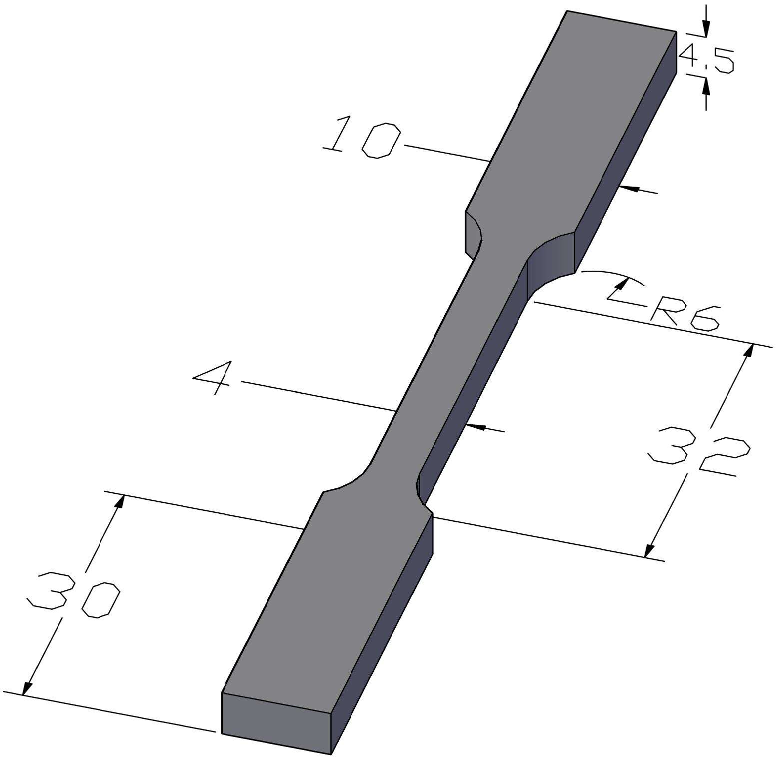

Figure 2.1: Tensile specimen dimensions [mm].

2.1.5 Charpy specimens

The dimensions of the Charpy tests were produced according to the ASTM E23/ISO 148. Dimensions can be seen in figure 2.2. The Charpy specimens were measured with a micrometer to see if there were any large deviations compared to the designed dimensions. There were not found any large deviations, and these results are therefore not discussed any further. The measurements can be seen in appendix A.

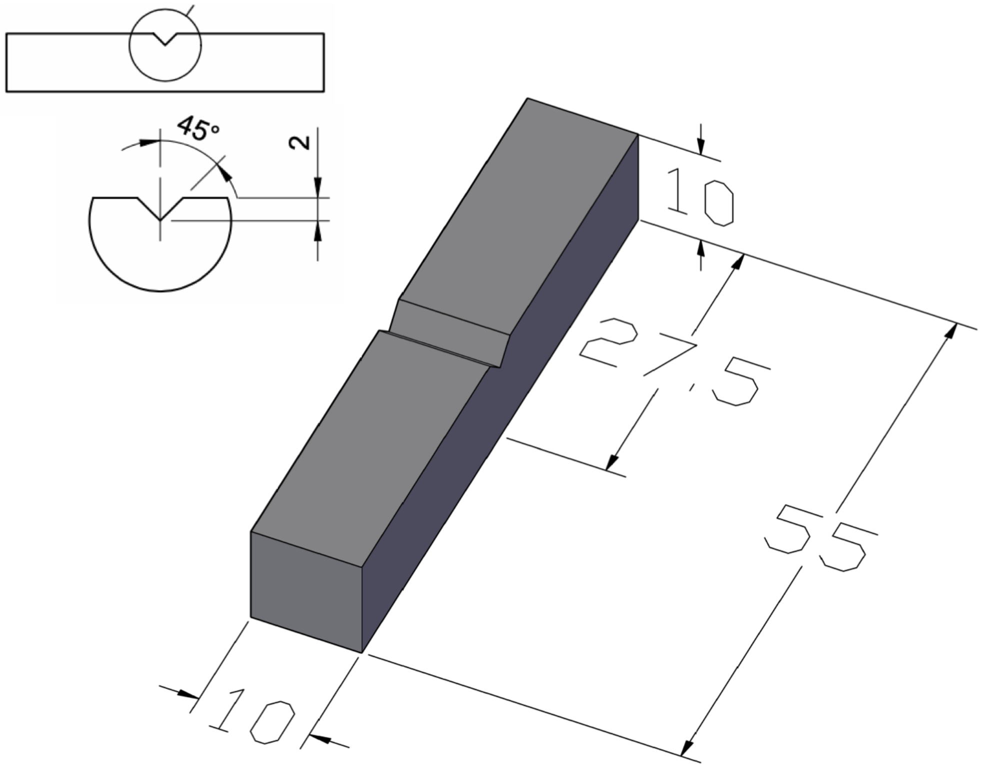

Figure 2.2: Charpy specimen dimensions [mm].

2.2 Mechanical Evaluation

2.2.1 Tensile tests

The tensile test were carried out in an MTS 809 Axial Test System with a 100 kN load cell at room temperature. The machine was set to move at a constant speed of 1 mm per minute.

Digital Image Correlation (DIC)

Along side the tensile tests, DIC system from Vic3D was used to capture the strain. To give a high contrast, white paint was used as background and the spatter pattern was painted black, as seen in figure 2.3. A stereo vision setup was used and focused on two adjacent planes in the 32 mm long section (figure 2.1). The frequency used was one picture every 500 milliseconds (2 Hz). The strain fields used in post-processing with the Vic3D software were two adjacent planes in the 32 mm long section(figure 2.1). The stereo vision system was connected with the data from the tensile test machine. The output file was further post-processed with in-house Matlab scripts provided by Even Wilberg Hovig.

Parameter retrieval

The tensile data was further processed with in-house Matlab scripts. Exactly how the results for the tensile specimens was retrieved is explained in this section. The stress (force/area) data points was filtered with a three data point moving average filter. Then the curve was drawn based on the data.

The elastic modulus data points with stress values between 100 MPa and 700 MPa were sorted out. Just after startup of a tensile test fluctuation (of the force data) may occur. By filtering out the lower range values of the force data, the inaccuracy caused by this fluctuation is avoided. The upper limit was set to ensure that the data would be in the elastic region, and to avoid data from the plastic region to mix in. The data from within the range, was fitted into a linear equation. By definition, the gain of the curve is equal to the elastic modulus [6]. To find the yield strength the same linear equation was used, with an 0.2% offset along the x-axis (strain axis). The yield strength is the intersection between the stress-strain curve and the offset linear curve. By using the maximum data points for load and strain, the UTS and the elongation at break were found.

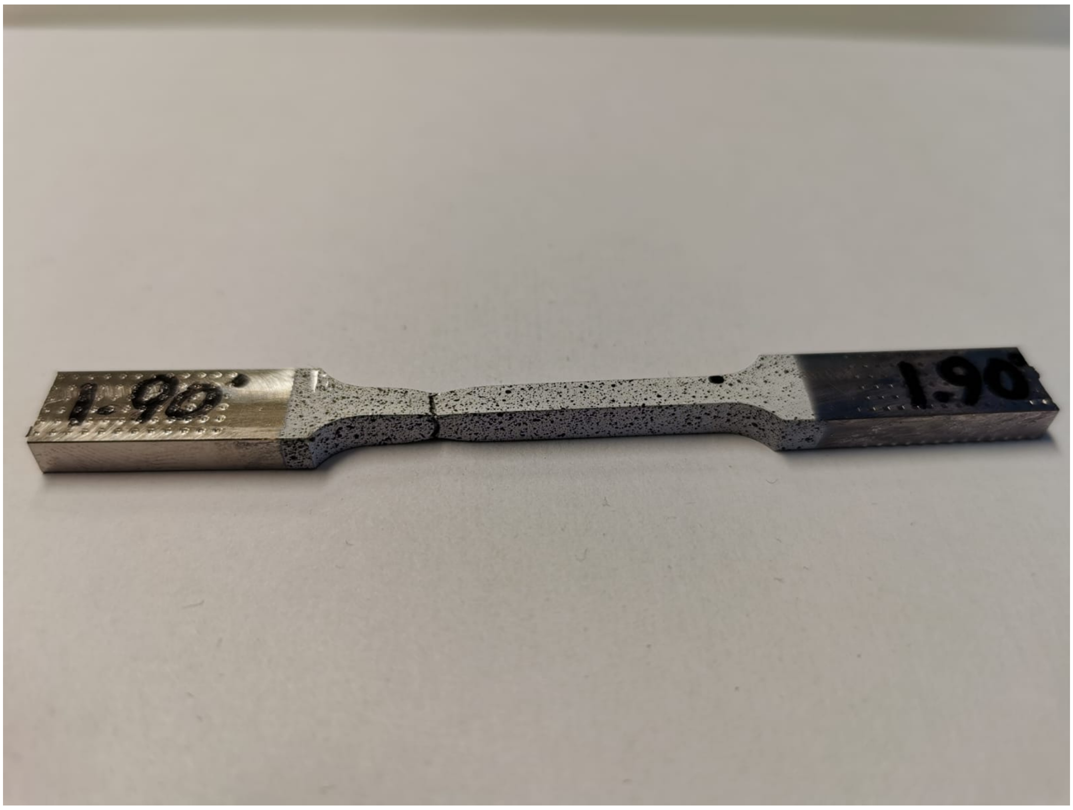

Figure 2.3: The applied DIC pattern.

2.2.2 Charpy tests

The Charpy impact test was carried out according to ASTM E23 with self centring tongs in an Instron MPX450 machine. The initial potential energy of the machines is 450 J. At an initial potential energy of 450 J the Instron MPX450 has a resolution of 0,023 J at an impact energy absorption of 15 J [15].

2.3 Microstructure investigation

The v-notch sizes of the Charpy specimens was investigated with an optical microscope. The fracture surfaces of the tensile and Charpy specimens were investigated by using a Scanning Electron Microscope (SEM), on a Quanta FEG 650 system.

2.4 Roughness measurements

The tensile specimens were produced and machined in the same way as the machined Charpy specimens. It was assumed that they were fairly similar and therefore roughness measurements were collected from the Charpy specimens only. The roughness measurements were conducted with a Mahr Perthometer M2.

Chapter 3

Theory

3.1 Microstructure

AS-built Ti6Al4v PBF-LB/M built parts, without heat treatment, has a microstructure consisting of a fine martensitic (α') needles inside of columnar prior β-grains [40, 42, 49, 54]. The columnar β-grains are oriented parallel to the building direction [29, 32, 36–40, 42, 52, 54].

3.1.1 Martensite (α')

The α' is the hardest and strongest phase in as-built PBF-LB/M Ti6Al4V, but also the most brittle [6, 7, 28, 46, 50, 51, 54]. It leads to high yield strength and UTS, exceeding convectional production methods, but poor ductility (<10% [29]) and toughness [7, 28, 46, 50, 51, 54]. The martensitic microstructure in PBF-LB/M can be attributed to fast solidification and cooling of the melt pool [7, 37, 46, 50, 51, 54]. With a cooling rate of 10^3 and as high as 10^8 [46, 50], the PBF-LB/M process well exceeds the critical cooling rate required for martensitic transformation in Ti6Al4V of 410 K/s [3].

The mechanical properties of the α' is dependent on the crystallographic direction [2, 6, 49]. Some crystallographic directions promotes dislocations more than others [2, 6, 49]. Orientations of the grains to a preferred slip system will therefore promote dislocation movement, which leads to anisotropic behavior [2, 49]. 90° built specimens have been shown to contain a larger number of α' grains in a stress state which are easier to slip than 0° specimens. This leads to anisotropy in the mechanical properties between them [49].

3.1.2 Columnar β-grains

The columnar β-grains can be considered in accounting for some of the mechanical anisotropy seen in PBF-LB/M built parts [32, 54]. They yield higher elongation when load is applied parallel with the grains (90° direction), than perpendicular to the grains (0° direction) [28].

These columnar β-grains occurs because of epitaxial growth [29, 32, 36–40, 42, 52, 54]. This is because of higher thermal gradients in the building direction (directional cooling [42]) and rapid solidification [36, 40, 42, 54], due to the high localized heat from the laser and short laser-powder interaction times [40]. The columnar β-grains can be up to several millimetres in length [31, 37, 40, 43], through successive build layers [32, 37]. This is because the columnar grains from the previously laid layer acts as a nucleus for the grains next layer, leading to epitaxial growth of the strongly textured grains [38]. The width of the columnar grains has been found to closely match the hatch spacing [21, 33, 37, 40, 54].

3.1.3 Effect of heat treatment

The mechanical properties of PBF-LB/M built Ti6Al4V are affected by and differ greatly after various heat treatments [40, 45, 54]. Temperatures from 600°C to 850°C have shown to be effective in decomposition of α' [40, 45]. A temperature of 800°C or above is needed for full decomposition [45, 54]. The heat treatment decomposes the α' needles to a more coarse lamella mixture of α and β [40, 45, 54]. This increases the ductility, but decreases the UTS and yield strength [19, 40]. It was found by Zhang et al.[54] that yield strength declined almost linearly from 800°C to 950°C in correlation with the lamella width. Finer microstructure corresponded to higher yield strength and contributed to micro-crack resistance of the material [54]. Vrancken et al.[40] found that "Post treating at 850°C for 2 h, followed by furnace cooling increased the ductility of PBF-LB/M parts to 12.84 ± 1.36%, compared to 7.36 ± 1.32% for as-built parts". The effect of the cooling rate after 2 h at 850°C on the microstructure was found to be minimal, having small differences between furnace cooling, air cooling and water quenching [40, 54]. For heat treatment above the β transus temperature, or very close to (950°C [38]), the cooling rate becomes important again to avoid reappearance of martensite [38, 40, 42, 54].

While the α' disappear at temperatures above 800°C the columnar β-grains consists until the transus temperature of 995±5°C [38, 40, 42, 54]. Above the β transus temperature the β-grain growth can take place. They become large and equiaxed and the anisotropy of the prior columnar β-grains are eliminated [40, 42, 54].

For heat treatment temperatures below β transus the α and β lamella structure coarsen, but its grain growth is hindered by each other and therefore limited [40, 54]. The residence time and cooling rate is therefore of less importance [40]. For temperatures above or close to β transus, this is not the case and the residence time and cooling rate is therefore of more importance. Longer residence time leads to larger α colony sizes [40, 54]. The α colony sizes are a determining factor for the mechanical properties [40, 54].

Larger α colony sizes gives more slip length which increases the ductility [54]. With increase in temperature up to 850°C the average width of the α+β lamella structure grows slowly, and therefore the specimens still posses a very fine microstructure [54]. The increase in width for the lamella structure and decrease of α phase is more pronounced for temperatures above 900°C [54]. The growth-inhibiting effect becomes weaker and lamellar grains starts to coarsen, thus lowering the elongation at break [54].

The effect of heat treatment temperature on the fracture strain and yield stress for PBF-LB/M built specimens, can be seen in figure 3.1. The drop in yield strength and UTS after heat treatment is due to transition from fine α' to coarser microstructure [40]. With heat treatment above β transus temperature the yield strength decreases with almost no improved ductility [40, 54]. The coarse α structure at the prior β boundaries affect the mechanical continuity within the structure, making it difficult to achieve improved strength and ductility [40, 54]. Both Vrancken et al.[40] and Zhang et al.[54] found that the specimen heat treated at 850 °C for two hours, followed by furnace cooling gave the best overall mechanical properties. The results from Vrancken et al.[40] can be seen in table 3.1. Zhang et al.[54] performed compression tests and the results are therefore excluded.

Table 3.1: Mechanical properties results of 90° tensile specimens heat treated at 850°C for 2 hours and then furnace cooled from Vrancken et al.[40].

E (GPa)	Yield strength (MPa)	UTS (MPa)	Elongation (%)
114.7±3.6	955±6	1004 ±6	12.84 ±1.36

3.1.4 Use of scan parameters

Kumar et al.[21] found that use of the right scanning parameters could mitigate the anisotropy induced by the columnar β-grains, without the use of heat treatments above β transus temperature. With use of the same scanning parameters as in this thesis the columnar prior β grains becomes equiaxed in the horizontal plane (xy-plane, seen in figure 3.2 as the B-plane). The columnar prior β grains in the build direction, seen in figure 3.2 as S-plane, becomes jagged and discontinuous [21]. This irregular arrangement of the prior β-grains in both planes, are because of the slight mismatch between the melt pools from layer to layer due to the 67° rotational scanning (see figure 3.2 b)) [21]. This leads to isotropy in the mechanical properties yield strength and UTS, while some insignificant anisotropy in ductility [21]. Ch et al.[8] also found, with PBF-LB/M of $AlSi_{10}Mg$, that a 67° rotational scanning strategy helps eliminate anisotropy in the mechanical properties and hinder crack propagation along the boundary of elongated grains.

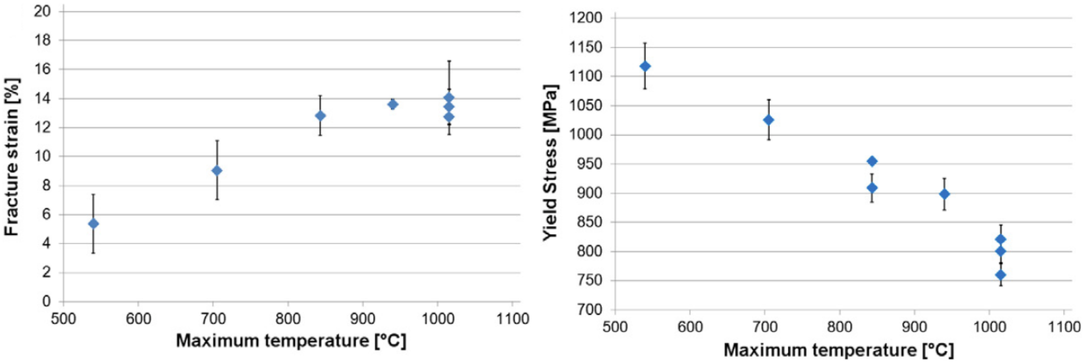

Figure 3.1: The effect of different heat treatment temperatures on the fracture strain and the yield strength [40].

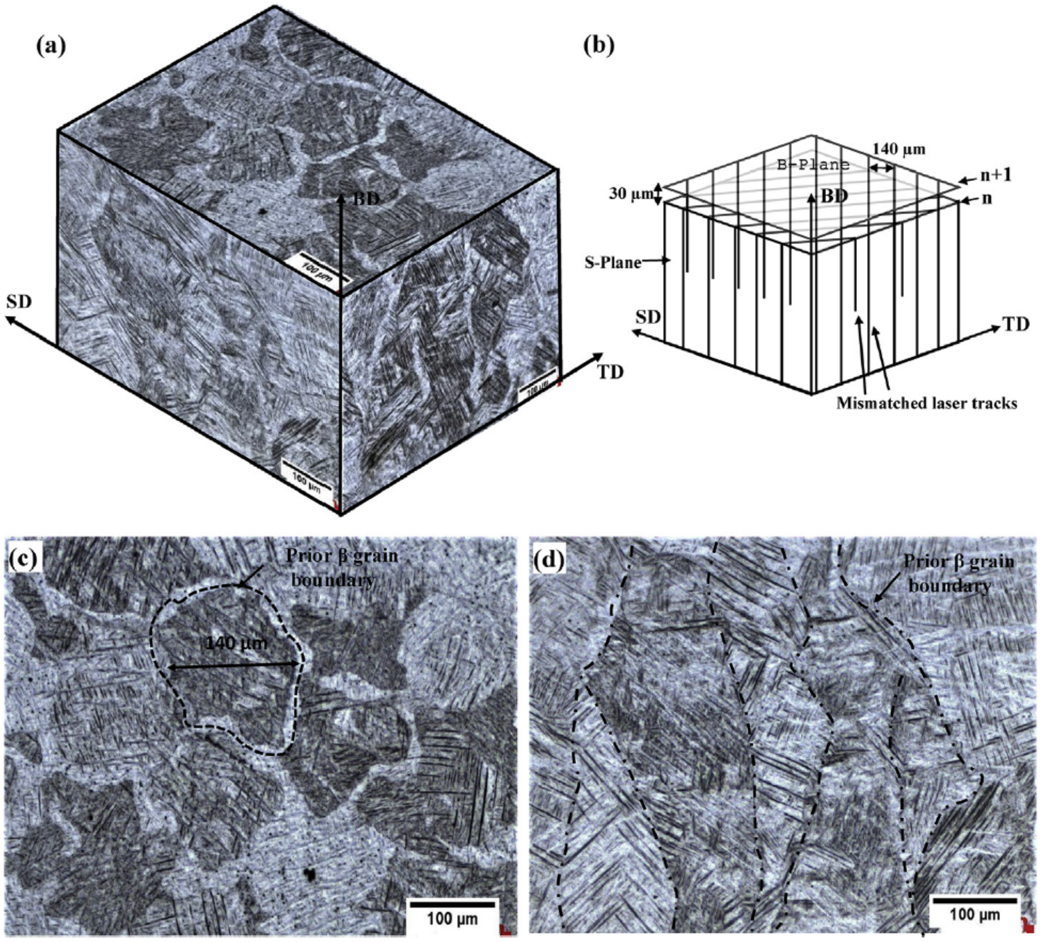

Figure 3.2: "(a) 3D representative microstructure of sample with 30 mm layer thickness and the 67° scan rotation. (b) Schematic representation of the scan rotation of 67° between each successive layer and its effect on the microstructure in B (xy-plane) and S (z-direction) planes. (c) Microstructure of B-plane and (d) microstructure of S-plane. Dashed lines in (c) and (d) are for 'guiding the eye' purpose." [21].

3.2 Melt pool boundaries (MPBs)

As described further in this chapter, MPBs has clearly been seen in Ti6Al4V built with PBF-LB/M by Thijs et al.[37], Kruth et al.[20] and Yadroitsev et al.[47]. It should be mentioned that to the author's knowledge there hasn't been published any specific research on the impact of Melt Pool Boundaries (MPBs) on the mechanical properties in PBF-LB/M with Ti6Al4V. The specific impact of the MPBs described further in the chapter beneath, are therefore researched on other materials, but are still regarded as relevant. An example of this is the much referenced article "Effect of molten pool boundaries on the mechanical properties of selective laser melting parts" by W.Shifeng et al.[30] on 316L stainless.

3.2.1 Creation

"In the PBF-LB/M process, the rapidly moving laser beam scans and melts metal powders, resulting in molten pools (see figure 3.3a). These molten pools have a lower solidification rate and higher temperature gradient at the bottom, hence easily form plane grains. The cross section of these plain grains are the MPBs" [30]. Individual MPBs and the whole MPB interconnected structure, greatly affects the mechanical performance of PBF-LB/M parts [30]. It has significant impact on the microscopic slipping, macroscopic plastic behavior and fracture mode. It is one of the main reasons for anisotropy and low ductility in PBF-LB/M parts [30].

MPBs was seen in Ti6Al4V PBF-LB/M built specimens, as Ti_3Al, due to preferential etching, by Thijs et al.[37], Kruth et al.[20] and Yadroitsev et al.[47]. Kumar et al. [21] also discover the Ti_3Al with X-ray diffraction. In Ti6Al4V segregation of Al occurs at the bottom of the melt pool due to fast solidification [20]. In these Al rich zones Ti_3Al phase precipitates [20].

3.2.2 Form

The form of the MPBs are dependent on the form of the initial melt pool [55]. The behavior of the molten pool is complex [51, 53]. The shape of the melt pool is influenced and sensitive to the scanning speed, laser power, layer thickness and defocusing amount (laser focus) [51, 55]. The height (see figure 3.3b) of the molten pool is closely associated with the layer thickness and is almost unaffected by changes in scan speed an laser power [51]. At the other hand the width and depth (see figure 3.3b) is negligibly affected by the layer thickness [51]. An increase in scan speed leads to an decrease of both melt pool width and depth, while an increase in laser power leads to an increase of both [51]. Between the two processing parameter an increase in the scanning speed is dominant in determining the size of molten pool in comparison with laser power [51].

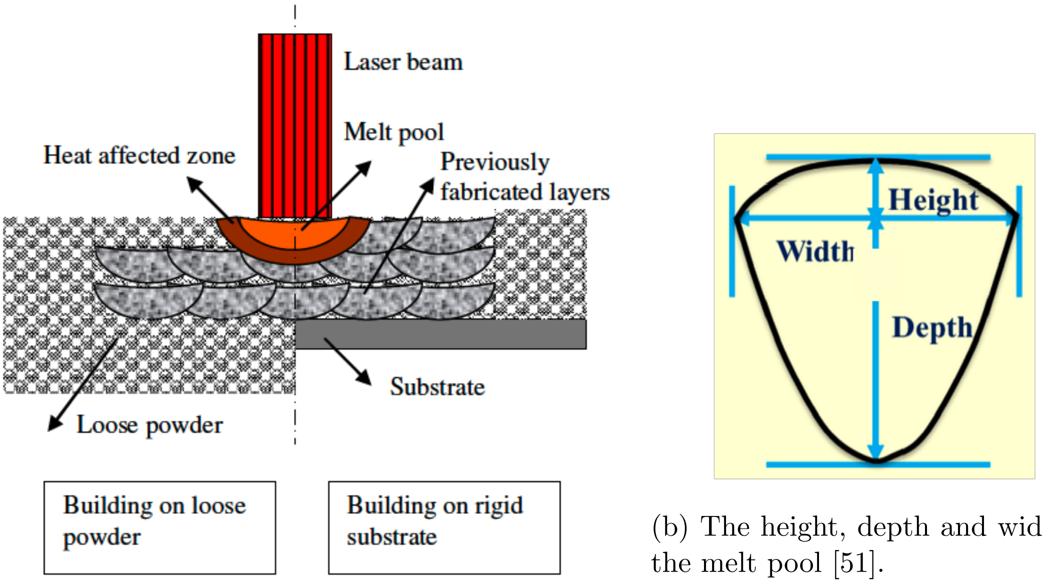

(a) Schematic view showing the melting of powder and previous layers creating a new melt pool and MPBs [20].

(b) The height, depth and width of the melt pool [51].

Figure 3.3

3.2.3 Impact on mechanical properties

Ductile deformation in PBF-LB/M is attributed to slipping of MPBs and grain slip [30, 55]. Slipping along the MPBs preferentially occurs due to the weaker bonding force between the MPBs compared with grain boundaries [30, 55]. MPBs are divided into layer-layer and track-track MPBs [30, 55]. In figure 3.4 the schematic of the two types can be seen.

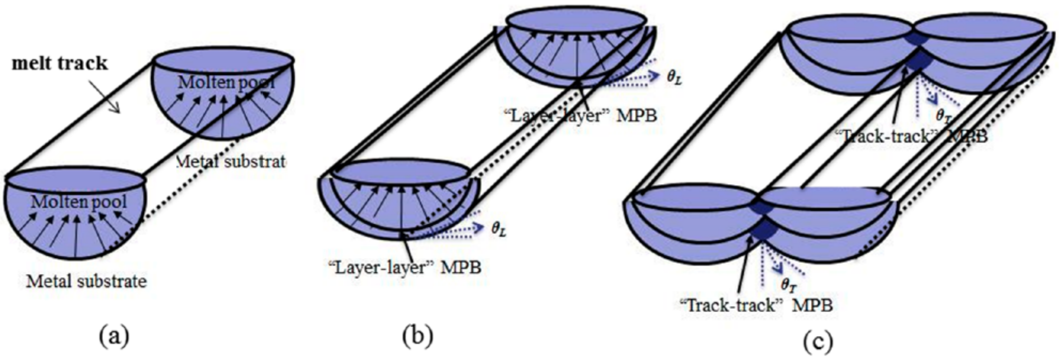

Figure 3.4: Schematic diagram of the crystallization solidification of molten pools during PBF-LB/M process: (a) single half-cylindrical molten pool(the height is not depicted (see figure 3.3b)); (b) layer–layer MPBs; (c) track–track MPBs. The arrows represent the solidification direction [30, 55].

Schmids law (equation 3.1), when solved for the yield stress (equation 3.2), σ_s, can be used to calculate the yield stress needed for slipping [30, 55]. Here θ is the angle between the applied load and the slipping surface, λ is the angel between the applied load and the normal direction of the slip plane.

$$\tau = \sigma cos(\theta) cos(\lambda) \tag{3.1}$$

$$\sigma_s = \frac{\tau_k}{(cos(\theta) cos(\lambda))_{max}} \tag{3.2}$$

Slipping in materials begins when shear stress on the slipping surface reaches a critical value, τ_k [6, 30, 55]. Even though an applied stress is pure tensile, shear components exists at all planes except for planes aligned parallel or perpendicular to the load [6]. The critical shear stress value represent the minimum shear stress required to initiate slip [6]. It mainly depends on the physical and chemical properties of the slipping surface, and is a property that determines when yielding occurs [6, 30, 55]. It is only connected with the interfacial binding force of the slipping surface, regardless of change of the angle of applied loads [30, 55]. Therefore the yield limit, σ_s, only depends on variation of the angle between applied load and slipping surface[30, 55].

Minimum stress necessary for introduce yielding occurs when $\theta = \lambda = 45°$ [6, 30, 55]. This gives a minimal value for σ_s at $\theta = 45°$ of $\sigma_s = 2\tau_k$ [6, 30]. When $\theta = 0°$ or $\theta = 90°$ the shear component goes to zero and σ_s goes to infinity, i.e the slipping surface cannot slip [6, 30].

For 0° tensile specimens the angle between layer-layer MPBs and the loading direction, denoted θ_L (see figure 3.5), is always zero, i.e the MPBs are always parallel with the loading direction [30]. Consequently it is difficult to slip along layer-layer MPBs in 0° specimens [30]. The ductile deformation in 0° specimens is therefore mainly attributed to slipping along track–track MPBs [30]. As both types of MPBs are not strictly planar slipping along both types of MPBs occurs [30]. For 90° specimens this means that the angle between the track-track and the loading direction, denoted θ_T, and θ_L is not strictly 0° and 90° respectively (see figure 3.5) [30]. There is therefore some degree of ductility [30]. For other build orientations the angel between MPBs and loading directions are not 0° and 90°, but varies with the build orientation [30].

As previously mentioned, layer-layer and track-track MPBs are not strictly planer [30]. Theoretical minimum stress when $\theta = 45°$ therefore doesn't match experimental data [30]. Instead experimental results show that maximum elongation occurs when $\theta_T = 30°$ and $\theta_L = 60°$ [30]. Which would correspond to a 60° building orientation. From the maximum the elongation decreases with the change of build orientation [30].

The loading upon MPBs leads to a significant difference in elongation between 0° specimens and the other build orientations [30]. The elongation of 90°, 75°, 60° and 45° specimens are for example much higher than for the 0° specimens [30]. This is due to the different number of slipping surfaces at the loading direction [30].

The number of slipping surfaces is dependent on the hatch spacing and the layer thickness [30]. Spacing between track-track MPBs matches the hatch spacing, while the layer thickness matches the spacing between layer-layerMPBs [30]. The specimens achieve the highest elongation when slipping along both types of MPBs [30, 55]. When loading of the 0° specimens the slipping mainly occurs along the track-track MPBs, while when loading of the 90° specimens the slipping occurs along both types of MPBs [30]. This together with the difference between the layer thickness and hatch spacing (e.g: in this thesis is 30/140) gives 90° specimens more slipping surfaces, leading to higher elongation compared with 0° specimens [30].

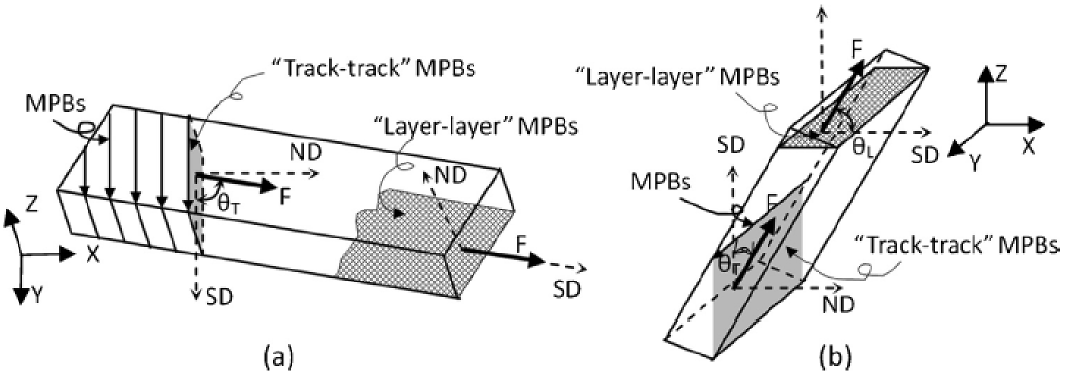

Figure 3.5: "The force analysis diagram of MPBs: (a) produced in horizontal direction; (b) produced in vertical direction, where, ND-normal direction, SD-slipping direction, θ_T-the angle between tensile load and "track–track" MPBs slipping surface, θ_L– the angle between tensile load and "layer–layer" MPBs slipping surface"[30].

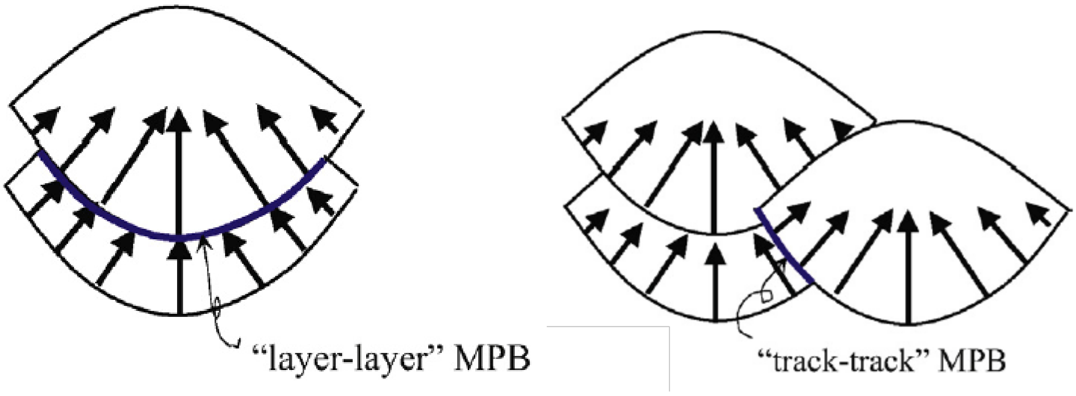

(a) Layer-layer melt pools[30]

(b) Track-track melt pools[30]

Figure 3.6

In AlSi10Mg MPBs are the weakest and softest region of the material [1, 44]. Cracks follow the weaker regions in the material, and tears along the MPBs [1, 44]. The elongation is therefore determined by the fraction of MPBs withstanding load, which Xiong et al.[44] was found to be 0° <45° <90° built specimens, and leading to lower elongation in the same order (largest elongation for 0° specimens).The same was found by Buchbinder et al. [5] between 0° and 90° specimens, for the same reasons. This contradicts the findings of Shifeng et al. [30] on 316L stainless, where the elongation of the 90° specimen was much larger than the 0° specimen.

3.2.4 Effect of heat treatment

It should be mentioned that for Yadroitsev et al.[47] the MPBs was seen clearly in as-built specimens, but could not be observed after heat treatment at 800-960°C. Here it should be mentioned that Yadroitsev et al.[47] also used etching (Kroll's reagent), which for Thijs et al.[37] and Kruth et al.[20] was seen due to preferential etching of the Ti_3Al phase.

3.3 Pores

In this thesis the terms porosity and pores will be used when describing void defects generated during PBF-LB/M manufacturing process. The presence of porosities have been shown to have a strong impact on mechanical properties [4, 11, 18, 34, 38, 39]. Even with low volume fractions, influence of pores have been confirmed [34, 39].

Pores makes prints less ductile and more brittle [34]. They become stress concentrations which leads to failure [34, 38]. Cracks preferentially goes through the network of pores and propagates along the alignment of them [34]. There are various types of pore defects, but the most common are spherical entrapped gasses (Figure 3.7b)) and elongated pores (Figure 3.7a)) [34, 38]. Spherical entrapped gasses will from now be referred to as spherical pores.

The influence of pores on the mechanical properties are dependent on their morphology and size [6, 11, 18, 38, 39]. The influence of spherical pores on mechanical properties are expected to be independent of the loading direction [18]. Their morphology makes it indifferent in which direction they are pulled upon [18]. Spherical pores does not become critical until the material starts to yield and the cross sectional area shrinks [38]. The size of the defects then becomes significant to the cross sectional area, and becomes an area of stress concentrations. Finally the stress becomes higher than the UTS and the specimen fails [34, 38].

Elongated pores are much more detrimental to the mechanical properties than spherical pores, due to sharp rims and crack tips that results in areas of high stress concentration [11, 18, 38]. Elongated pores perpendicular to the loading direction are pulled in a way that opens them up at relatively low stress levels. When elongated pores are oriented parallel with the loading direction they are not as detrimental, because they are closed when pulled upon [34, 38]. This makes the influence of elongated pores on mechanical properties depend on the pores orientation with respect to the loading direction [18, 38]. This can lead to anisotropy in mechanical properties of different building directions [38].

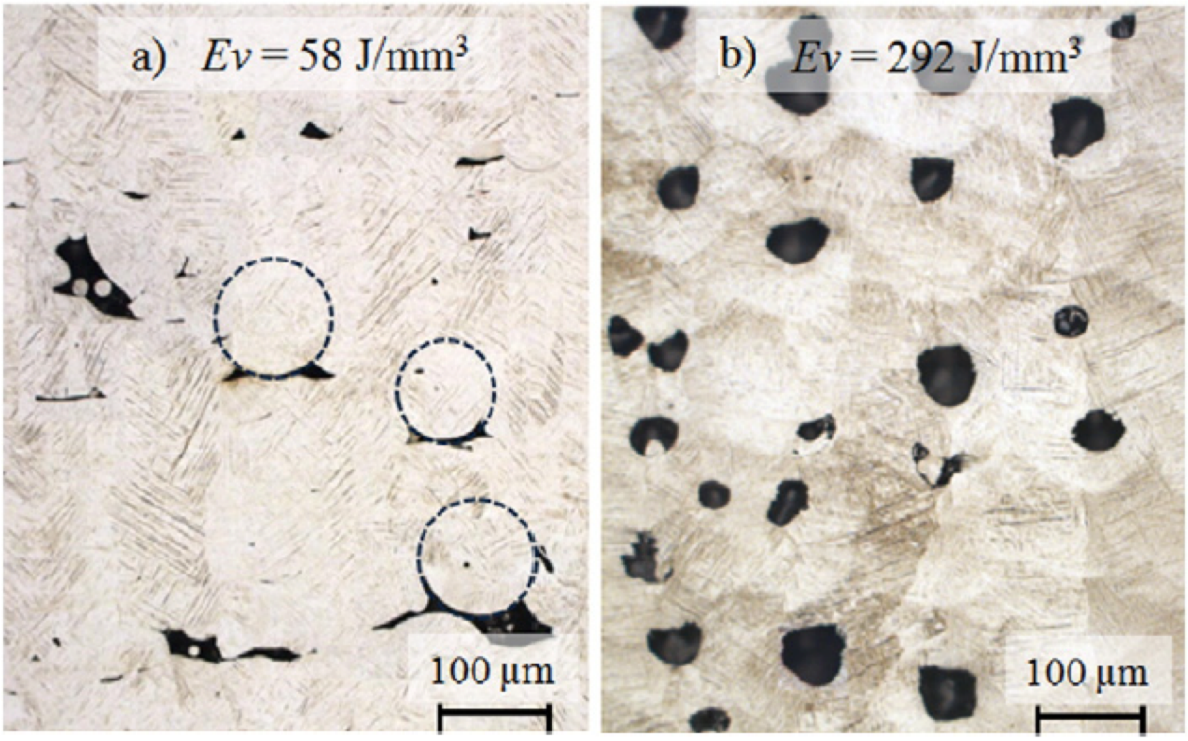

Figure 3.7: a) Example of elongated pores (look away from the dotted circles). b) Example of spherical pores [18].

The formation of pores are correlated to the energy density (figure 3.8) [4, 9, 11, 18, 34], E_v:

$$E_v = \frac{P}{v \cdot l \cdot h} \tag{3.3}$$

Where P is laser power (W), v is scan speed (mm/s), h is hatch spacing (mm) and t is layer thickness (mm) [11, 18, 34].

At high energy densities there are a large amount of pores, mainly spherical (figure 3.8) [11, 18]. Spherical pores can be created in the following ways:

1) Insert gas entrapped in between the powder particles becomes dissolved in the melting pool, and are then trapped due to the high cooling rate of the PBF-LB/M process [11, 18, 38].

2) High temperatures in the melting pool due to a high energy density, leads to high solubility of gas in the liquid metal which are released on solidification [18, 38].

3) Metal gas evaporates by high energy density due to high laser intensity, which leads to pores when the metal is quickly solidified [9, 11, 18].

4) The break up of the melt pool into small spheres, called the balling effect [4, 18].

At lower energy density the number of pores are fewer (figure 3.8), but most of them are of the elongated type [11, 18]. These elongated pores mostly occurs because insufficient melting (lack of fusion) between layers. This is due to low laser power and/or high scan velocity [11, 18, 34, 38]. Insufficient melting occurs due to improper optimization of process parameters or an inhomogeneous powder bed [38]. Elongated pores due to insufficient melting can be recognized by that unmelted powder particles observable near the pores [14]. They are typical in additive manufacturing [34, 38] and much bigger than spherical pores [11, 38].

Elongated pores due to lack of fusion are oriented with their elongated part perpendicularly to the build direction [11, 18, 34, 38]. This preferred orientation of the elongated pores can lead to anisotropy in specimens with respect to their building direction. Especially for the difference between the 0° and 90° specimens. Since the 90° orientation is loaded perpendicular, and the 0° orientation is loaded parallel to the elongated pores [4, 38, 41].

To counteract elongated pores due to insufficient melting the "thickness of the powder bed can be reduced in order to melt less powder particles, but more previously solidified material, enhancing the bonding between layers." [38]. While steps to remove porosity can be made, the total removal of all pore defects are difficult and a minimum of porosity is expected at an intermediate energy density (figure

3.8) [18, 34]. Densities slightly higher than for minimum volume fraction of porosity is recommended to avoid elongated pores due to insufficient melting [18]. This increases the occurrence of spherical pores, but avoids the presence of the elongated flat crack-like pores [18].

There should be mentioned that it has been found a systematic occurrence of elongated pores parallel to the building direction (perpendicular to the horizontal direction) [39]. A high concentration of pores occurs at the laser turn-around point, where the laser slows downs and turns off [39]. At this point, when the laser turns off, the melt pool collapses and freezes due to the fast solidification, which leaves elongated pores parallel with the building direction [39]. These elongated pores opens up when horizontally built specimens are loaded, and closes when vertically built specimens are loaded [39].

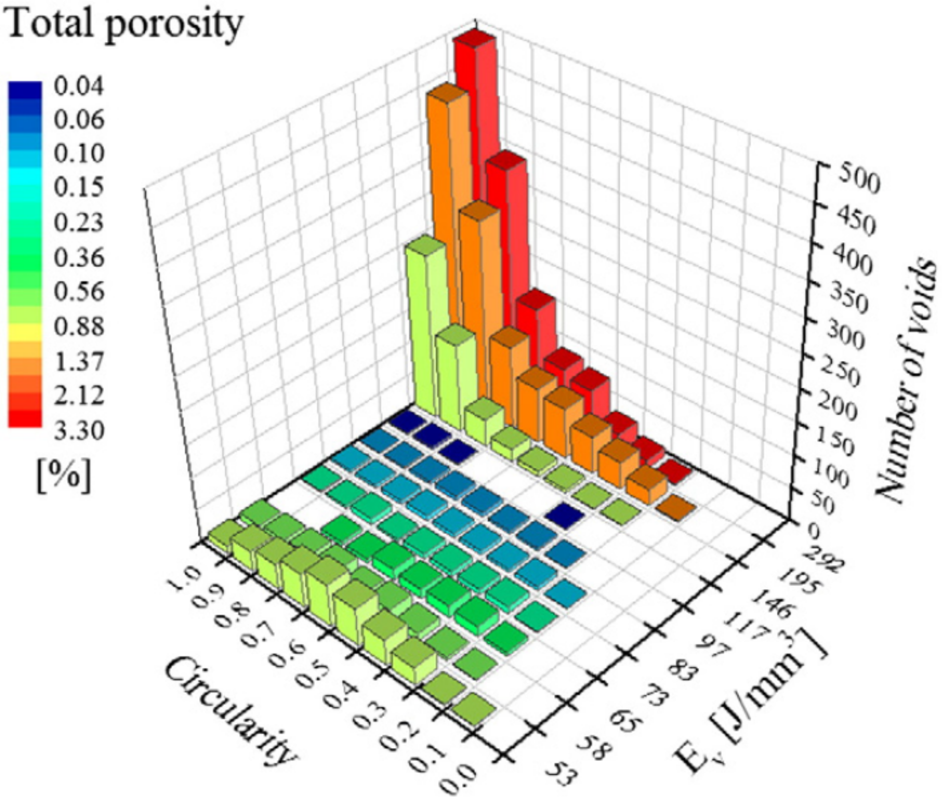

Figure 3.8: Number of pores (voids=pores) and their morphology with different energy densities [18]. Spherical pores are considered as those with sphericity > 0.7 [18].

There is a strong correlation between scan strategy and pore distribution [34]. The pore distribution is closely linked to the scanning strategy. It has the same pattern as the scanning strategy (follows the laser path) [34, 39]. The length of the individual laser scan track also increases the probability of pores [34]. Yan et al.(2018)[48] found that a heat treatments does not significantly affect the number of pores or their size.

3.4 Fractography

3.4.1 Ductile and brittle fracture

There are two types of fracture, brittle and ductile [6, 26]. Brittle fracture is undesirable as it can lead to complete failure of the material very rapid, when a critical load is reached, with no notice in advance [26]. Ductile fracture is often a more stable and more predictable mode of fracture [26]. A distinct feature of a ductile fracture surface is the spherical dimples as shown in figure 3.9 [6, 12, 26]. Narrow and deep dimples indicate very ductile materials, while shallow and wide dimples are produced in less ductile materials [12]. On the other hand, brittle material fractures without any appreciable deformation, and the fracture surface lacks the dimples as seen in ductile fractures [6, 12, 26].

In ductile fractures the stress to initiate a crack is lower than the stress needed to grow it [26]. The crack becomes more difficult to grow as it becomes larger, until it reaches a critical size that is necessary to cause complete failure [26]. In brittle fractures the stress to initiate the crack is higher than the stress needed to grow the crack [26]. After the crack initiation the crack propagates quickly through the material, leading to complete failure [26].

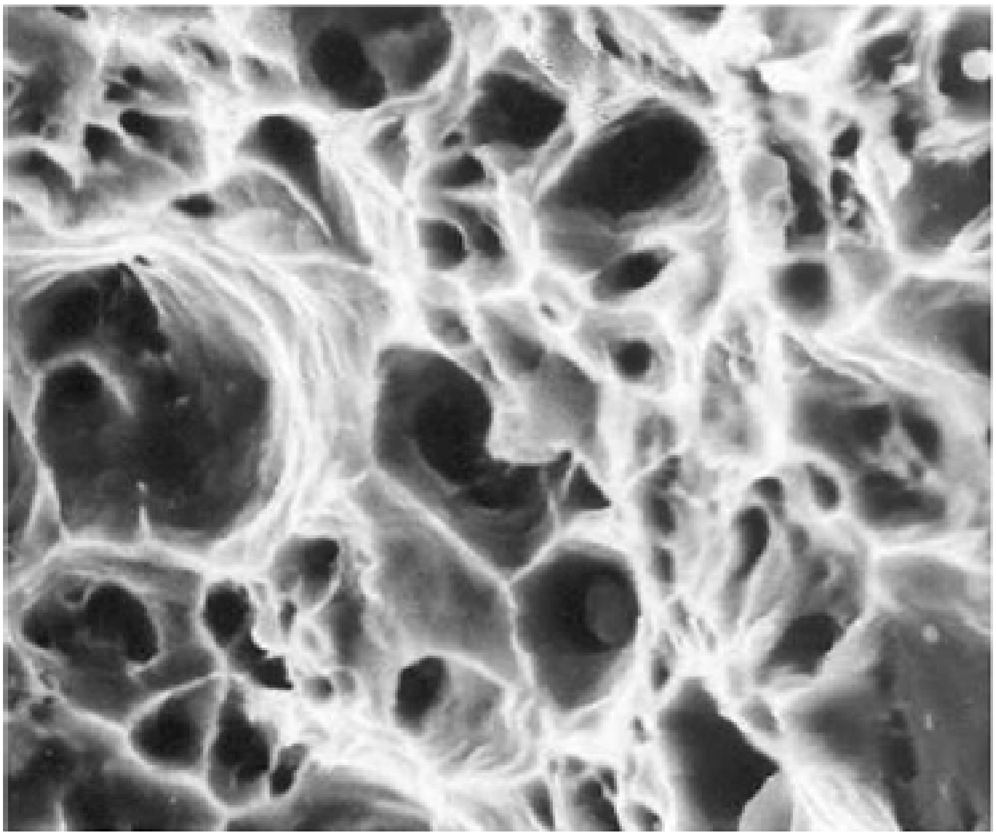

Figure 3.9: Example of ”deep dimples in a very ductile material” [12].

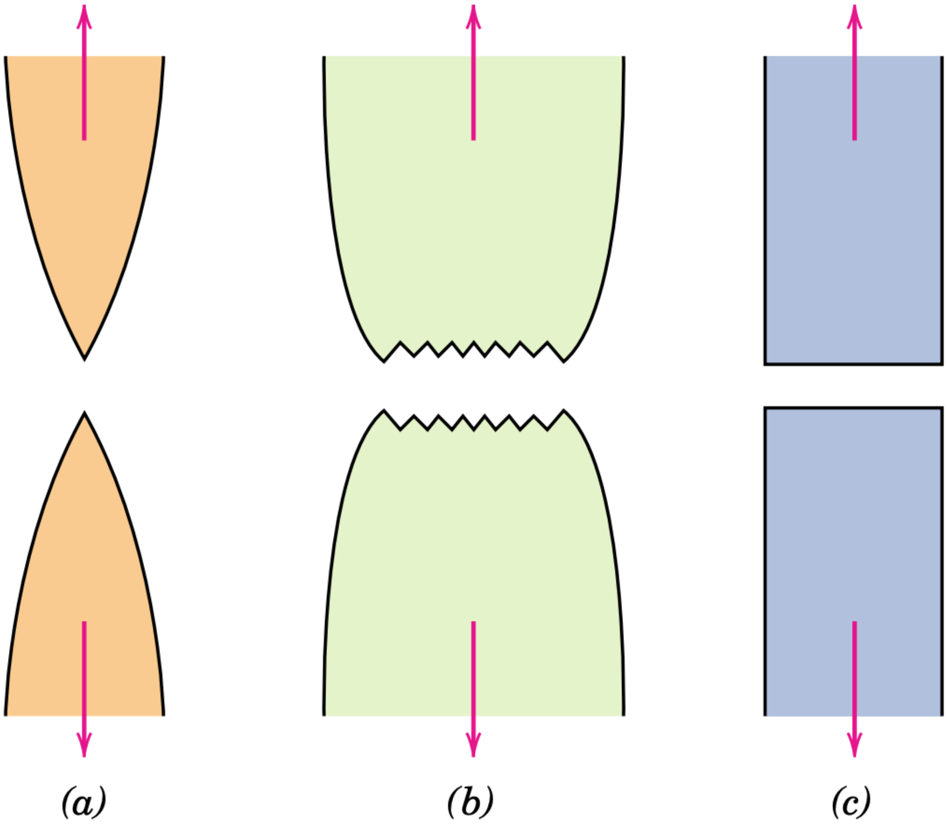

Figure 3.10: "a) Highly ductile fracture where the specimen necks down to a point. b) Moderate ductile fracture after some necking. c) Brittle fracture without any plastic deformation" [6].

When ductile materials are subjected to tensile testing one region of the specimen plastically deforms more than the other [6, 12, 26]. The local cross-sectional area at this region decreases and a neck is formed, as seen in figure 3.10 [6, 12, 26]. The amount of necking depends on the ductility of the material [6]. Most ductile materials have an moderate amount of necking, as shown in figure 3.10 b) [6]. Brittle materials have no appreciable deformation, as seen in figure 3.10 c) [6, 12, 26].

Crack growth in ductile metals can occur in several ways, depending on the type of material and the applied stress conditions [26]. Two important types of a fracture processes are the formation of microscopic cracks and growth, and coalescence of microvoids [26]. When subjected to a tensile test, and leading up to the ductile fracture, the following sequence typically occurs [6, 12]:
First the tensile specimen undergoes uniform deformation [12]. Then, when the specimen reaches the maximum stress on the stress-strain curve, the formation of a neck begins [6, 12]. Once necking begins, a triaxial stress state is induced in the midsection of the cross-sectional area, inducing nucleation of voids [12]. These small cavities, or microvoids, form in the interior of the cross section [6, 12]. As the deformation continues, these microvoids grow under action of stress [12, 26], by plastic deformation [12]. The microvoids enlarge, until they coalesce and link up with the main crack causing it to grow and form an internal cavity (figure 3.11 c))

[6, 12, 26]. Toward the end, the fracture ensues by shear deformation at an angle approximately about 45°, the direction of maximum shear stress [6, 12]. This creates shear lips [6, 12]. Schematics of the fracture stages of a ductile fracture with shear lips are shown in figure 3.11.

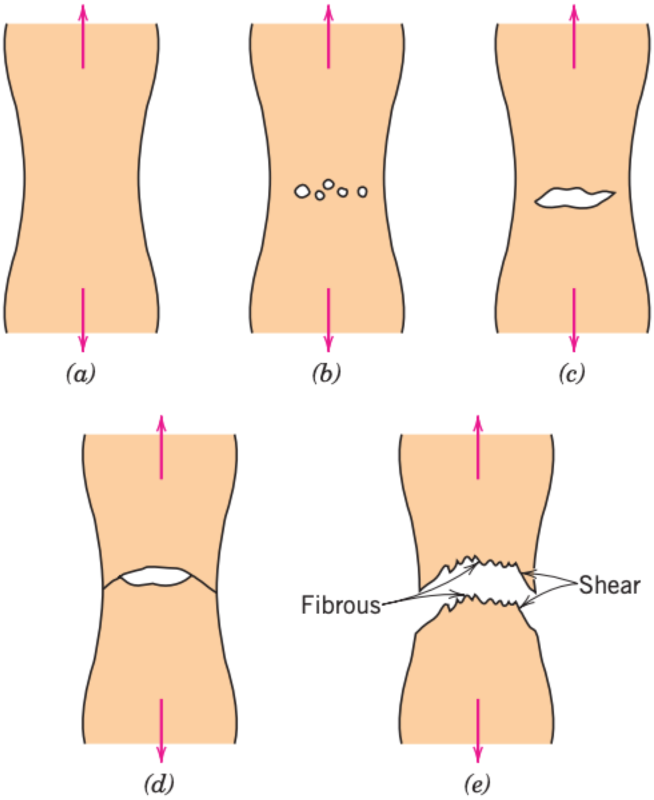

Figure 3.11: "Stages in the cup-and-cone fracture. (a) Initial necking. (b) Small cavity formation. (c) Coalescence of cavities to form a crack. (d) Crack propagation. (e) Final shear fracture at a 45 angle relative to the tensile direction" [6].

The other important fracture process in ductile material, formation of microscopic cracks, develops when a large number of dislocations becomes entangled into a high density [26]. The microscopic cracks link up with the main crack to advance the fracture process, as seen in figure 3.12 [26].

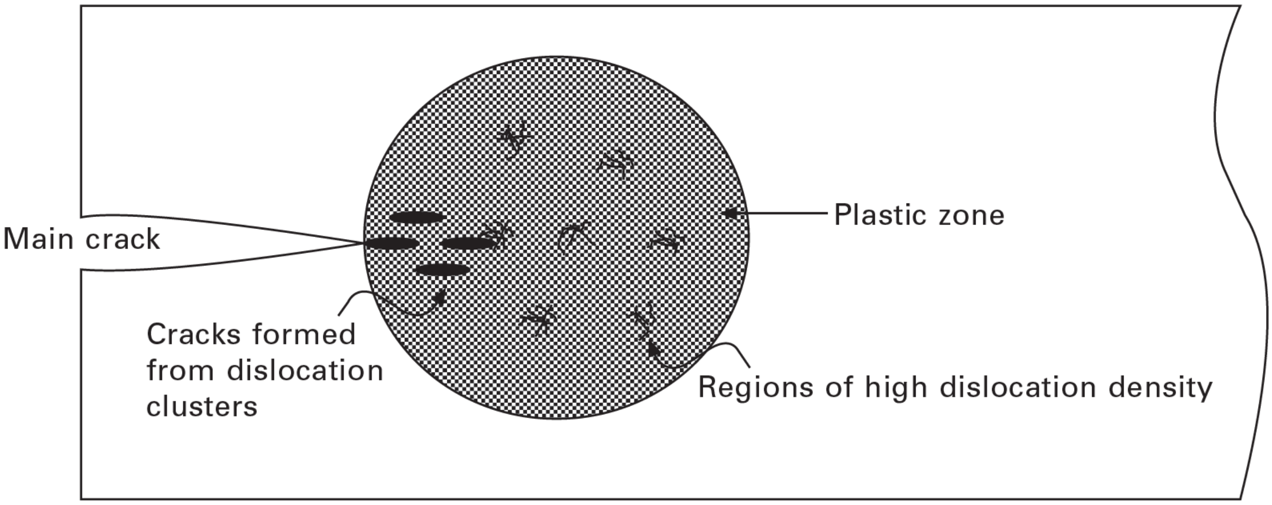

Figure 3.12: "Schematic representations of the ductile fracture process involving crack development from local regions of high dislocation density" [26].

3.4.2 Pores

Pores in SEM can be recognized by their smooth surface [28, 34, 41]. Examples of pores can bee seen in 3.13.

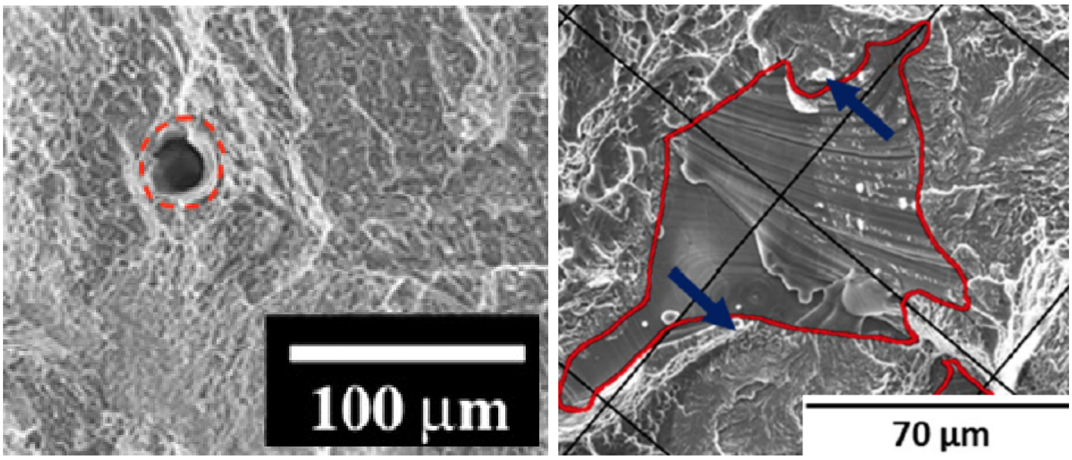

(a) Spherical pore seen in SEM [28].

(b) Example of pore seen in SEM (not spherical) [34].

Figure 3.13: Examples pores seen in SEM

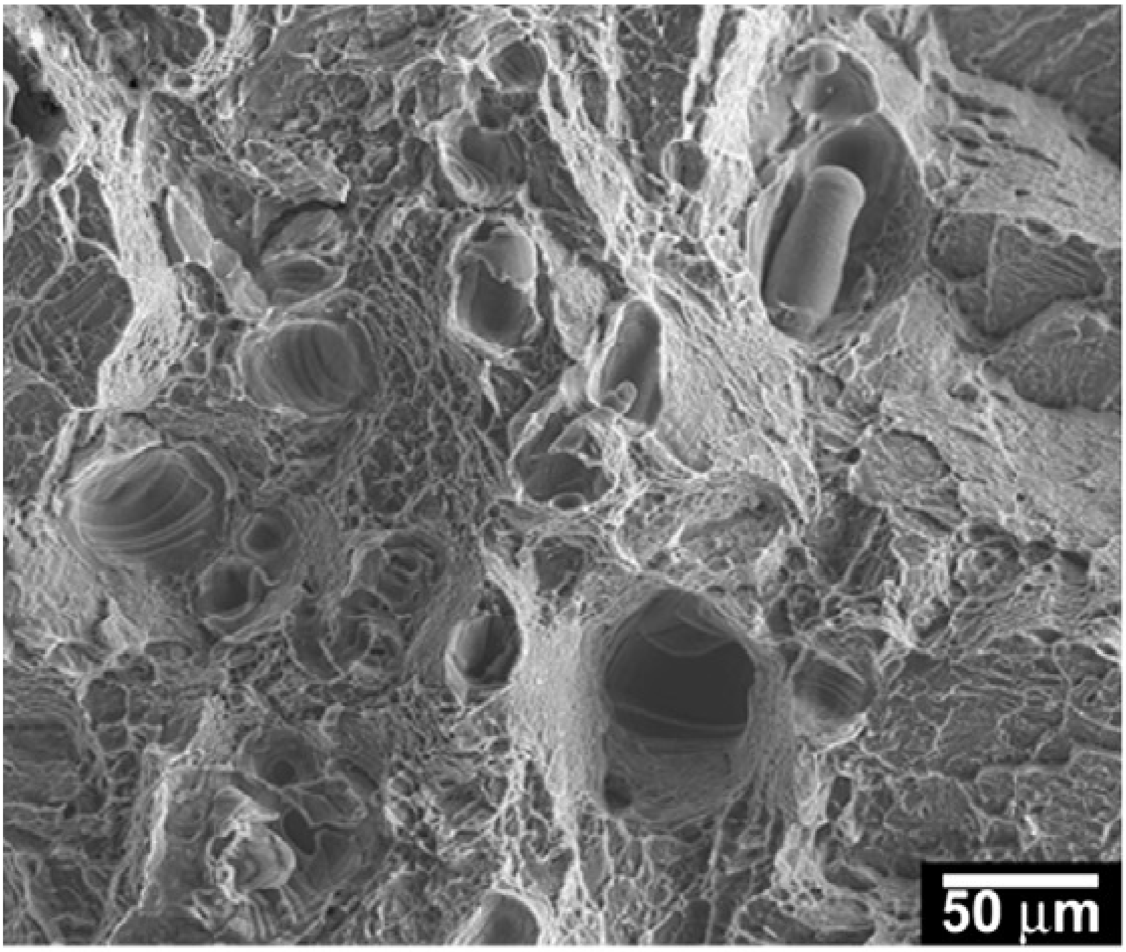

(c) Spherical pores seen in SEM [28].

Figure 3.13: Examples pores seen in SEM, continued.

3.5 Summary

3.5.1 Microstructure

PBF-LB/M built Ti6Al4V, without post heat treatment, has a microstructure consisting of fine martensitic (α') needles inside of columnar prior β-gains [29, 32, 36–40, 42, 49, 52, 54]. Both the martensitic (α') needles and columnar prior β-grains can lead to mechanical anisotropy [2, 32, 49, 54]. The columnar prior β-grains yield higher elongation when load is applied in the 90° orientation, than in the 0° orientation [28]. The α' is preferentially orientated leading to better strength in the 0° specimens, but a higher elongation in 90° specimens [49].

Full decomposition of α' into a lamella mixture of α and β happens for heat treatments of 800°C or above [45, 54]. The columnar prior β-grains remains until heat treated above the β transus temperature (995±5°C) [40, 42, 54]. For removal of the anisotropic effect of columnar prior β-grains without implementing a post heat treatment, a 67° rotational scanning strategy with the right process parameters are effective [8, 21].

3.5.2 Melt Pool Boundaries (MPBs)

MPBs are one of the main reasons for anisotropy and low ductility in PBF-LB/M parts [30]. They greatly affects the mechanical performance and impacts the microscopic slipping, macroscopic plastic behavior and fracture mode [30]. MPBs have been discovered in PBF-LB/M built Ti6Al4V, made out of Ti_3Al [20, 21, 37, 47].

Experimental results show that slipping along MPBs leads to a maximum elongation, when loaded at a 60° build orientation. From the maximum point, the ductility gradually goes down with the increase or decrease of the build orientation [30]. There is also seen a large difference in elongation between 0° and 90° tensile specimens due to MPBs [30].

3.5.3 Pores

Pores makes prints less ductile and more brittle [34]. They become stress concentrations which leads to failure [34, 38]. Cracks preferentially goes through the network of pores, propagating along their alignment [34]. There are various types of pore defects, but the most common are spherical entrapped gases (Figure 3.7b)) and elongated pores (Figure 3.7a)) [34, 38].

The influence of spherical pores on mechanical properties are independent of the loading direction, as their morphology makes it indifferent in which direction they are pulled upon [18]. Elongated pores are much more detrimental to the mechanical properties than spherical pores, due to sharp rims and crack tips resulting in areas of high stress concentration [11, 18, 38].

Elongated pores due to insufficient melting (lack of fusion) leads to anisotropy between 0° and 90° orientations, because of the way they open up when loaded upon [4, 38, 41].

Chapter 4

Results

To distinguish between the tensile specimens a two digit notation is used:
The first digit refers to the build orientation angle, and the second digit is exclusively connected to each specimen. E.g 0-2 is the 0° build orientation and the second of the two 0° tensile specimens.

For the Charpy specimens following notation is used:
The numbers stand for the build orientation angle. AS stand for as-built and MC stands for machined. E.g 45AS is the as-built Charpy specimen built at a 45° angle with respect to the horizontal plane.

Again, to clarify, all specimens have been heat treated at the same temperature. The as-built refers to the surface of the specimens, that have not been machined after the PBF-LB/M manufacturing.

As was mentioned in the methodology chapter about the roughness measurements, only the Charpy specimens were measured. The tensile specimens were produced and machined the same way, and it is therefore fair to assume that the roughness for the surfaces are equal.

4.1 Tensile

4.1.1 Mechanical properties

Tensile results with respect to the build orientation are seen in figure 4.1. It should be noted that the intervals of the result-axis (y-axis) are small.

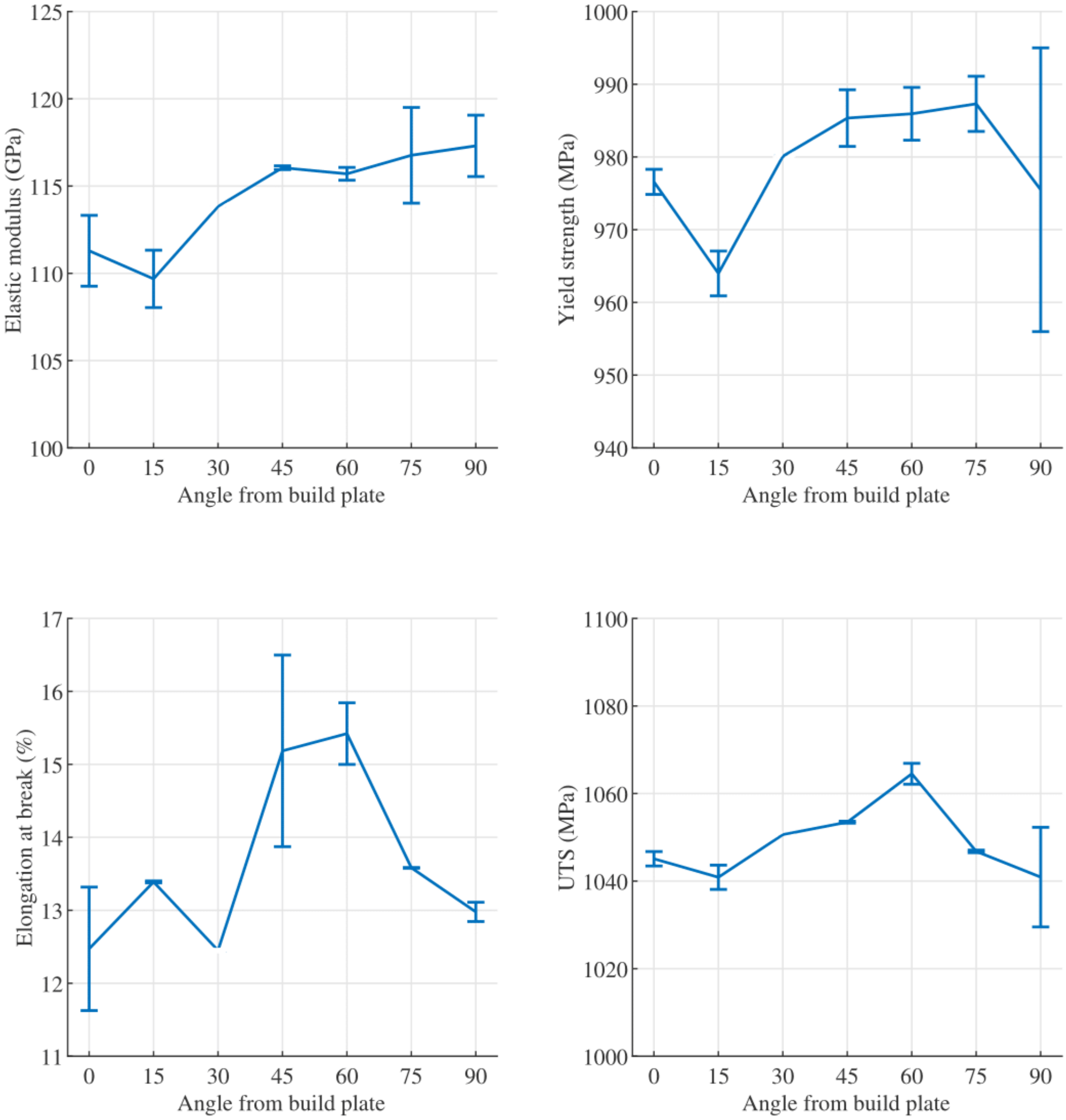

Figure 4.1: Tensile properties plotted with respect to build orientation.

4.1.2 Fracture surface, tensile specimens

For analysis of the fracture surface with SEM the 0-1, 0-2, 45-1, 45-2, 90-1 and 90-2 specimens were chosen. This was because the 45° specimens had the highest elongation (see figure 4.1) and that much of the existing literature on anisotropy is about comparison between 0° and 90° specimens. This makes them a key component in comparison with earlier research.

There are also focused on pores, as they can be critical for the mechanical properties [11, 18, 38, 41]. This also goes for the fracture surfaces of Charpy specimens presented later in the "Results" chapter.

Close-ups of the fracture surfaces with pores are shown in figure 4.3 and 4.4. It shows spherical dimples, which are a distinct feature of a ductile fracture [6, 12, 26]. This ductile fracture surface is valid for every analysed tensile specimen.

As explained in chapter 3.4.1 dimples form in ductile materials due to nucleation of microvoids [12]. These dimples form in the midsection due to an triaxial stress state induced when necking begins [6, 12]. An internal cavity is then formed in the midsection as these microvoids coalesce and link up of with the main crack [6, 12, 26]. Towards the end, the fracture ensues by shear deformation in the direction of maximum shear stress which is an angle of about 45° [6, 12]. Because of this shear lips are created [6, 12]. In figure 4.2 an overview of whole fracture surface of both specimens in the 0°, 45° and 90° groups are shown. The area within the yellow encircling shows the ductile midsection. This is where the fracture surface is highly dimpled. The area outside the yellow encircling is the shear lip. It should be noted that there is a clear difference between the shape of the 0-1 and 0-2 specimens compared with the rest of the specimens. This will be further discussed in the discussion chapter, 5.1.1.

In figure 4.3 close-ups of spherical pores taken with SEM is shown. They have the smooth surface and spherical form as described in the "Fractography" chapter in the theory section. There were few pores observed on the fracture surfaces of all the tensile specimens analysed. The pores in figure 4.3 were the only spherical pores found when combing the surface with the SEM.

In figure 4.4 microscopic elongated openings are shown. There were found elongated openings on the fracture surface of every tensile specimen. There was no significant difference in the number with respect to build direction. Overall there were few elongated openings.

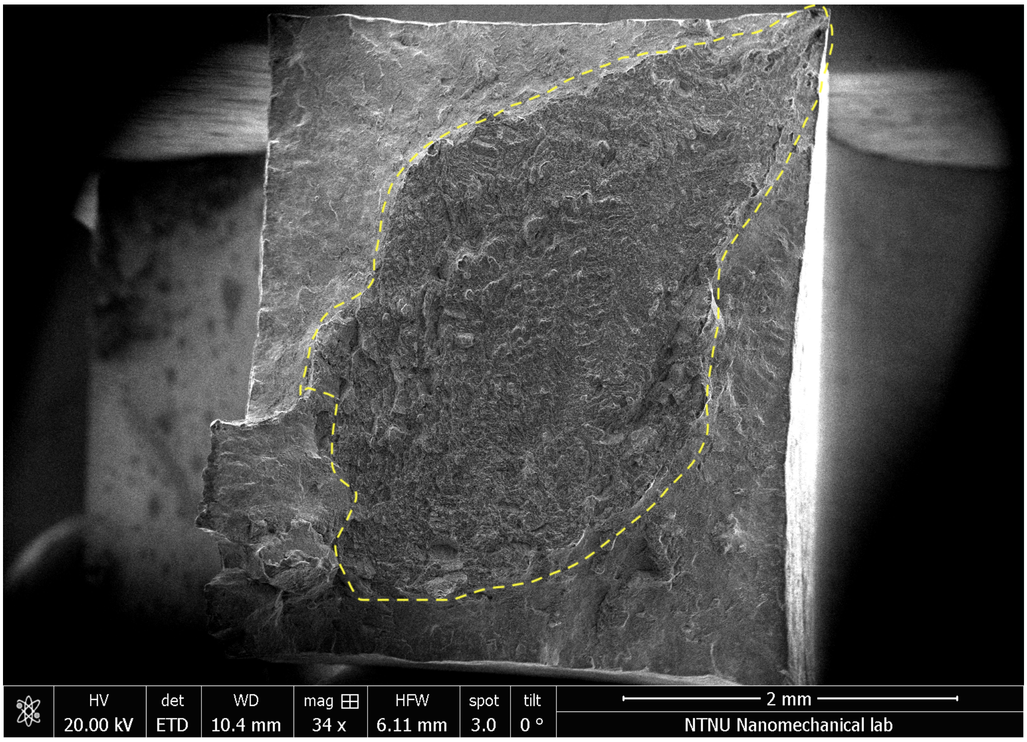

(a) 0-1 tensile specimen.

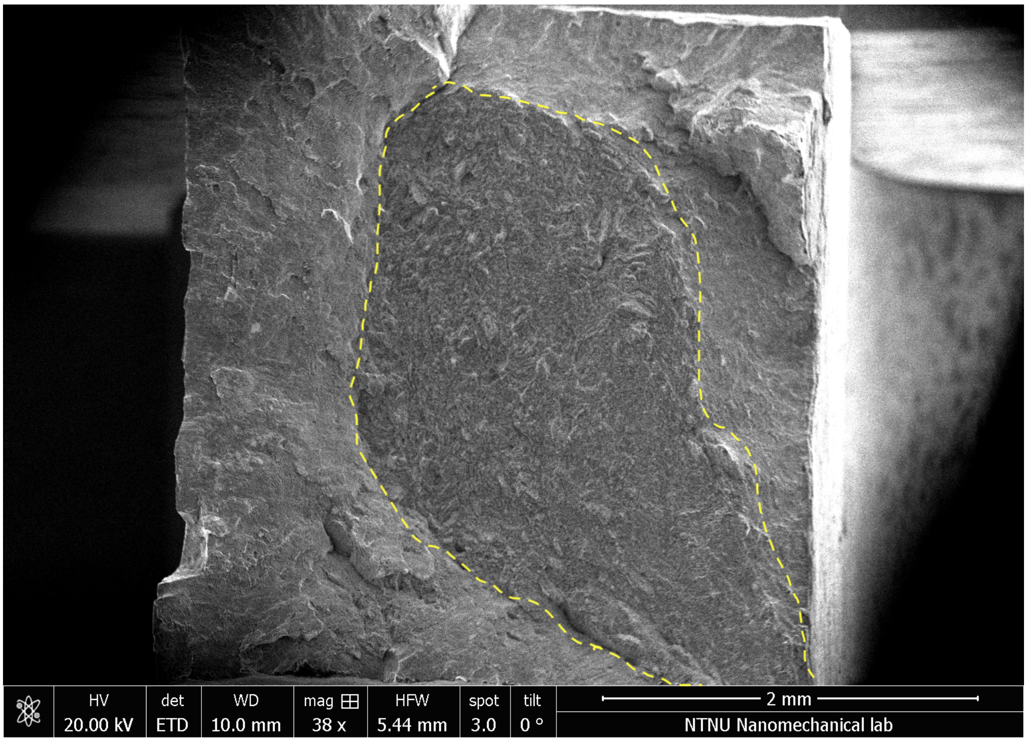

(b) 0-2 tensile specimen

Figure 4.2: Fracture surface of the tensile specimens.

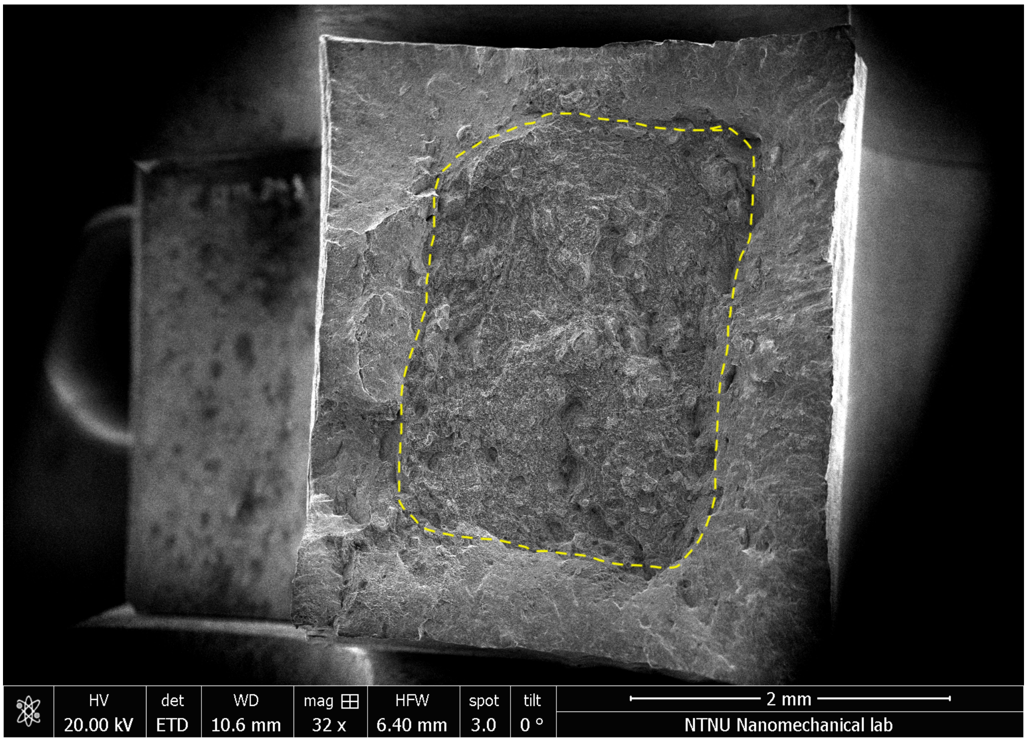

(c) 45-1 tensile specimen.

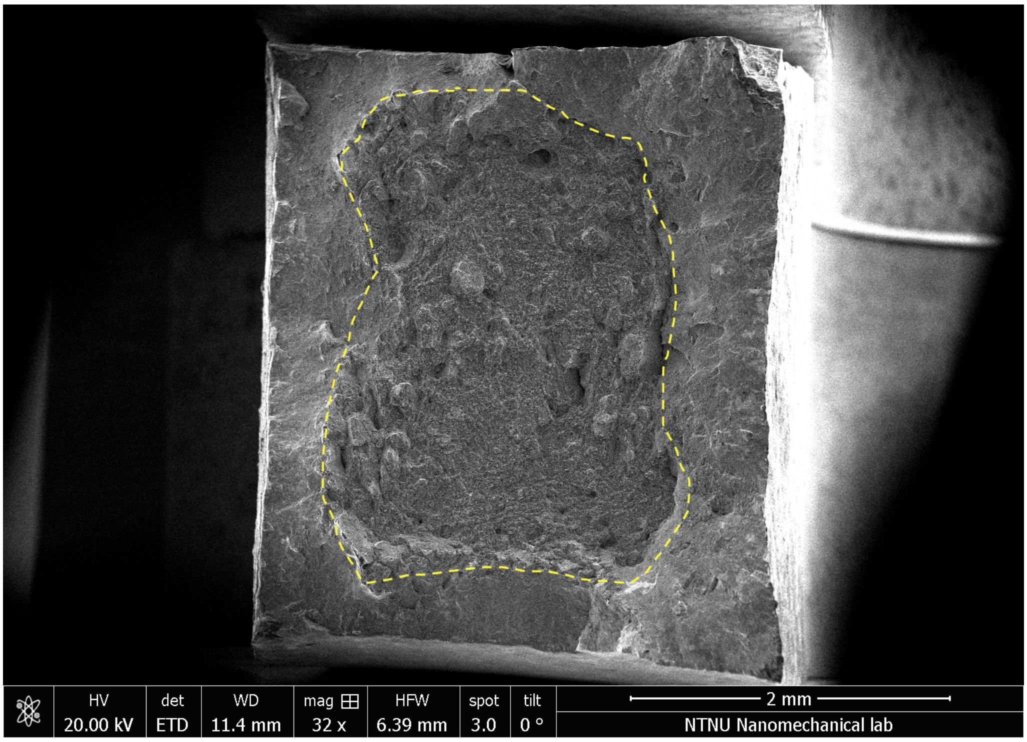

(d) 45-2 tensile specimen.

Figure 4.2: Fracture surface of the tensile specimens, continued.

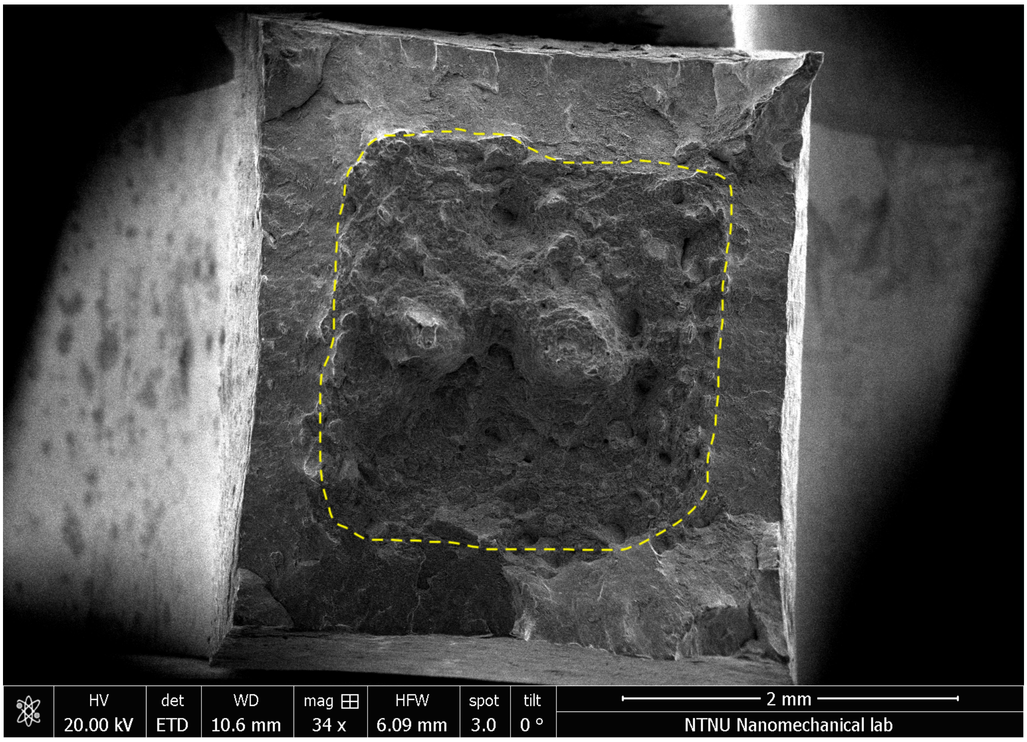

(e) 90-1 tensile specimen.

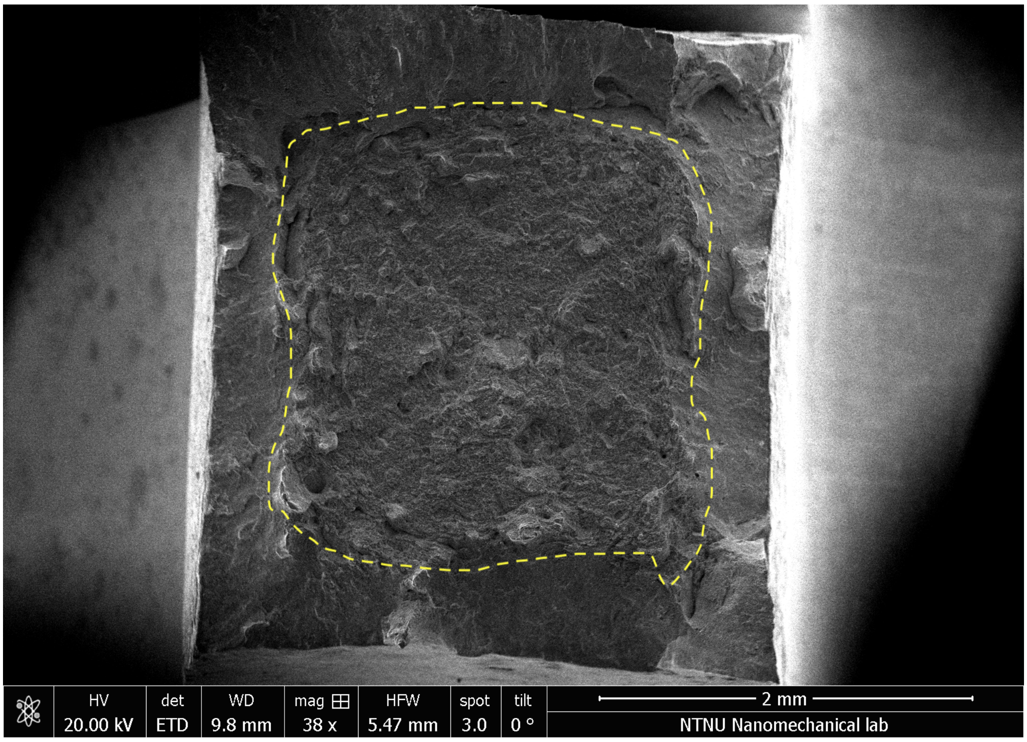

(f) 90-2 tensile specimen.

Figure 4.2: Fracture surface of the tensile specimens, continued.

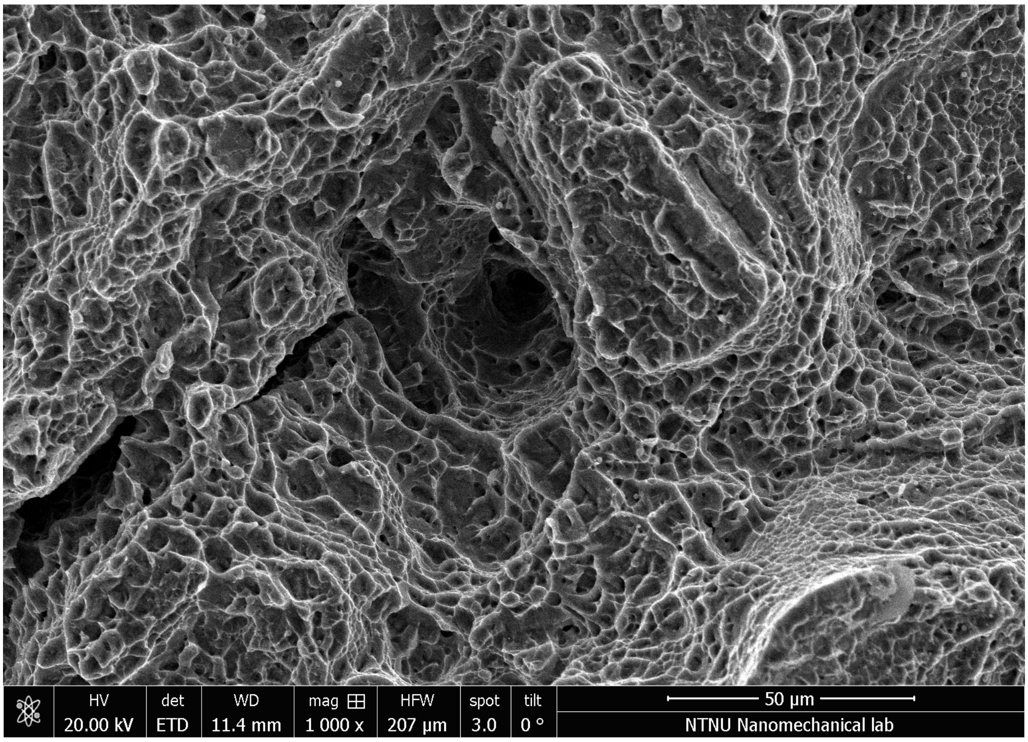

(a) Spherical pore on the fracture surface of the 45-2 tensile specimen.

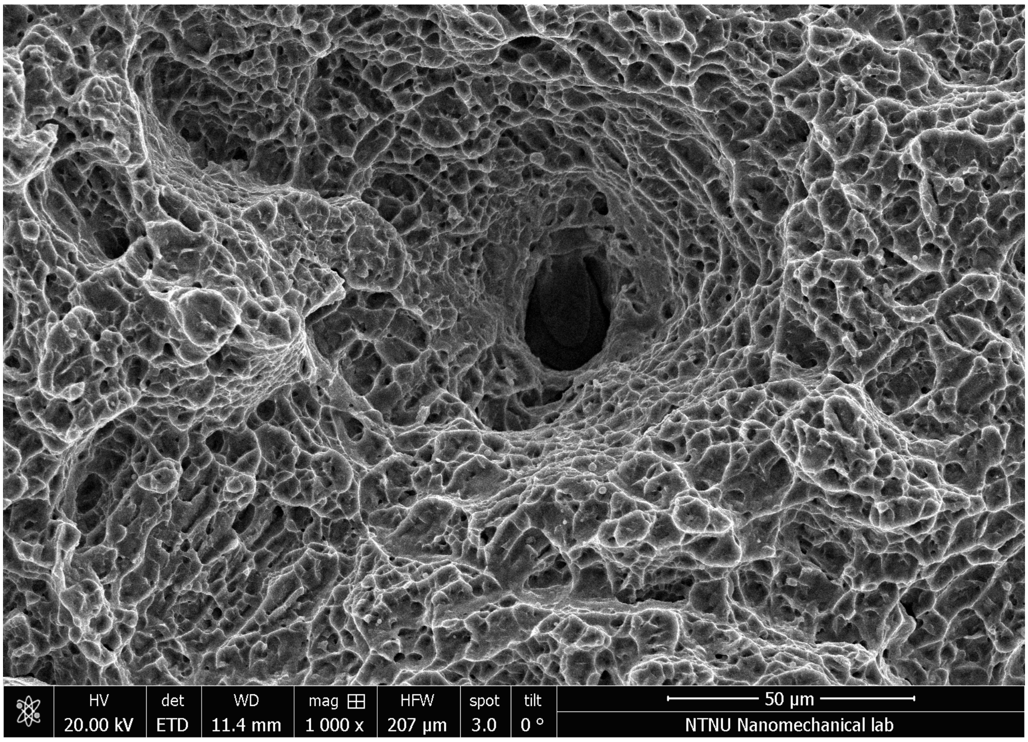

(b) Another spherical pore on the fracture surface of the 45-2 tensile specimen.

Figure 4.3: Pores found on the fracture surface of tensile specimens.

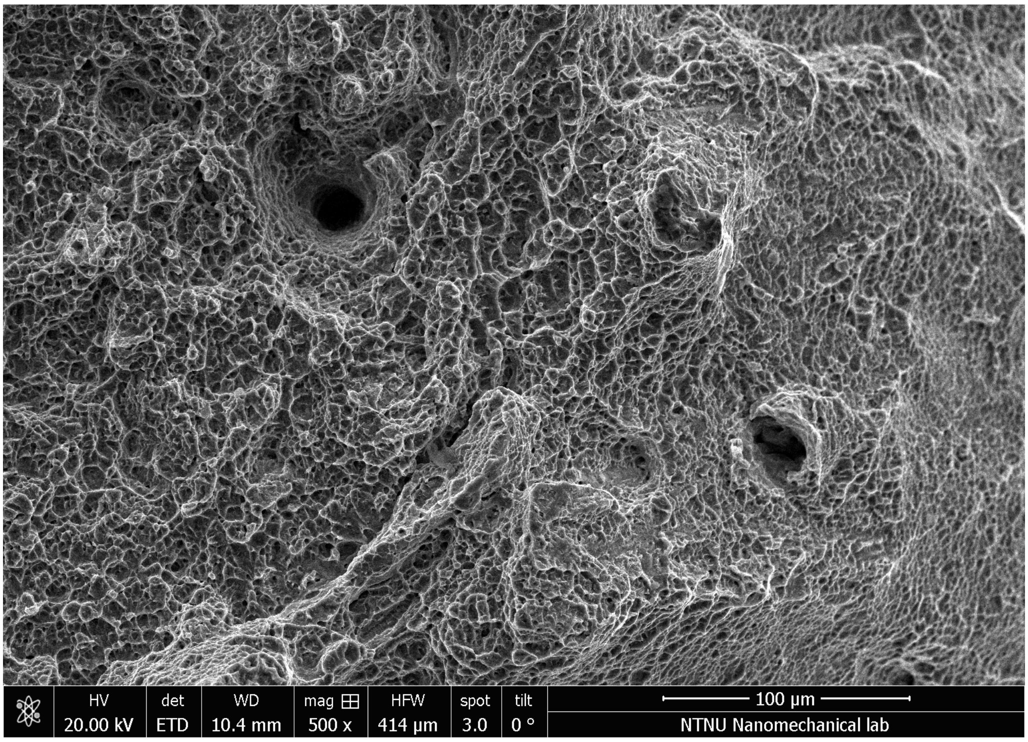

(c) Spherical pores found in tensile fracture surface of specimen 90-2.

Figure 4.3: Pores found on the fracture surface of tensile specimens, continued.

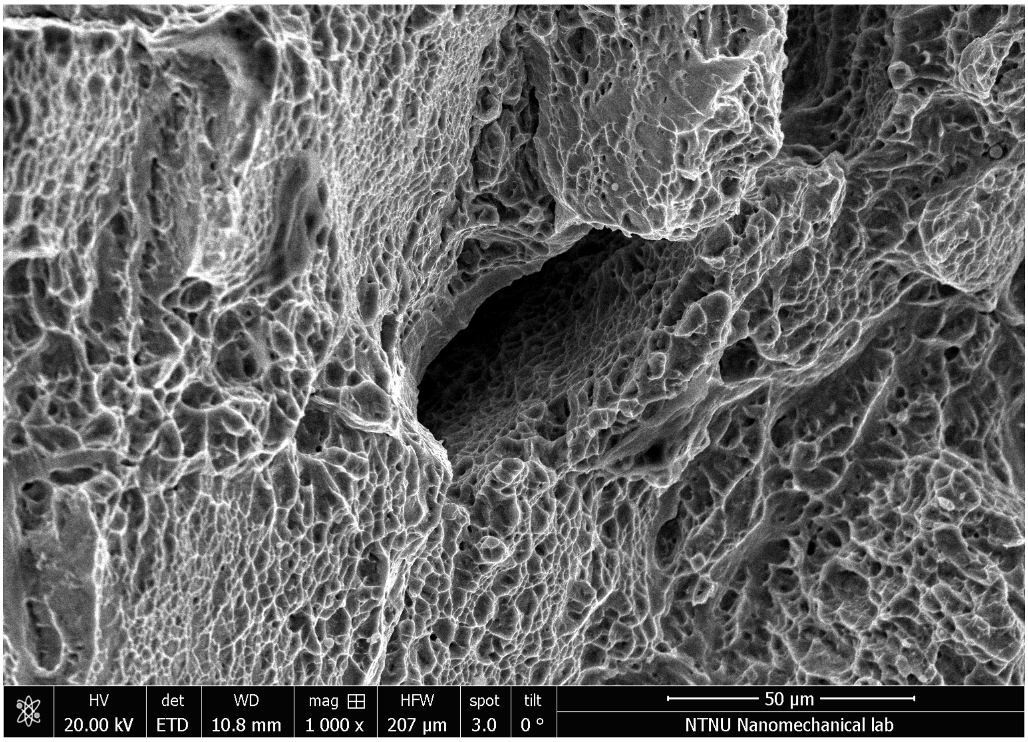

(a) Elongated opening in the fracture surface of the 45-1 tensile specimen.

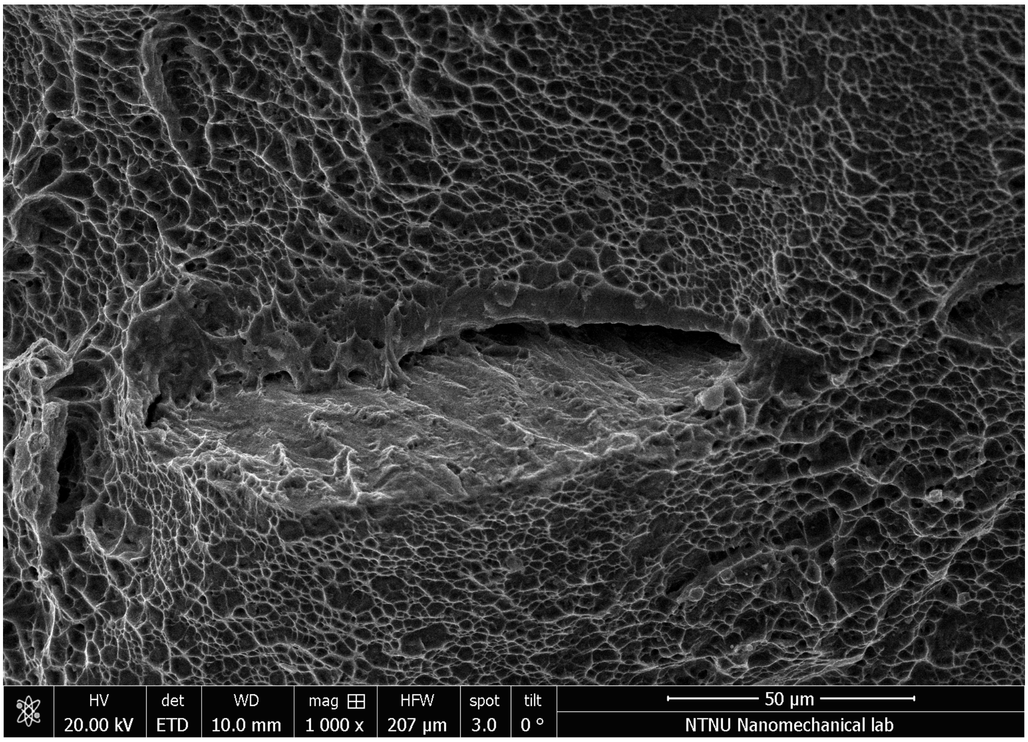

(b) Elongated opening in the fracture surface of the 90-1 tensile specimen.

Figure 4.4: Examples of elongated openings found on all the tensile specimen fracture surfaces.

4.2 Charpy

4.2.1 Impact toughness

The result of the impact toughness from the as-built and the machined Charpy specimens can be seen in figure 4.5. Both have a similar trend, but at a different level of absorbed energy.

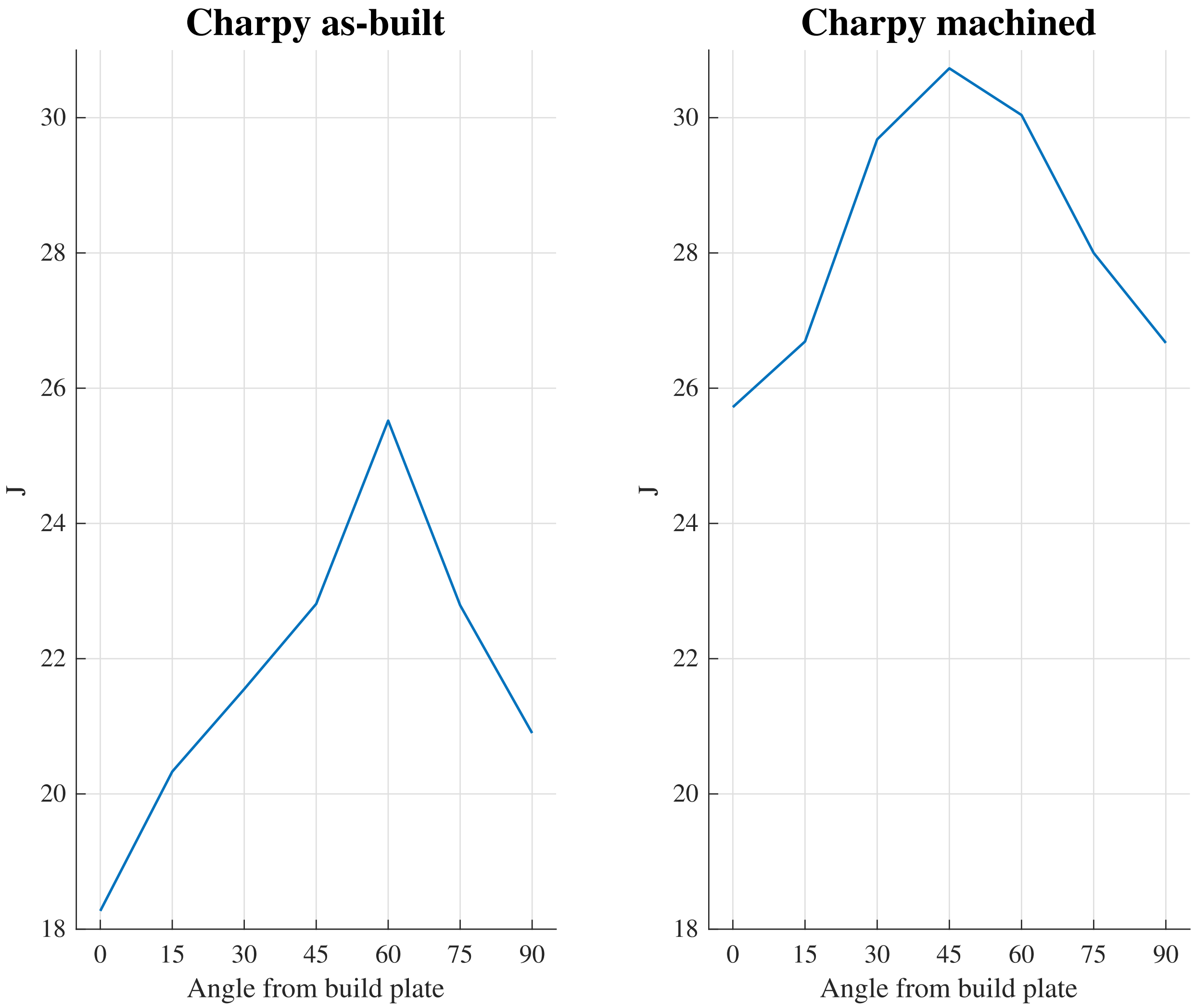

Figure 4.5: Charpy impact results, absorbed energy [J].

4.2.2 Roughness measurements

Roughness measurements of the Charpy specimens can be seen in table 4.1. Detailed roughness results can be seen in appendix B.

Table 4.1: Roughness, Ra [µm] value, from the Charpy specimens.

Specimen	Charpy as-built	Charpy machined
0°	12.2	0.19
15°	15.9	0.41
30°	13.4	0.17
45°	9.8	0.26
60°	11.9	0.22
75°	13.2	0.24
90°	6.0	0.27

4.2.3 V-notch sizes

Pictures was taken with a microscope to determine if there was a difference between the v-notch sizes of the as-built and machined Charpy specimens, as this could possibly have impact on the impact toughness [22]. The v-notches of the as-built Charpy specimens are difficult to determine, because there are partly melted powder particles covering the as-built surface. This is illustrated with pictures of two different measurements of the same v-notch of the as-built 15° and 45° specimens in figure 4.6 and 4.7 respectively. The machined v-notch radius size of both the 15° and 45° machined Charpy specimens can be seen in figure 4.8. It should be noted that the as-built v-notches are smaller than the machined v-notches. This was true for all the as-built v-notches, the pictures of the 15° and 45° specimens are just chosen as an example.

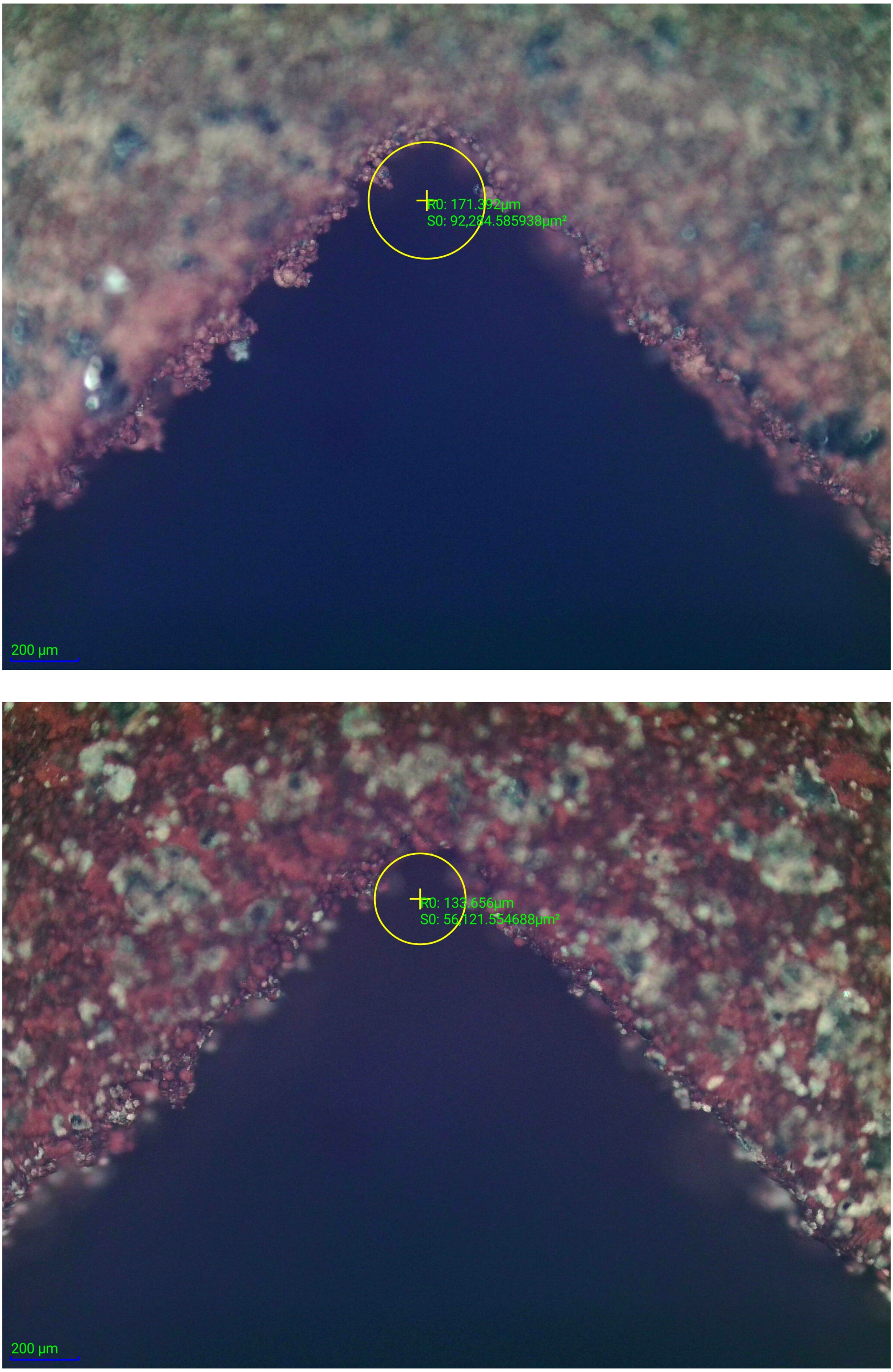

Figure 4.6: Two pictures of the same notch, the as-built 15°, showing the difficulty determining the v-notch radius because of the oxidation layer on the surface.

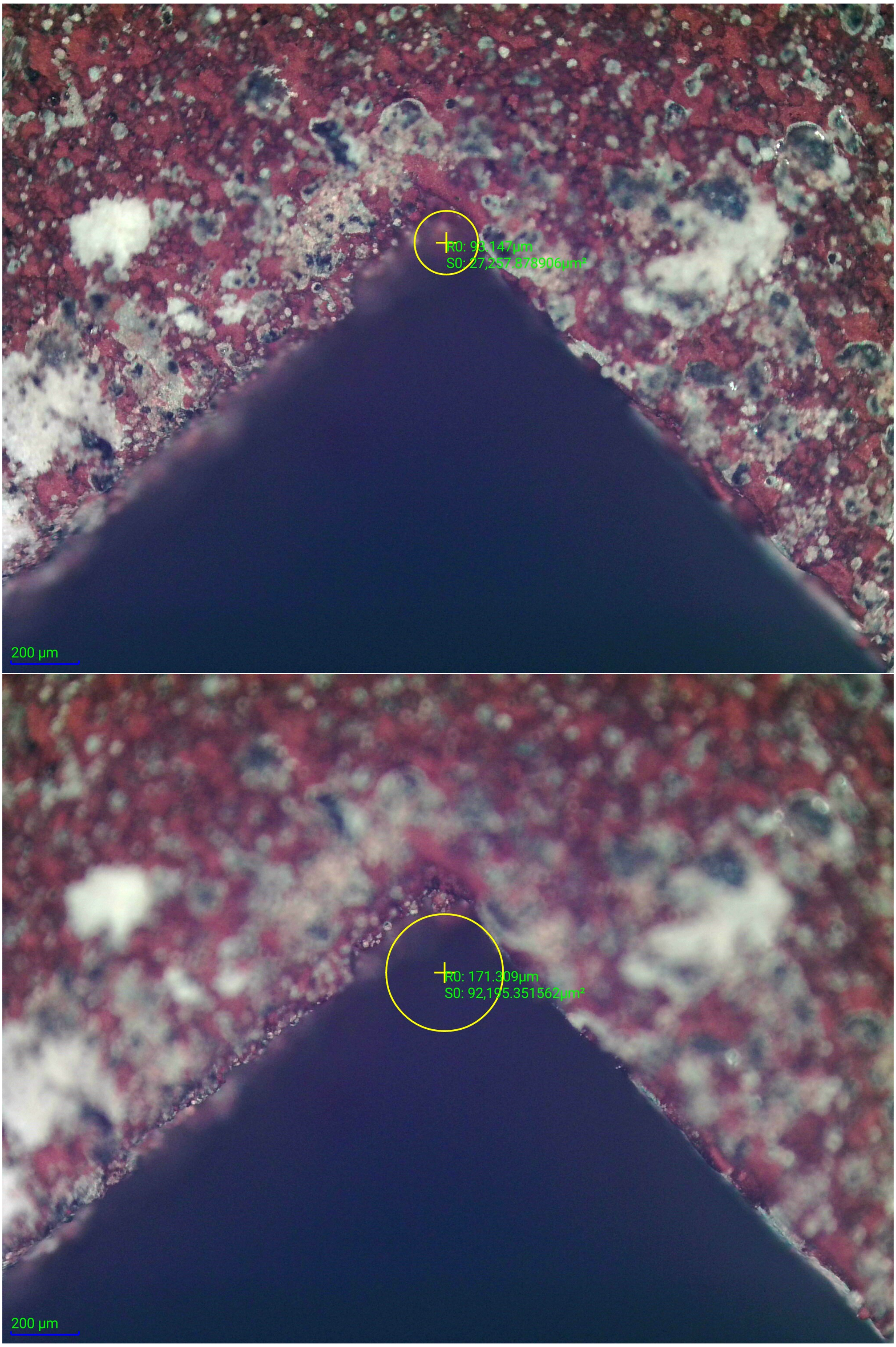

Figure 4.7: Two pictures of the same notch, the as-built 45°, showing the difficulty determining the v-notch radius because of the oxidation layer on the surface.

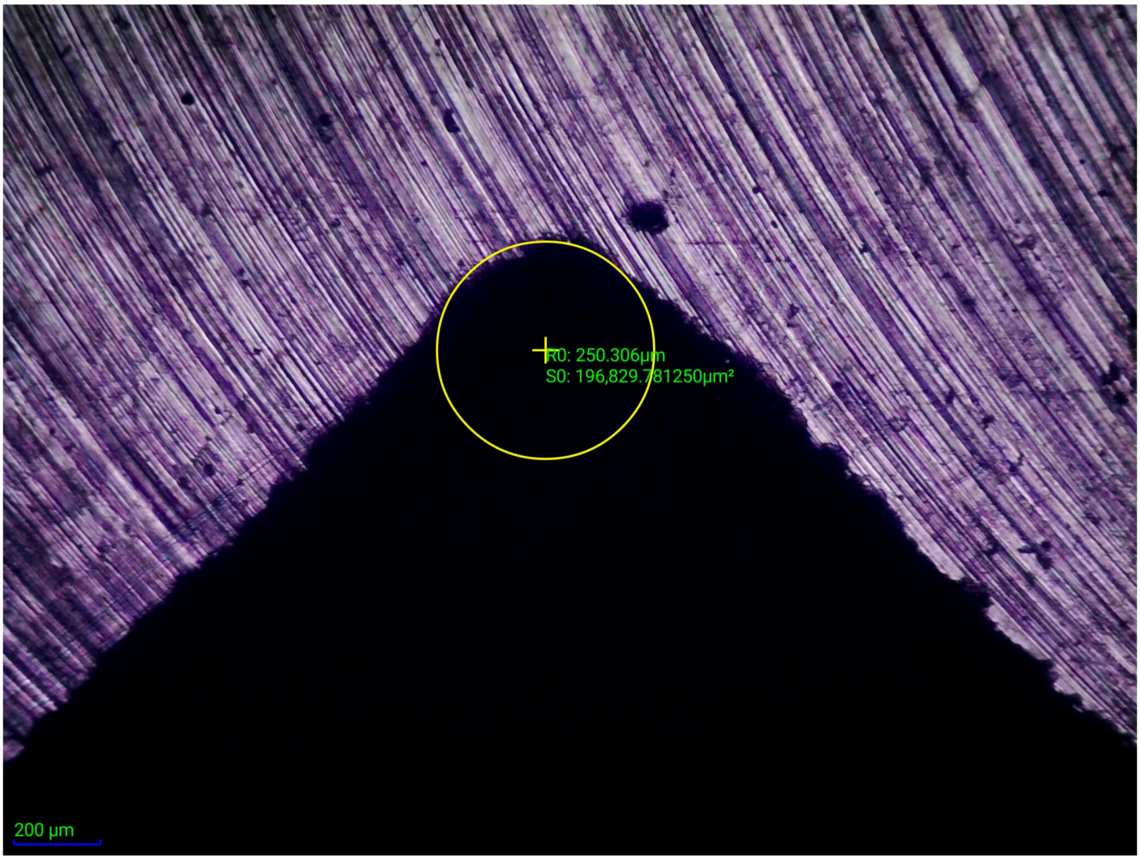

(a) The 15° machined Charpy specimen.

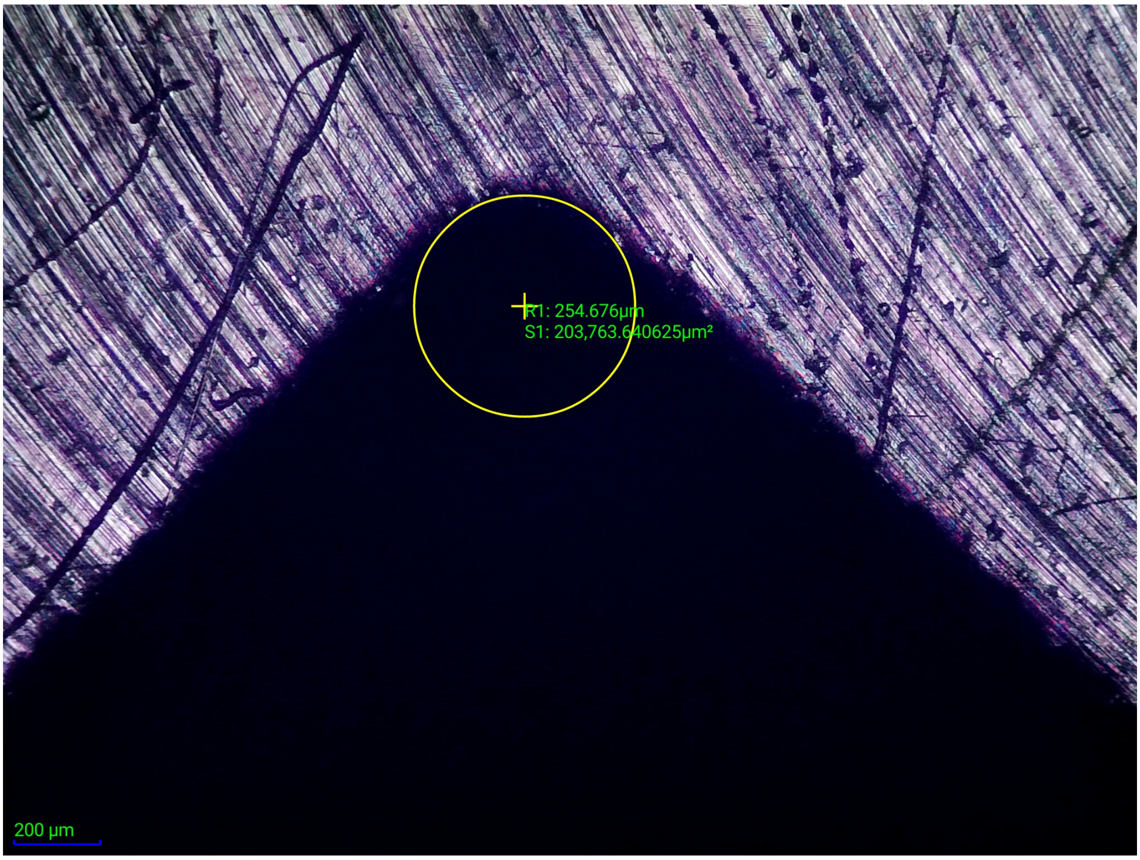

(b) The 45° machined Charpy specimen.

Figure 4.8: Pictures of two machined Charpy specimens showing the v-notch radius and the surface.

4.2.4 Fracture surface, Charpy specimens

The dominant fracture behavior of all the Charpy specimens were ductile, as can be seen in the SEM pictures in this sub-chapter. Both spherical and elongated pores were found, as seen in figure 4.9, 4.10 and 4.11. Otherwise there were overall few pores on the fracture surface of each specimen. There are no significant difference in the number of pores on the fracture surface with respect to the build orientation.

Large pores, much larger and easier to spot than on the other specimens, was found on the 0AS specimen, as can especially be seen in figure 4.10b and 4.10c. It should be mentioned that such large pores were not present in the 0MC specimen. The long bright grain like structure seen clearly in figure 4.10b was deemed as contamination and not a part of the fracture surface. As on tensile fracture surfaces there were found elongated openings in the Charpy specimens, as seen in figure 4.12.

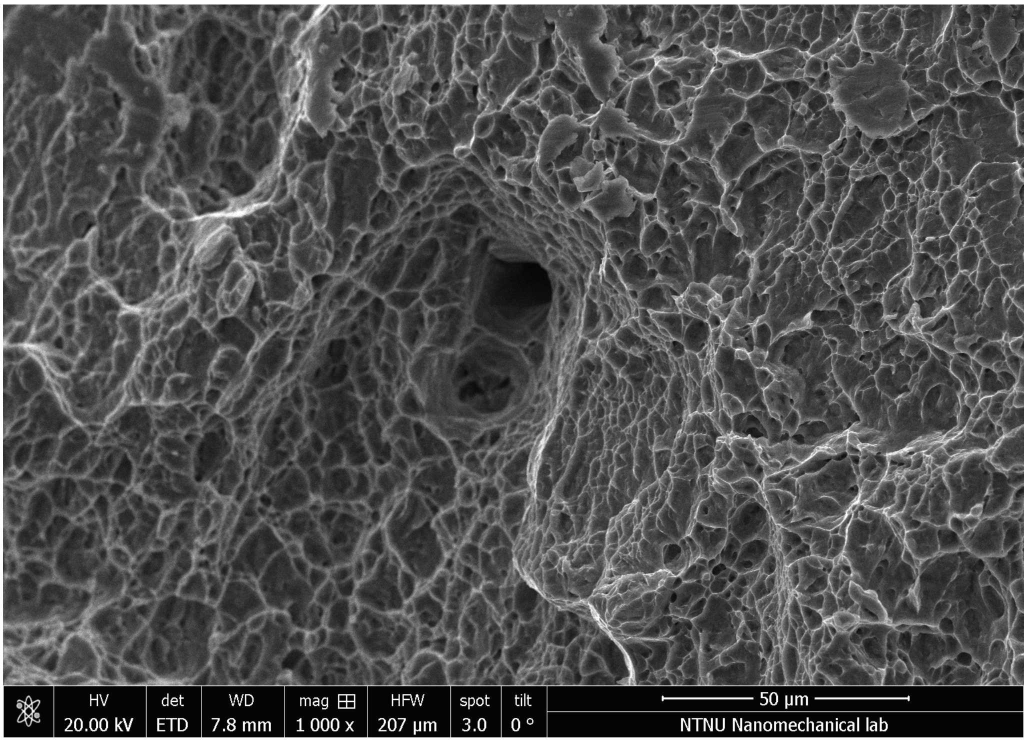

Figure 4.9: SEM of a spherical pore on the fracture surface of the machined 0° Charpy specimen.

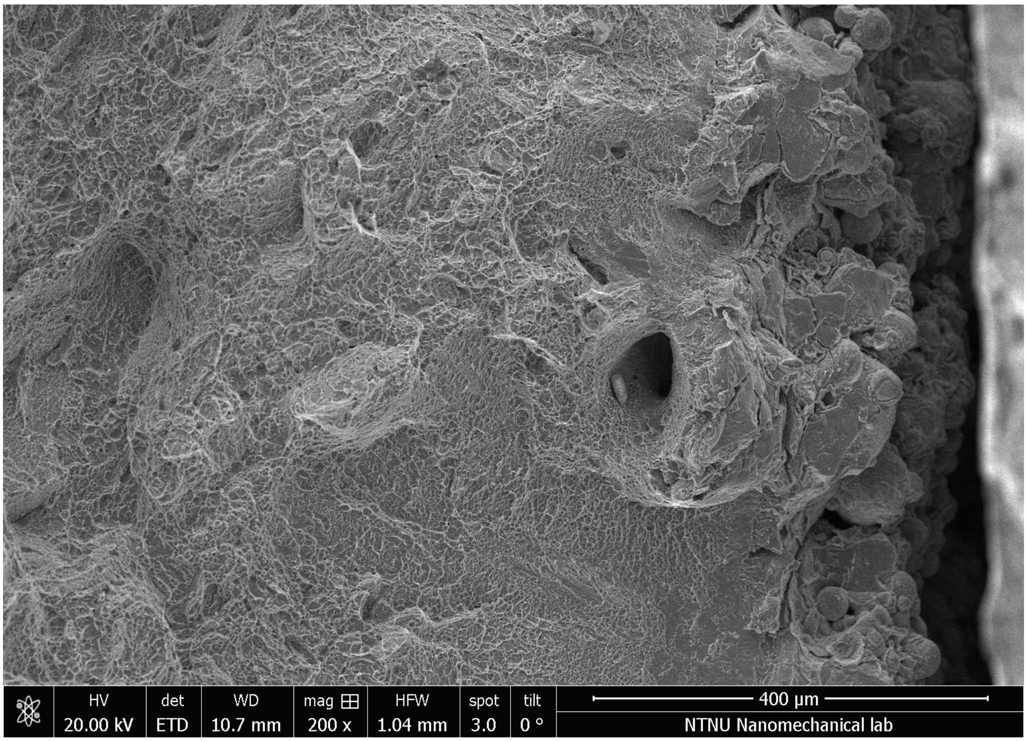

(a) A large elongated pore, 0AS specimen.

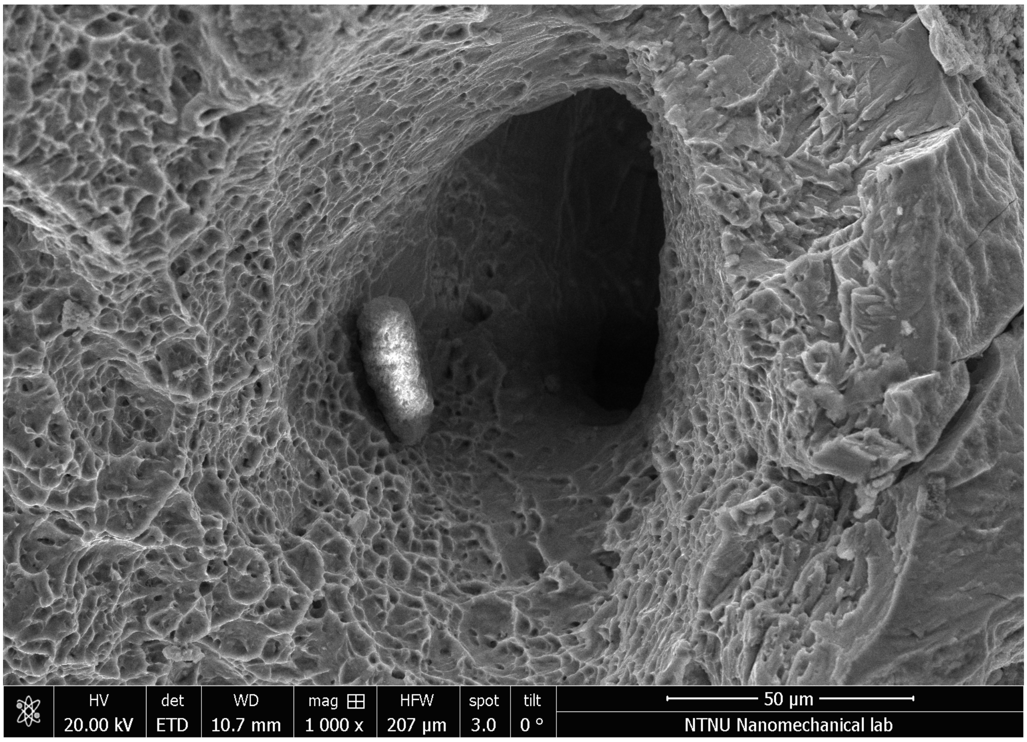

(b) Close-up of the elongated pore in 4.10a, 0AS specimen.

Figure 4.10: SEM of defects on the fracture surface of the as-built 0° Charpy specimen.

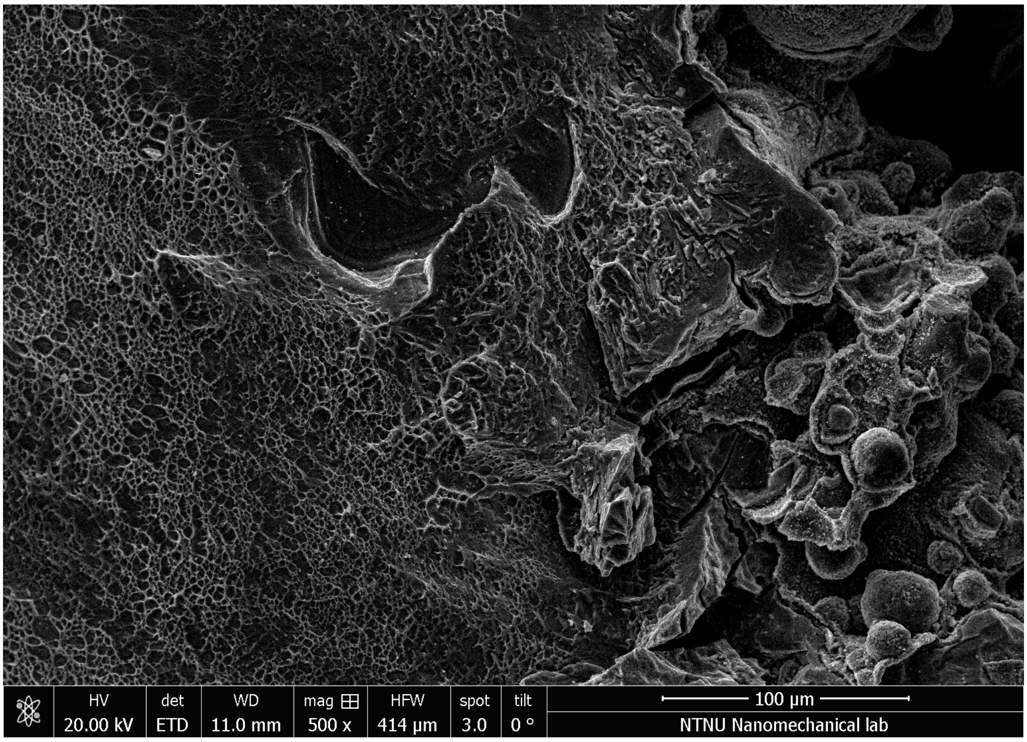

(c) Large elongated pore, 0AS specimen.

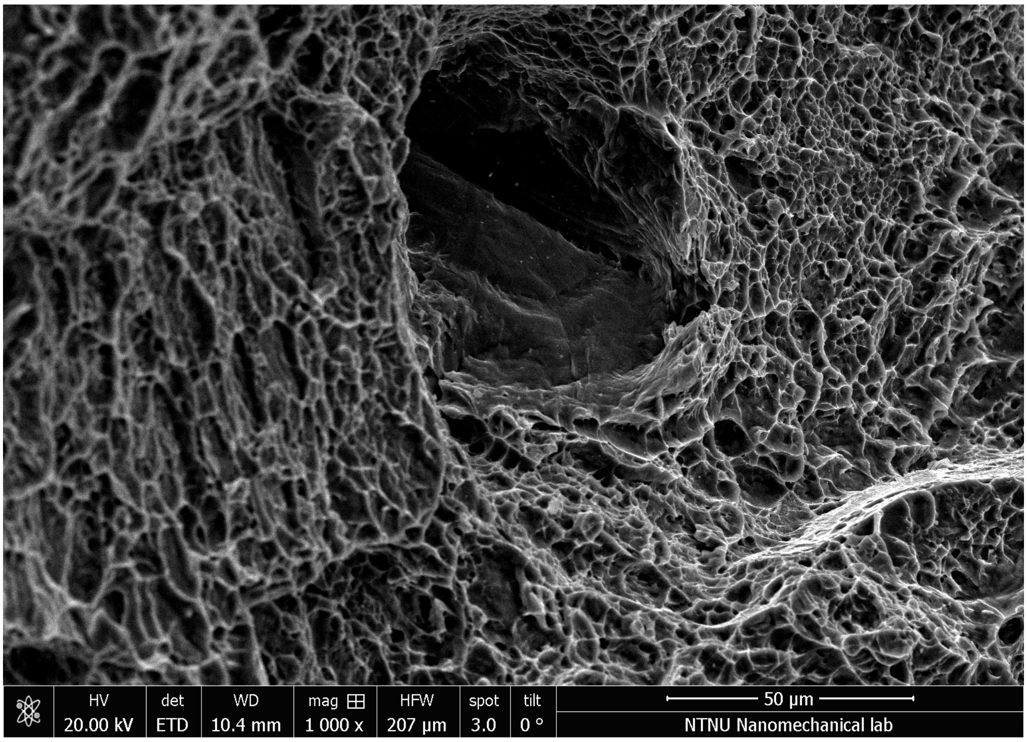

(d) Spherical Pore, 0AS specimen.

Figure 4.10: SEM of defects on the fracture surface of the as-built 0° Charpy specimen, continued.

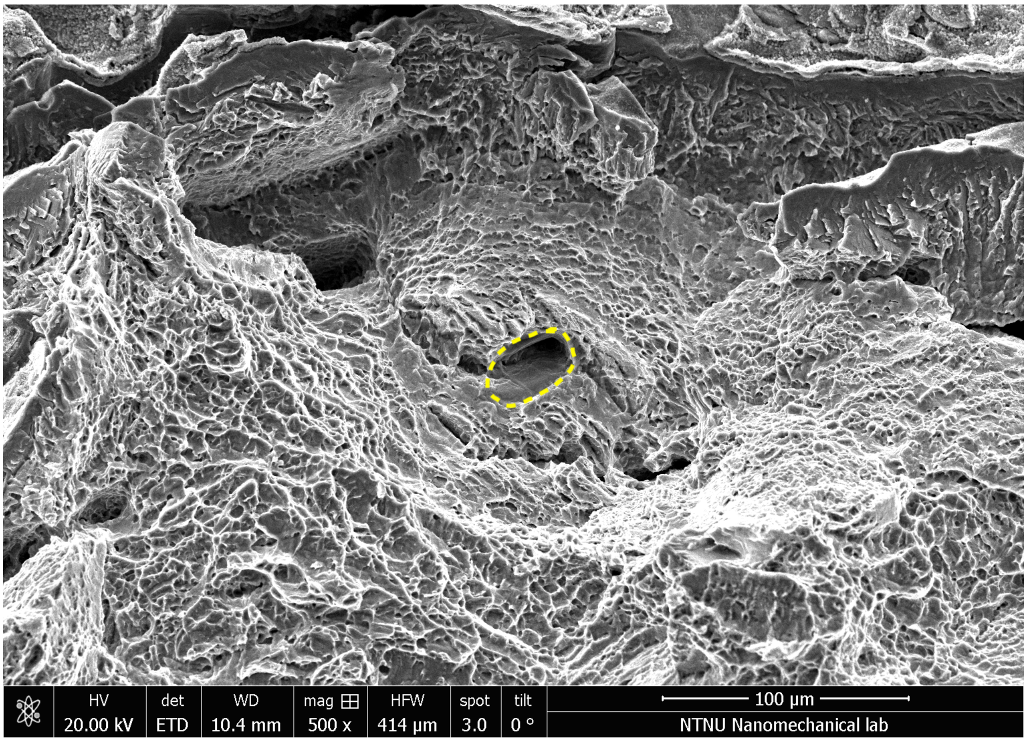

Figure 4.11: Pore (encircled in yellow) found on the fracture surface of the as-built 45° Charpy specimen.

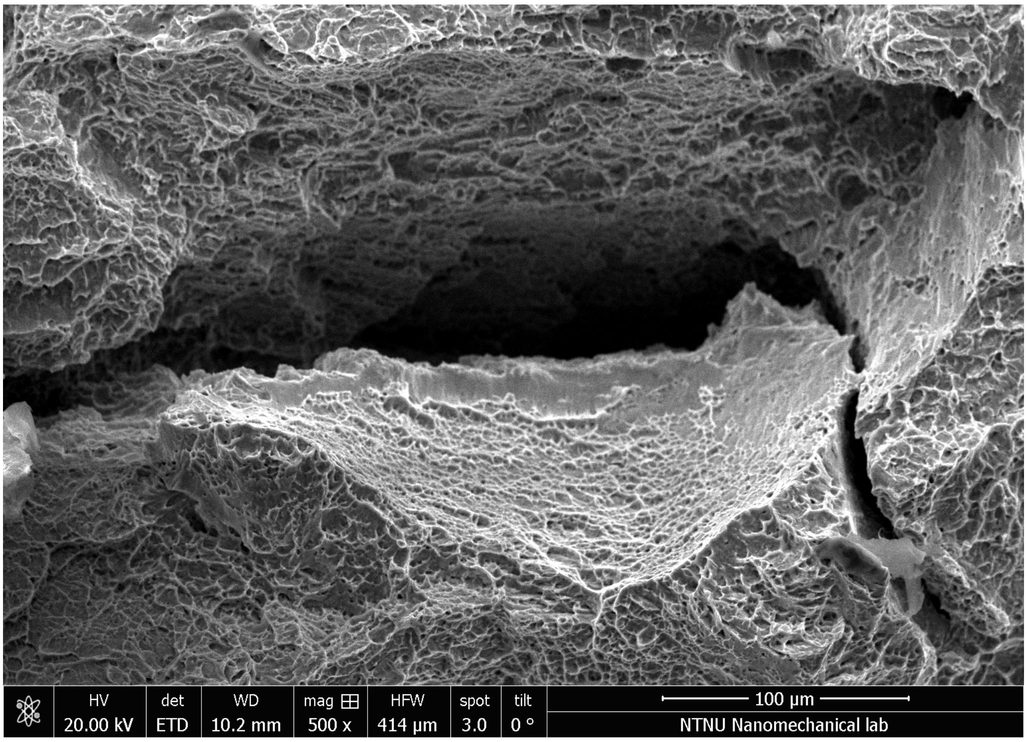

(a) Close-up of an elongated opening, 45MC.

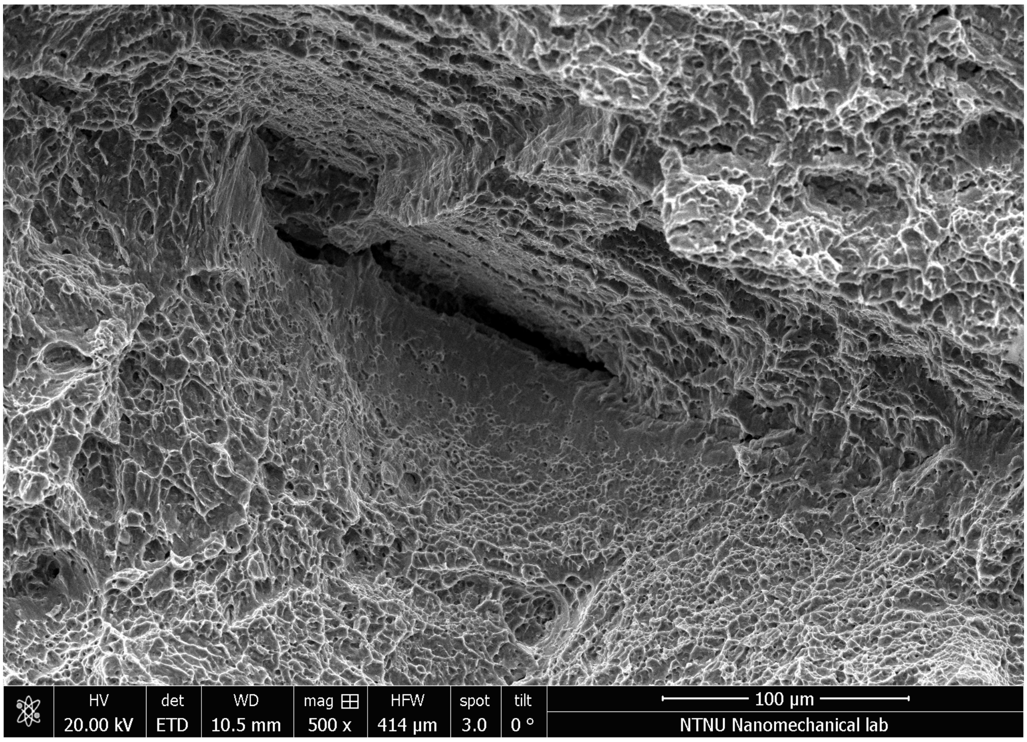

(b) Close-up of elongated opening, 45MC.

Figure 4.12: SEM of defects on the fracture surface of the machined 45° Charpy specimen.

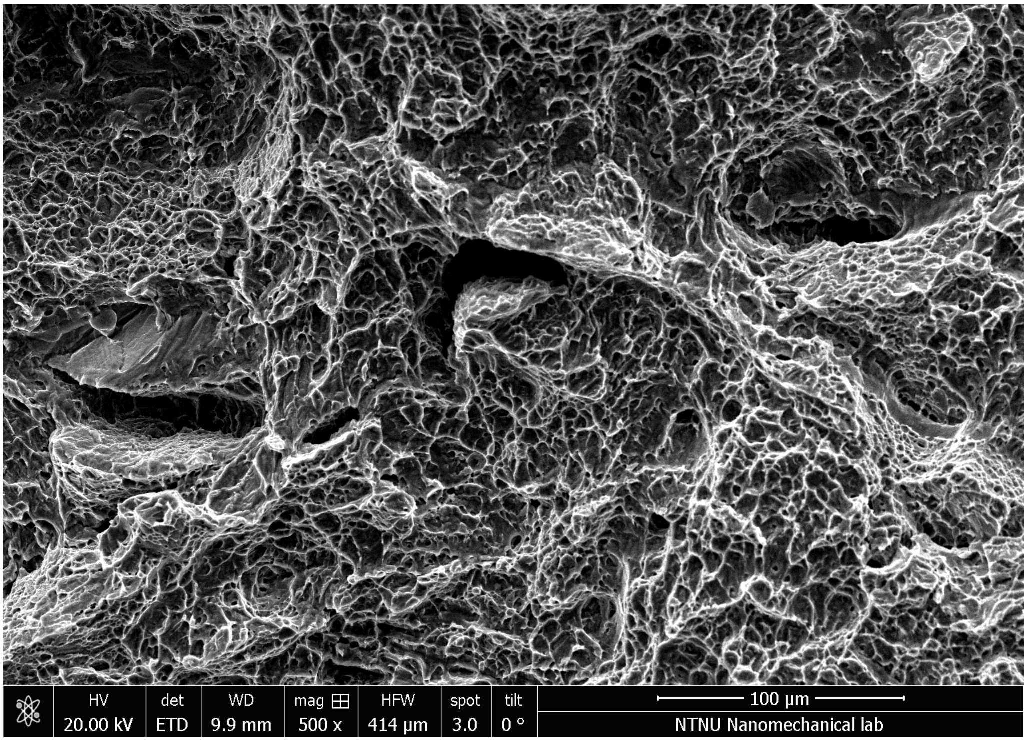

(c) Elongated openings, 0AS.

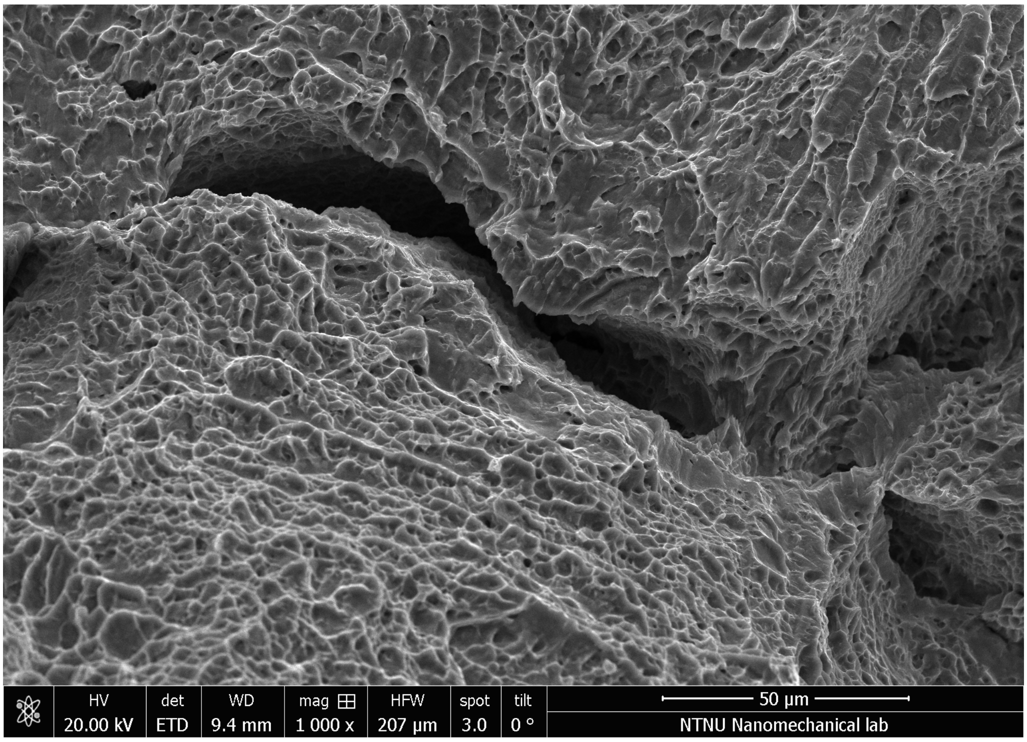

(d) Close-up of an elongated opening, 0MC.

Figure 4.12: Continued.

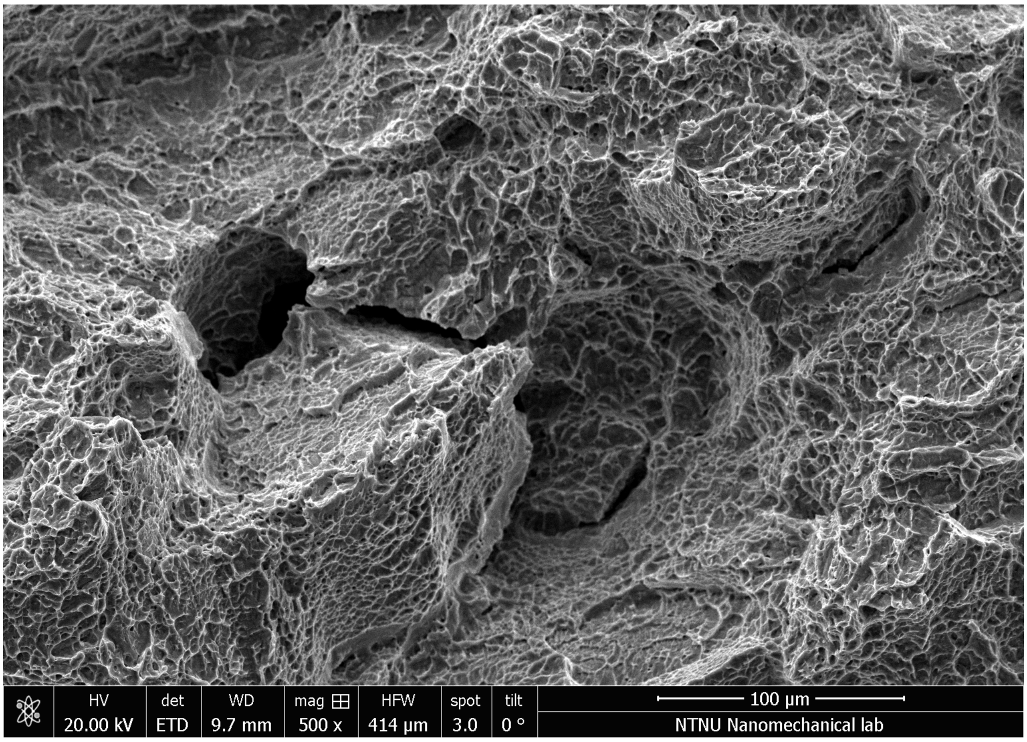

(e) Cluster of elongated openings, 45AS.

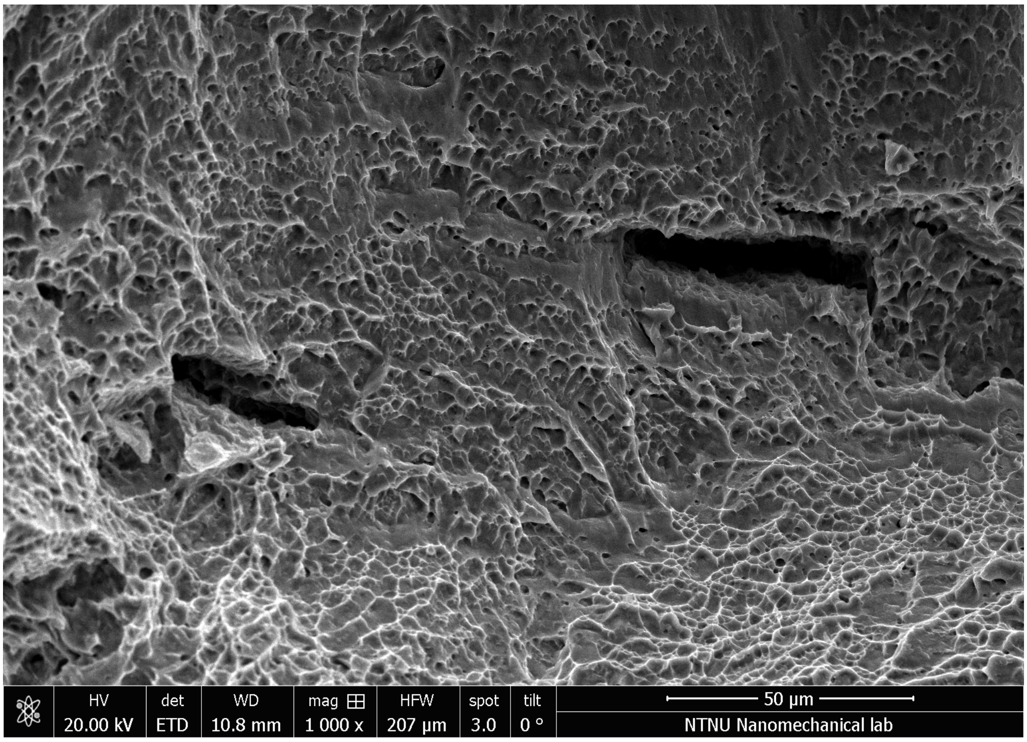

(f) Close-up of elongated opening, 45AS.

Figure 4.12: Continued.

Chapter 5

Discussion

Without considering any specific build orientation, the test results are comparable to the results of the 850°C heat treated specimens of Vrancken et al.[40] (see table 3.1). These results were deemed by Vrancken et al.[40] as the best result with respect to heat treatments.

There are small differences between the tensile test results of yield strength, elastic modulus and UTS, seen in figure 4.1, with respect to build orientation. For the elongation results there are bigger differences and a trend can be seen.

Roughly describing the trend (from left to right as seen in 4.1):
The mean of the elongation increases from the 0° specimen, maxes out on the 60° specimens, then follows a similar inverted trend down, before ending on a similar value for the 90° specimen as for the 0° specimens. There is a difference in absorbed energy between the as-built and machined Charpy specimens. However, a similar trend like that of the tensile elongation results, can be seen in both AS and MC Charpy specimens with respect to build orientation.

An Anlysis of variance (ANOVA) was performed to investigate if there is any statistically significant difference between the mechanical properties of the tensile specimens with respect to build directions. The analysis was made with Matlab's inbuilt ANOVA function. Two ANOVA analysis were made, a balanced and unbalanced one. The balanced one is without the 30° tensile specimen as there has to be an equal amount of specimens in each group in the analysis. In unbalanced ANOVA it does not need to be an equal amount of specimens in the groups, and therefore the 30° tensile specimen was included in this analysis. This was done to see if there was any significant difference with or without the single 30° tensile specimen in the analysis, or if it gave the same outcome.

In an ANOVA the null hypothesis is that the expected value is equal for every group, here build orientation. The null hypothesis is rejected if the p-value is less than the chosen confidence level [23]. In this thesis a confidence level of 0.05 was chosen, as this is a typical value to set for an ANOVA [23]. This means, that if the p-value is smaller than the chosen 0.05, it can be concluded that a significant statistical difference between the groups exist [23]. On the other hand, if the p-value is larger than the chosen confidence level it means that the variation between the groups are too small to be considered as statistically different [23].

The p-values calculated in the ANOVA can bee seen table 5.1. As seen all the p-values are larger than the confidence level of 0.05. This means that a statistically significant difference between the groups dose not exist [23]. This is true for all the tensile results, including the elongation.

Table 5.1: P-values of the ANOVA of the tensile test results

	Unbalanced with the 30° specimen	Balanced without the 30° specimen
E-modulus	0.11	0.08
Yield strength	0.54	0.45
UTS	0.12	0.09
Elongation	0.10	0.09

Further in this chapter the impact of pores, MPBs, heat treatment and microstructure on the mechanical properties will be discussed. There will also be made an effort to discuss the reason of the trend seen in the elongation for tensile specimens and the impact toughness for Charpy specimens, with respect to build orientation.

To the author's knowledge there is no available research on PBF-LB/M of Ti6Al4V that describes similar trends as those seen in this thesis. Most research found in literature was performed with two build orientations, 0° and 90°. The discussion is therefore based on research done with fewer build orientations than in this thesis. Consequently, mostly 0° and 90° build orientations are considered in the discussions.

5.1 Pores and fracture surface

5.1.1 0° tensile specimens

Shown with the yellow encircling in figure 4.2, every fracture surface except the 0-1 and 0-2 specimens had a classic nucleation of voids in the middle of the cross section, leading to an internal cavity with a square of shear lips around it. Here the crack initiation first occurs in the center of the specimen and then propagates to the surface [6, 12].

As can be seen in figure 4.2a and 4.2b the dimpled zone of the 0-1 and 0-2 specimens, unlike the others, stretches all the way to the outer edge of the specimens. This indicates that the crack initiation takes place at the edge of the specimens [36]. These crack initiation sites may be due to microscopic flaws such as cracks or pores, sharp corners, scratches and notches, as cracks usually initiate at the site with the highest stress concentration [6, 10]. There were not observed such initiation sites for the 0° specimens with SEM on the fracture surfaces. The roughness of the 0° specimens were also low compared to the others, as seen in table 4.1 (low R_a value meaning low roughness [13]). This indicates that it is not the surface itself, due to building orientation, that is the causation.

Since crack initiation at the surface took place for both 0° tensile specimens the effect this has on the mechanical properties, if any, is difficult to quantify. As this only happened to one of the groups, and to both of the specimens within the group, this can't be confirmed. Since this only happened to the 0° specimen, it cannot be ruled out that this has something to do with the build orientation. This may be further clarified and explained with a more thorough examination of both the fracture surface and the edge of the specimen at the initiation site itself.

5.1.2 45° tensile specimens

This group had the largest difference in elongation between the specimens. No large pores or other defects were found on the specimen with the lowest elongation, the 45-1 specimen, that could explain the difference between two specimens. It may therefore be caused by a undetected defect, or may be a part of the natural deviations inside the group.

5.1.3 Elongated pores, 0AS Charpy specimen

As can be seen in figure 4.10b and 4.10c the 0AS Charpy specimen had some large elongated pores on the fracture surface. The building direction is upwards in the pictures and the elongation of the pores are perpendicular to the loading direction. It is difficult to ratify the cause of origin of these pores. They both lay close to the surface of the specimen and may be caused by the laser turn-around point [39]. At this point the laser turns off, the melt pool collapses and freezes due to fast solidification [39]. This leaves pores which are elongated parallel with the building direction [39]. These elongated pores open up when 0° specimens are loaded, where as they close when 90° specimens are loaded [39]. This can lead to poorer mechanical properties in the 0° direction [39]. Pores like this were not observed on the fracture surface of any other specimens, tensile or Charpy. One of the reasons they are not observed in the other 0° specimens might be because they were removed by machining of the outer surface [39]. Another possibility is that they may not have existed at all in the other 0° specimens.

Elongated pores reduce the effective load-bearing area and cause stress concentrations resulting in reduction of mechanical properties [6, 11, 18, 38]. This should mean a lower impact toughness for the 0AS Charpy specimen compared to the others. The exact effect (e.g numerically) this has on the impact toughness, is hard to determine due to it only being observed in one specimen. Trends for the as-built and machined Charpy specimens are fairly similar. The 0MC specimen dose not have any elongated pores on the fracture surface. It can therefore be argued that elongated pores also has a small impact on the mechanical properties of the 0AS specimen.

The plastic deformation in ductile materials leads to a more uniform distribution of stress in vicinity to pores [6]. This can lead to the pores having a small effect on the mechanical properties [6]. The total combined size of the pores are small, and the load bearing surface is therefor only marginally reduced. This can explain why the absorbed impact energy of the 0AS specimen dose not deviate significantly from the trends seen in the Charpy specimens.

5.1.4 Elongated openings

On the fracture surface of every specimen, tensile and Charpy, opening that so far has been referred to as elongated openings, were found. These openings may look like the side view of elongated pores made due to insufficient melting, or they may look like microcracks due to the coalesce of microvoids [4, 38].

Elongated pores due to insufficient melting can be recognized by unmelted powder particles observable near the pores [14], and by their smooth surface [34, 41]. Elongated pores due to insufficient melting in Vilaro et al.[38] showed a smooth interior even when seen from the side. This is when they have the same form as the elongated openings. If studied closely, best seen in figure 4.12a and 4.12d, the roof and interior of the elongated openings has a dimpled surface, indicating ductile fracture, and not the smooth surface which is characteristic of pores [28, 34, 41]. There are also no unmelted powder particle observed near the pores.

Elongated pores due to insufficient melting also lead to anisotropy in the 0° and 90° specimens, for both tensile and Charpy [11, 18, 38, 41]. This is due to the detrimental way they are opened when loaded upon in the 90° direction [11, 18, 38, 41]. In Wu et al.[41] the elongated pores lead to an inferior impact toughness of

90° Charpy specimens, with almost a 100% difference from the 0° specimen (non-heat treated). In Vilaro et al. [38] higher elongation in the 0° tensile specimens compared to 90° specimen were observed, after the specimens were heat treated. In Wu et al.[41] and in Vilaro et al. [38] large smooth surfaces (length of 50-200 μm [38]) from elongated pores due to insufficient melting were observed on the 90° Charpy and tensile specimens respectively. In this thesis no such large elongated pores were observed on the surfaces of 90° specimen, Charpy or tensile. The difference in mechanical properties between the 0° and 90° build orientations were small. It should also be noted that these elongated openings in this thesis appear equally on the fracture surfaces independent of the build orientation.

The lack of smooth surfaces from the elongated pores on the 90° Charpy and tensile specimens indicate that the elongated opening observed are not elongated pores, and has some other explanation, e.g coalesce of microvoids into a microcrack. The small differences in mechanical properties between the 0° and 90° specimens, both tensile and Charpy, no signs of unmelted powder particles and the equal appearance on the fracture surface, regardless of build orientation, strengthens this hypothesis.

5.1.5 Energy difference between the two Charpy trends

The as-built and machined Charpy results show a similar trend, but with an energy difference in impact toughness. There were no significant difference in pores on the fracture surface of the as-built specimens compared to the machined ones, except for the 0AS. This indicates that the energy difference in impact toughness can not be explained by pores. Pores can be a part of small deviations in the two trends. The formation of pores, their position and size, seen on the fracture surface seems too randomized to be able to cause this energy difference, which is held throughout both trends.

It was shown by Yasa et al. [52] that the roughness of the as-built surface does not behave like stress-concentrating notches. Additionally, Yasa et al. [52] found that the difference between 0° and 90° specimens ”does not play an important role on the Charpy impact toughness results if the connection between successive layers is well established without any directional porosity”. This matches the small difference in absorbed energy seen between the 0° and 90° Charpy specimens in this thesis. Another explanation for the energy difference may be the difference between notch-radius size of as-built and machined Charpy specimens, as a smaller notch-radius has been shown to lead to a lower absorbed energy for Charpy specimens at room temperature [22].

5.1.6 Effect of pores

Cracks preferentially goes through the network of pores and propagate along the alignment of the pores [34]. As there were overall few pores on the fracture surface of all the specimens this indicates that pores played a small role in the fracture mechanism of the specimens. The stress concentrating effect of pores are small for ductile materials [6]. The plastic deformation in ductile materials leads to a uniform distribution of stress in vicinity to the pores [6]. This could mean that the pores have a small effect on the mechanical properties.

The influence of spherical pores on mechanical properties are expected to be independent of the loading direction [18]. Their morphology makes it indifferent of which direction they are pulled upon [18]. Since most of the pores on the fracture surface were spherical (except two elongated pores found on the 0AS specimen). It indicates that the pores does not lead to different mechanical properties with respect to build orientation.

5.2 Melt pool boundaries (MPBs)

The trends seen in elongation have similarities to trends in elongation of tensile specimen results found by W.Shifeng et al. [30]. In this thesis the elongation tops around the 60° orientation and then declines as it gets closer to the 0° and 90° build orientations. The trends in impact toughness also has similarities with theories of MPBs.

W.Shifeng et al. [30] found a large difference in elongation between the 0° and 90° tensile specimen. The 90° specimens have a higher number of slipping surfaces, leading to higher elongation [30]. This difference between the 0° and 90° is not the observed in tensile results in this thesis. In W.Shifeng et al. [30] the scan direction was not orientated between layers, giving large planes of track-track MPBs (as seen in figure 3.5). The results of different builds in the horizontal plane, i.e different θ_T angles (see figure 3.5), showed a difference in mechanical properties. Slipping of the specimens built in the horizontal plane was mainly attributed to the slipping along track–track MPBs [30]. This indicates that the angle of which the track-track MPBs is loaded upon is important, and that it can be affected by the scan strategy. A 67° scan strategy, changes the different melt pool orientations and mixes the melt pools [27]. It only produces the same direction for every 360 layer [27]. This would not give large planes with the same track-track MPBs orientations and could change the effect track-track MPBs has on slipping. The closer the angle gets to a 0° build orientation, the larger the effect of the 67° scan strategy should be, as the slipping along the layer-layer has less effect [30]. This on the other hand should not give the 0° specimens more slipping surfaces. The effect of the of 67° scan strategy should not have a large effect on the elongation in 90° specimens as it would pull upon both the layer-layer and track-track MPBs in a similar way. Thus the lack of difference between elongation of 0° and 90° specimens cannot be explained by the MPBs in accordance with the results of W.Shifeng et al.[30].

For the Charpy specimens the trends could be explained by the cracks tearing along the MPBs, as it follows the weaker regions in the material [1, 44]. According to *G.Lütjering and J.C.Williams (2007)*[24], Ti_3Al is brittle, which leads to easy and fast crack propagation through it. The trend for the Charpy specimens could be explained by the crack having to propagate through more material as the length of crack propagation through MPBs changes with the build orientation, shown with the red line in figure 5.1 [25]. A fracture would need more energy as the crack would have to propagate through more material.

For Maconachie et al. [25] ($AlSi10Mg$) the fracture surface of the 0° tensile specimen, when propagating through the MPBs, resulted in a 45° angle of the fracture surface, as shown in figure 5.1. This was not the case of the fracture surface in the 0° tensile specimens in this thesis. The fracture surface of every tensile specimen was relatively flat, with no incline except for on the shear lips. This is an indication that the cracks didn't propagate through MPBs. In this thesis there were no flat

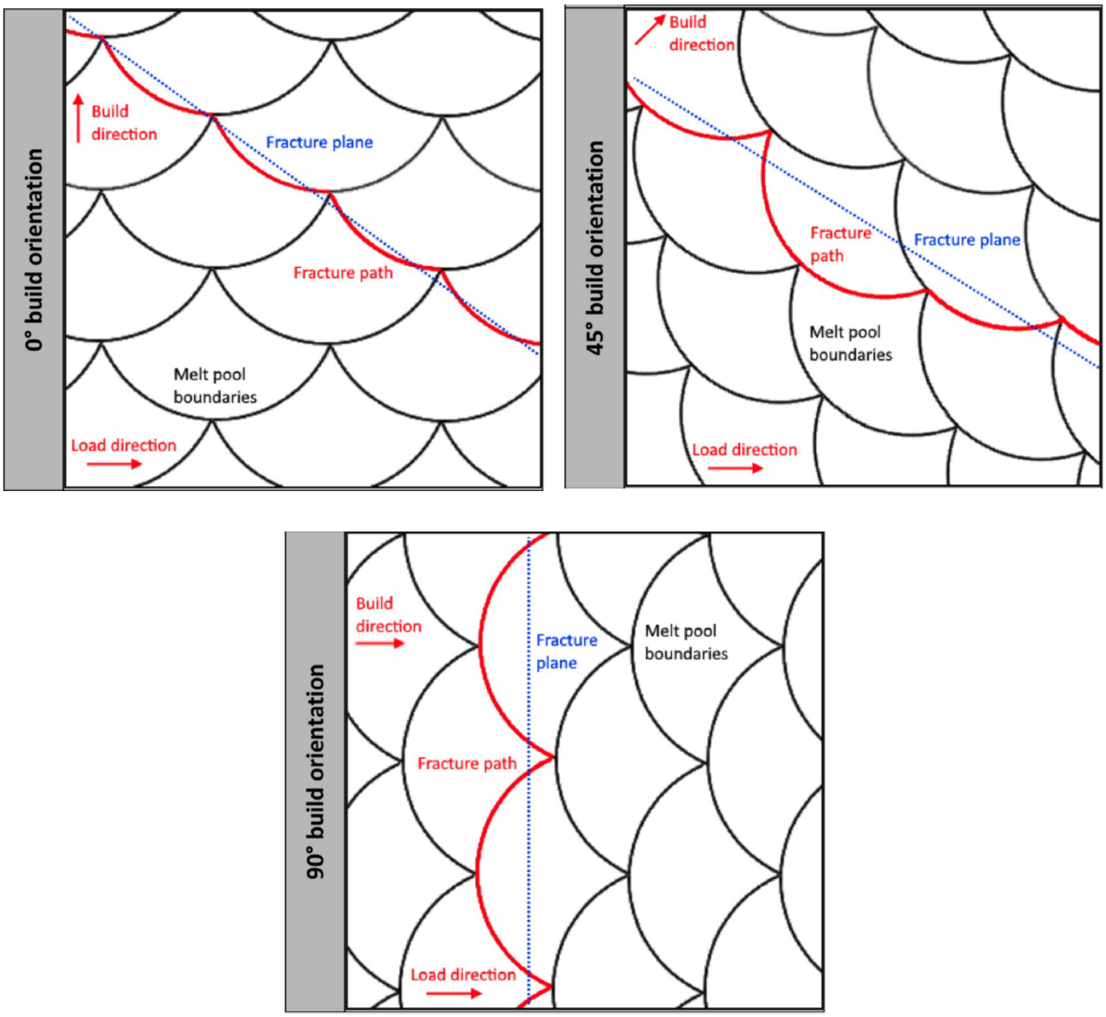

Figure 5.1: "Simplified schematic representation of melt pool boundaries and fracture paths for different build and load directions"[25]. Showing the fracture path in red and the fracture plane with blue dotted line.

surfaces indicating brittle fracture through MPBs in contrary to Xiong et al. [44] and Tang et al. [35].

Evidence from literature points to that the Ti_3Al, i.e MPBs, should disappear at heat treatment at $850°C$ [24, 47]. The Ti_3Al solvus temperature for Ti6Al4V is between $550°C$ and $600°C$, depending on the exact aluminum and oxygen content[24]. Consequently at temperatures above this, the Ti_3Al should disappear [24]. The temperature itself is more important than the time factor [24]. This could explain why Thijs et al.[37] and Yadroitsev et al.[47] could see MPBs of non-heat treated parts. While the MPBs could not be observed by Yadroitsev et al.[47] after heat treatment at 800-960°C. This makes it likely that the $850°C$ heat treatment used in this thesis has removed the MPBs. If the trends seen in the results were to be explained by MPBs, it would mean that the effect of MPBs still is present after the Ti_3Al (MPBs) has been dissolved by the heat treatment. Due to the effect of heat treatment, a small difference between elongation of 0° and 90° tensile specimens and the lack of flat, brittle, surfaces on the fracture surface, indicates that the resemblance between the elongation and Charpy impact toughness results and literature on MPBs is a mere "lucky" coincidence.

5.3 Microstructure

5.3.1 Martensite

Martensite is present in non-heat treated PBF-LB/M built Ti6Al4V [40, 42, 49, 54]. Research has shown that heat treatments above 800°C leads to full decomposition of the martensite [45, 54]. As it is brittle the presence of martensite leads to poor ductility, <10% [6, 7, 28, 29, 46, 50, 51, 54]. The heat treatment leads to decomposition of the martensite into a more coarse lamellar mixture of α and β phases [40, 45, 54], increasing the ductility, but reducing the strength [19, 40].

Since all the specimens in this thesis were heat treated at 850°C and the tensile results shows good ductility (above 10%) there is reasonable to assume that the martensite is gone.

5.3.2 Effect of columnar grains

Concerning the columnar prior β-grains, research shows that it remains intact beneath temperatures of 995°C [40, 42, 54]. Research done on the effect of columnar prior β-grains in Ti6Al4V has mainly focused on the effect of 0° and 90° specimens. The columnar grains yield higher elongation when load is applied parallel with the grains, i.e the 90° specimens, than perpendicular to the grains, i.e 0° specimens [28]. This difference in elongation between the 0° and 90° specimen is not seen in the tensile results. This is consistent with the results by Kumar et al. [21]. In Kumar et al. [21] the use of the exact same scanning parameters as used in this thesis lead to the prior β-grains becoming equiaxed in the horizontal plane and jagged and discontinuous in the vertical planes. This irregular arrangement of the prior β grains was caused by the slight mismatch between the melt pools from layer to layer due to the 67° rotational scanning. In Kumar et al. [21] this lead to small differences in yield strength and UTS with respect to the 0° and 90° build orientations and some insignificant difference in ductility. This correlates well with the results of the 0° and 90° specimens found in this thesis, indicating the same situation in this thesis. Since exactly the same scan parameters were used in Kumar et al. [21] this is reasonable to assume. Ch et al.[8] found, with PBF-LB/M of $AlSi_{10}Mg$, that the 67° rotational scanning strategy helps eliminate anisotropy in the mechanical properties and hindered crack propagation along the boundary of elongated grains. This would mean that the prior β-grain is not the cause of trends seen in elongation and in impact toughness in this thesis.

Chapter 6

Conclusion

In this thesis, the influence of different build orientation on tensile properties and Charpy impact toughness on PBF-LB/M built Ti6Al4V was studied.

The mechanical properties yield strength, elastic modulus and UTS, show small differences with respect to build orientation and isotropic behavior. There is anisotropy in the elongation with respect to build orientation, and trend can be seen, but not statistically differentiated. A similar trend of anisotropy is also present in the impact toughness, for specimens with an as-built and machined surface. To the authors knowledge, this trend has not been seen in published literature. The origin of the trend was investigated with respect to pores, MPBs and microstructure.

The impact of pores on the mechanical properties with respect to build orientation, was found to be insignificant. This is based on results of mechanical properties, the morphology of the pores and frequency of occurrence on fracture surfaces with respect to build orientation.

With support of published research it was concluded that the martensite, which is common in PBF-LB/M Ti6Al4V, was decomposed due to the heat treatment. It is likely, based on previous research, that MPBs and columnar prior β-grains are not deciding factors in the trends seen in elongation and impact toughness.

Published research together with the results at hand from the experiments performed, mainly the tensile tests, Charpy tests and SEM of the fracture surface, cannot completely explain the trends seen in elongation and impact toughness. It is therefore concluded that more research is needed to explain these trends. The origin of these trends may be found in the microstructure. As a suggestion for further work, pictures of the microstructure should be examined.

Bibliography

[1] Nesma T Aboulkhair et al. “Mechanical properties of selective laser melted AlSi10Mg: nano, micro, and macro properties”. In: *Proc. of Solid Freeform Fabrication Symposium*. Vol. 1. 2015, pp. 1–30.

[2] Dylan Agius et al. “Cyclic plasticity and microstructure of as-built SLM Ti-6Al-4V: The effect of build orientation”. In: *Materials Science and Engineering: A* 701 (2017), pp. 85–100.

[3] T Ahmed and HJ Rack. “Phase transformations during cooling in $\alpha+\ \beta$ titanium alloys”. In: *Materials Science and Engineering: A* 243.1-2 (1998), pp. 206–211.

[4] Hooyar Attar et al. “Manufacture by selective laser melting and mechanical behavior of commercially pure titanium”. In: *Materials Science and Engineering: A* 593 (2014), pp. 170–177.

[5] D Buchbinder et al. “Selective laser melting of aluminum die-cast alloy—Correlations between process parameters, solidification conditions, and resulting mechanical properties”. In: *Journal of Laser Applications* 27.S2 (2015), S29205.

[6] William D Callister and David G Rethwisch. *Materials science and engineering*. John wiley, 2014.

[7] Sheng Cao et al. “Role of martensite decomposition in tensile properties of selective laser melted Ti-6Al-4V”. In: *Journal of Alloys and Compounds* 744 (2018), pp. 357–363.

[8] Srinivasa Rakesh Ch et al. “Influence of working environment and built orientation on the tensile properties of selective laser melted AlSi10Mg alloy”. In: *Materials Science and Engineering: A* 750 (2019), pp. 141–151.

[9] Haijun Gong et al. “Analysis of defect generation in Ti–6Al–4V parts made using powder bed fusion additive manufacturing processes”. In: *Additive Manufacturing* 1 (2014), pp. 87–98.

[10] Haijun Gong et al. “Effect of defects on fatigue tests of as-built Ti-6Al-4V parts fabricated by selective laser melting”. In: *Solid freeform fabrication symposium*. University of Texas Austin, Texas. 2012, pp. 499–506.

[11] Haijun Gong et al. “Influence of defects on mechanical properties of Ti–6Al–4 V components produced by selective laser melting and electron beam melting”. In: *Materials & Design* 86 (2015), pp. 545–554.

[12] Jorge Luis González-Velázquez. *Fractography and failure analysis*. Vol. 3. Springer, 2018.

[13] Mikell P Groover. *Fundamentals of modern manufacturing: materials, processes, and systems*. John Wiley & Sons, 2020.

[14] Patrick Hartunian and Mohsen Eshraghi. "Effect of build orientation on the microstructure and mechanical properties of selective laser-melted Ti-6Al-4V alloy". In: *Journal of Manufacturing and Materials Processing* 2.4 (2018), p. 69.

[15] Instron. *Motorized pendelum impact testing system*. URL: `https://www.instron.us/products/testing-systems/impact-systems/pendulums/-/media/literature-library/products/2014/08/motorized-pendulum-impact-testing-system-mpx-systems.pdf#page=2` (visited on 11/16/2020).

[16] A ISO. "ISO/ASTM 52900-1: 2019 Additive manufacturing Part 1: Laser-based powder bed fusion of metals". In: *ASTM 52911* (2019).

[17] A ISO. "ISO/ASTM 52900: 2015 additive manufacturing-general principles terminology". In: *ASTM F2792-10e1* (2015).

[18] Galina Kasperovich et al. "Correlation between porosity and processing parameters in TiAl6V4 produced by selective laser melting". In: *Materials & Design* 105 (2016), pp. 160–170.

[19] AmirMahyar Khorasani et al. "On the role of different annealing heat treatments on mechanical properties and microstructure of selective laser melted and conventional wrought Ti-6Al-4V". In: *Rapid Prototyping Journal* (2017).

[20] Jean-Pierre Kruth et al. "Part and material properties in selective laser melting of metals". In: *Proceedings of the 16th International Symposium on Electromachining (ISEM XVI)*. SHANGHAI JIAO TONG UNIV PRESS. 2010, pp. 3–14.

[21] Punit Kumar, Om Prakash, and Upadrasta Ramamurty. "Micro-and meso-structures and their influence on mechanical properties of selectively laser melted Ti-6Al-4V". In: *Acta Materialia* 154 (2018), pp. 246–260.

[22] Hiroaki Kurishita et al. "Effects of V-notch dimensions on Charpy impact test results for differently sized miniature specimens of ferritic steel". In: *Materials Transactions, JIM* 34.11 (1993), pp. 1042–1052.

[23] G Løvås Gunnar. *Statistikk for universiteter og høgskoler*. 2011.

[24] Gerd Lütjering and James C Williams. *Titanium*. Springer Science & Business Media, 2007.

[25] Tobias Maconachie et al. "Effect of build orientation on the quasi-static and dynamic response of SLM AlSi10Mg". In: *Materials Science and Engineering: A* 788 (2020), p. 139445.

[26] Adrian P Mouritz. *Introduction to aerospace materials*. Elsevier, 2012.

[27] JA Pakkanen. "Designing for Additive Manufacturing-Product and Process Driven Design for Metals and Polymers". In: *Politecnico di Torino* (2018).

[28] Chunlei Qiu, Nicholas JE Adkins, and Moataz M Attallah. "Microstructure and tensile properties of selectively laser-melted and of HIPed laser-melted Ti–6Al–4V". In: *Materials Science and Engineering: A* 578 (2013), pp. 230–239.

[29] HK Rafi et al. “Microstructures and mechanical properties of Ti6Al4V parts fabricated by selective laser melting and electron beam melting”. In: *Journal of materials engineering and performance* 22.12 (2013), pp. 3872–3883.

[30] Wen Shifeng et al. “Effect of molten pool boundaries on the mechanical properties of selective laser melting parts”. In: *Journal of Materials Processing Technology* 214.11 (2014), pp. 2660–2667.

[31] Marco Simonelli, Yau Yau Tse, and Chris Tuck. “On the texture formation of selective laser melted Ti-6Al-4V”. In: *Metallurgical and Materials Transactions A* 45.6 (2014), pp. 2863–2872.

[32] Marco Simonelli, Yau Yau Tse, and Christopher Tuck. “Effect of the build orientation on the mechanical properties and fracture modes of SLM Ti–6Al–4V”. In: *Materials Science and Engineering: A* 616 (2014), pp. 1–11.

[33] Marco Simonelli, Yau Yau Tse, and Christopher Tuck. “Microstructure of Ti-6Al-4V produced by selective laser melting”. In: *Journal of Physics: Conference Series*. Vol. 371. 1. IOP Publishing. 2012, p. 012084.

[34] Jonathan Stef et al. “Mechanism of porosity formation and influence on mechanical properties in selective laser melting of Ti-6Al-4V parts”. In: *Materials & Design* 156 (2018), pp. 480–493.

[35] Ming Tang and Petrus Christiaan Pistorius. “Anisotropic mechanical behavior of AlSi10Mg parts produced by selective laser melting”. In: *Jom* 69.3 (2017), pp. 516–522.

[36] Pan Tao et al. “Tensile behavior of Ti-6Al-4V alloy fabricated by selective laser melting: Effects of microstructures and as-built surface quality”. In: *China Foundry* 15.4 (2018), pp. 243–252.

[37] Lore Thijs et al. “A study of the microstructural evolution during selective laser melting of Ti–6Al–4V”. In: *Acta materialia* 58.9 (2010), pp. 3303–3312.

[38] Thomas Vilaro, Christophe Colin, and Jean-Dominique Bartout. “As-fabricated and heat-treated microstructures of the Ti-6Al-4V alloy processed by selective laser melting”. In: *Metallurgical and materials transactions A* 42.10 (2011), pp. 3190–3199.

[39] Thomas Voisin et al. “Defects-dictated tensile properties of selective laser melted Ti-6Al-4V”. In: *Materials & Design* 158 (2018), pp. 113–126.

[40] Bey Vrancken et al. “Heat treatment of Ti6Al4V produced by Selective Laser Melting: Microstructure and mechanical properties”. In: *Journal of Alloys and Compounds* 541 (2012), pp. 177–185.

[41] Ming-Wei Wu, Pang-Hsin Lai, and Jhewn-Kuang Chen. “Anisotropy in the impact toughness of selective laser melted Ti–6Al–4V alloy”. In: *Materials Science and Engineering: A* 650 (2016), pp. 295–299.

[42] SQ Wu et al. “Microstructural evolution and microhardness of a selective-laser-melted Ti–6Al–4V alloy after post heat treatments”. In: *Journal of Alloys and Compounds* 672 (2016), pp. 643–652.

[43] Zongyu Xie et al. “Effects of selective laser melting build orientations on the microstructure and tensile performance of Ti–6Al–4V alloy”. In: *Materials Science and Engineering: A* 776 (2020), p. 139001.

[44] ZH Xiong et al. "Role of melt pool boundary condition in determining the mechanical properties of selective laser melting AlSi10Mg alloy". In: *Materials Science and Engineering: A* 740 (2019), pp. 148–156.

[45] Wei Xu et al. "In situ tailoring microstructure in additively manufactured Ti-6Al-4V for superior mechanical performance". In: *Acta Materialia* 125 (2017), pp. 390–400.

[46] Wei Xu et al. "Ti-6Al-4V additively manufactured by selective laser melting with superior mechanical properties". In: *Jom* 67.3 (2015), pp. 668–673.

[47] Igor Yadroitsev, Pavel Krakhmalev, and I Yadroitsava. "Selective laser melting of Ti6Al4V alloy for biomedical applications: Temperature monitoring and microstructural evolution". In: *Journal of Alloys and Compounds* 583 (2014), pp. 404–409.

[48] Xingchen Yan et al. "Effect of heat treatment on the phase transformation and mechanical properties of Ti6Al4V fabricated by selective laser melting". In: *Journal of Alloys and Compounds* 764 (2018), pp. 1056–1071.

[49] Jingjing Yang et al. "Effect of crystallographic orientation on mechanical anisotropy of selective laser melted Ti-6Al-4V alloy". In: *Materials Characterization* 127 (2017), pp. 137–145.

[50] Jingjing Yang et al. "Formation and control of martensite in Ti-6Al-4V alloy produced by selective laser melting". In: *Materials & Design* 108 (2016), pp. 308–318.

[51] Jingjing Yang et al. "Role of molten pool mode on formability, microstructure and mechanical properties of selective laser melted Ti-6Al-4V alloy". In: *Materials & Design* 110 (2016), pp. 558–570.

[52] Evren Yasa et al. "Charpy impact testing of metallic selective laser melting parts". In: *Virtual and physical prototyping* 5.2 (2010), pp. 89–98.

[53] Tao Zhang et al. "Evolution of molten pool during selective laser melting of Ti–6Al–4V". In: *Journal of Physics D: Applied Physics* 52.5 (2018), p. 055302.

[54] Xiang-Yu Zhang et al. "Effect of subtransus heat treatment on the microstructure and mechanical properties of additively manufactured Ti-6Al-4V alloy". In: *Journal of Alloys and Compounds* 735 (2018), pp. 1562–1575.

[55] Suyuan Zhou et al. "Impacts of defocusing amount and molten pool boundaries on mechanical properties and microstructure of selective laser melted AlSi10Mg". In: *Materials* 12.1 (2019), p. 73.

Appendices

A Specimen measurments

Table 6.1: Measurements of tensile specimens [mm] and the calculated real area used in tensile strength calculations [mm^2].

Specimen	Width1	Width2	Width3	Depth1	Depth2	Depth3	Average Width	Average Depth	Area
0-1	4.088	4.087	4.069	4.519	4.508	4.500	4.081	4.509	18.401
0-2	4.090	4.087	4.098	4.551	4.538	4.543	4.092	4.544	18.594
15-1	4.101	4.095	4.086	4.510	4.508	4.483	4.094	4.500	18.423
15-2	4.099	4.079	4.081	4.523	4.522	4.541	4.086	4.529	18.505
30-1	4.094	4.102	4.090	4.557	4.553	4.554	4.095	4.555	18.653
30-2	4.095	4.083	4.069	4.509	4.516	4.518	4.082	4.514	18.426
45-1	4.096	4.092	4.063	4.495	4.491	4.494	4.084	4.493	18.349
45-2	4.081	4.082	4.091	4.464	4.474	4.486	4.085	4.475	18.280
60-1	4.051	4.064	4.070	4.550	4.526	4.520	4.062	4.532	18.409
60-2	4.105	4.078	4.073	4.530	4.517	4.510	4.085	4.519	18.460
75-1	4.099	4.090	4.072	4.481	4.477	4.463	4.087	4.474	18.285
75-2	4.093	4.092	4.071	4.518	4.533	4.524	4.085	4.525	18.485
90-1	4.090	4.095	4.088	4.511	4.517	4.522	4.091	4.517	18.479
90-2	4.092	4.088	4.070	4.532	4.542	4.546	4.083	4.540	18.537

Table 6.2: Measurements of Charpy as-built specimens [mm].

Specimen	Width1	Width2	Width3	Depth1	Depth2	Depth3	Average Width	Average Depth
0	10.092	10.106	10.088	10.049	10.026	10.004	10.095	10.026
15	10.041	10.092	10.045	10.007	10.029	9.988	10.059	10.008
30	10.082	10.055	10.056	10.005	10.015	9.999	10.064	10.006
45	10.010	10.025	10.061	9.993	10.016	10.051	10.032	10.020
60	10.056	10.092	10.089	10.063	10.067	10.057	10.079	10.062
75	10.071	10.065	10.071	10.070	10.085	10.085	10.069	10.080
90	10.082	10.080	10.102	10.062	10.096	10.090	10.088	10.083

Table 6.3: Measurements of Charpy machined specimens [mm].

Specimen	Width1	Width2	Width3	Depth1	Depth2	Depth3	Average Width	Average Depth
0	10.033	10.034	10.042	10.019	10.023	10.015	10.036	10.019
15	10.020	10.029	10.042	10.051	10.043	10.260	10.030	10.118
30	10.067	10.030	10.026	10.007	9.999	9.976	10.041	9.994
45	10.085	10.085	10.079	10.039	10.038	10.036	10.083	10.038
60	10.040	10.025	10.033	10.060	10.040	10.021	10.033	10.040
75	10.082	10.069	10.068	10.084	10.069	10.040	10.073	10.064
90	10.080	10.074	10.073	10.019	10.011	10.007	10.076	10.012

B Roughness measurements, Charpy

As-built

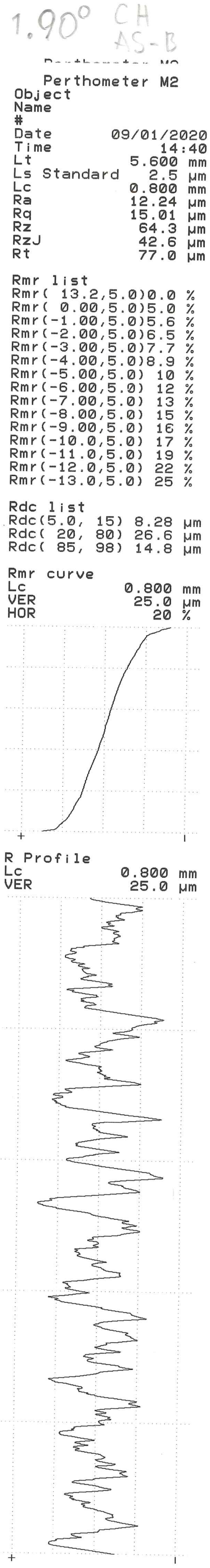

1.90° CH
AS-B

```
  Perthometer M2
Object
Name
#
Date          09/01/2020
Time               14:40
Lt              5.600 mm
Ls Standard       2.5 µm
Lc              0.800 mm
Ra              12.24 µm
Rq              15.01 µm
Rz               64.3 µm
RzJ              42.6 µm
Rt               77.0 µm

Rmr list
Rmr( 13.2,5.0)0.0 %
Rmr( 0.00,5.0)5.0 %
Rmr(-1.00,5.0)5.6 %
Rmr(-2.00,5.0)6.5 %
Rmr(-3.00,5.0)7.7 %
Rmr(-4.00,5.0)8.9 %
Rmr(-5.00,5.0) 10 %
Rmr(-6.00,5.0) 12 %
Rmr(-7.00,5.0) 13 %
Rmr(-8.00,5.0) 15 %
Rmr(-9.00,5.0) 16 %
Rmr(-10.0,5.0) 17 %
Rmr(-11.0,5.0) 19 %
Rmr(-12.0,5.0) 22 %
Rmr(-13.0,5.0) 25 %

Rdc list
Rdc(5.0, 15) 8.28 µm
Rdc( 20, 80) 26.6 µm
Rdc( 85, 98) 14.8 µm

Rmr curve
Lc             0.800 mm
VER             25.0 µm
HOR               20 %

R Profile
Lc             0.800 mm
VER             25.0 µm
```

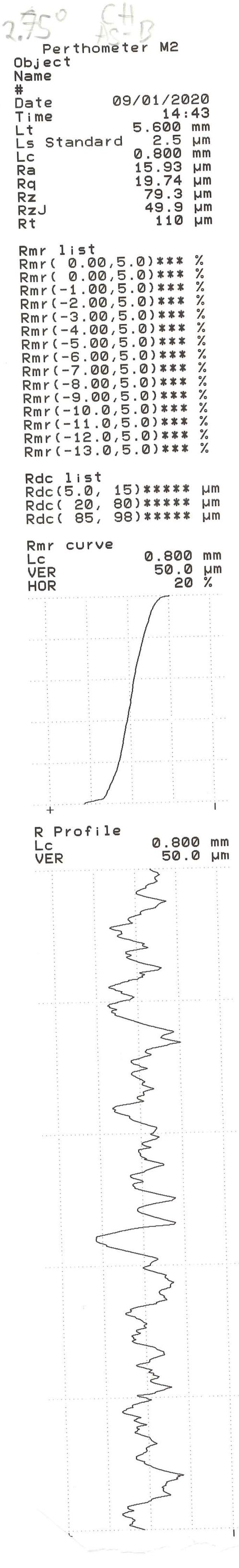

2.75° CH
AS-B

```
  Perthometer M2
Object
Name
#
Date          09/01/2020
Time               14:43
Lt              5.600 mm
Ls Standard       2.5 µm
Lc              0.800 mm
Ra              15.93 µm
Rq              19.74 µm
Rz               79.3 µm
RzJ              49.9 µm
Rt                110 µm

Rmr list
Rmr( 0.00,5.0)*** %
Rmr( 0.00,5.0)*** %
Rmr(-1.00,5.0)*** %
Rmr(-2.00,5.0)*** %
Rmr(-3.00,5.0)*** %
Rmr(-4.00,5.0)*** %
Rmr(-5.00,5.0)*** %
Rmr(-6.00,5.0)*** %
Rmr(-7.00,5.0)*** %
Rmr(-8.00,5.0)*** %
Rmr(-9.00,5.0)*** %
Rmr(-10.0,5.0)*** %
Rmr(-11.0,5.0)*** %
Rmr(-12.0,5.0)*** %
Rmr(-13.0,5.0)*** %

Rdc list
Rdc(5.0, 15)***** µm
Rdc( 20, 80)***** µm
Rdc( 85, 98)***** µm

Rmr curve
Lc             0.800 mm
VER             50.0 µm
HOR               20 %

R Profile
Lc             0.800 mm
VER             50.0 µm
```

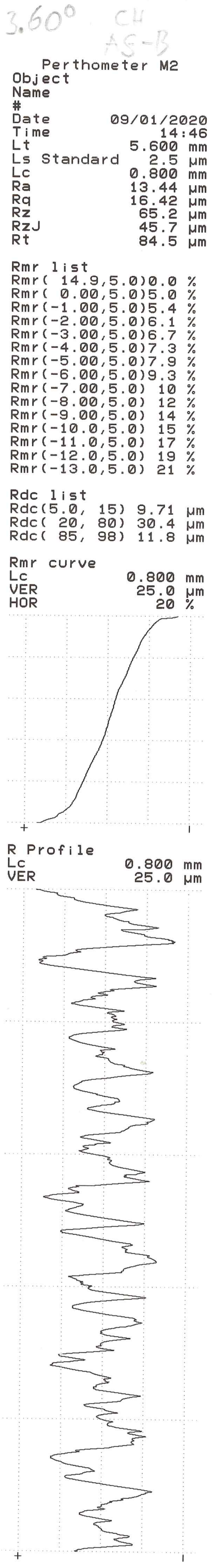

3.60° CH
AS-B

```
  Perthometer M2
Object
Name
#
Date          09/01/2020
Time               14:46
Lt              5.600 mm
Ls Standard       2.5 µm
Lc              0.800 mm
Ra              13.44 µm
Rq              16.42 µm
Rz               65.2 µm
RzJ              45.7 µm
Rt               84.5 µm

Rmr list
Rmr( 14.9,5.0)0.0 %
Rmr( 0.00,5.0)5.0 %
Rmr(-1.00,5.0)5.4 %
Rmr(-2.00,5.0)6.1 %
Rmr(-3.00,5.0)6.7 %
Rmr(-4.00,5.0)7.3 %
Rmr(-5.00,5.0)7.9 %
Rmr(-6.00,5.0)9.3 %
Rmr(-7.00,5.0) 10 %
Rmr(-8.00,5.0) 12 %
Rmr(-9.00,5.0) 14 %
Rmr(-10.0,5.0) 15 %
Rmr(-11.0,5.0) 17 %
Rmr(-12.0,5.0) 19 %
Rmr(-13.0,5.0) 21 %

Rdc list
Rdc(5.0, 15) 9.71 µm
Rdc( 20, 80) 30.4 µm
Rdc( 85, 98) 11.8 µm

Rmr curve
Lc             0.800 mm
VER             25.0 µm
HOR               20 %

R Profile
Lc             0.800 mm
VER             25.0 µm
```

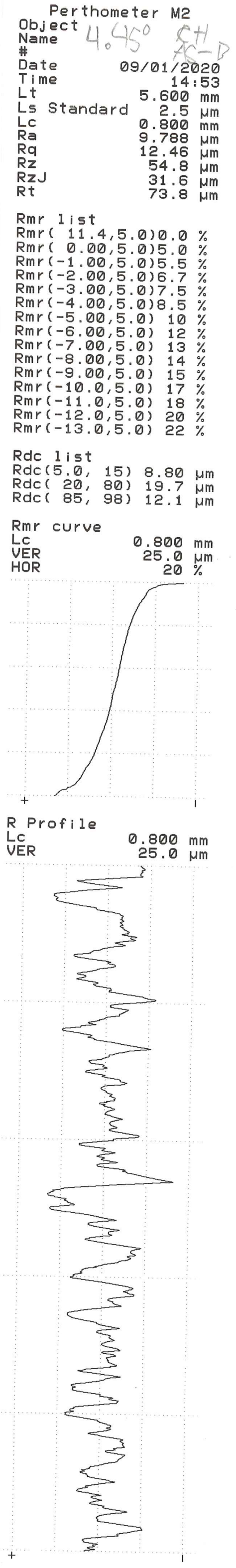

4.45° CH
AS-B

```
  Perthometer M2
Object
Name
#
Date          09/01/2020
Time               14:53
Lt              5.600 mm
Ls Standard       2.5 µm
Lc              0.800 mm
Ra              9.788 µm
Rq              12.46 µm
Rz               54.8 µm
RzJ              31.6 µm
Rt               73.8 µm

Rmr list
Rmr( 11.4,5.0)0.0 %
Rmr( 0.00,5.0)5.0 %
Rmr(-1.00,5.0)5.5 %
Rmr(-2.00,5.0)6.7 %
Rmr(-3.00,5.0)7.5 %
Rmr(-4.00,5.0)8.5 %
Rmr(-5.00,5.0) 10 %
Rmr(-6.00,5.0) 12 %
Rmr(-7.00,5.0) 13 %
Rmr(-8.00,5.0) 14 %
Rmr(-9.00,5.0) 15 %
Rmr(-10.0,5.0) 17 %
Rmr(-11.0,5.0) 18 %
Rmr(-12.0,5.0) 20 %
Rmr(-13.0,5.0) 22 %

Rdc list
Rdc(5.0, 15) 8.80 µm
Rdc( 20, 80) 19.7 µm
Rdc( 85, 98) 12.1 µm

Rmr curve
Lc             0.800 mm
VER             25.0 µm
HOR               20 %

R Profile
Lc             0.800 mm
VER             25.0 µm
```

1.90° CH
AS-B

```
    Perthometer M2
Object
Name
#
Date          09/01/2020
Time               14:40
Lt              5.600 mm
Ls Standard       2.5 µm
Lc              0.800 mm
Ra              12.24 µm
Rq              15.01 µm
Rz               64.3 µm
RzJ              42.6 µm
Rt               77.0 µm

Rmr list
Rmr( 13.2,5.0)0.0 %
Rmr( 0.00,5.0)5.0 %
Rmr(-1.00,5.0)5.6 %
Rmr(-2.00,5.0)6.5 %
Rmr(-3.00,5.0)7.7 %
Rmr(-4.00,5.0)8.9 %
Rmr(-5.00,5.0) 10 %
Rmr(-6.00,5.0) 12 %
Rmr(-7.00,5.0) 13 %
Rmr(-8.00,5.0) 15 %
Rmr(-9.00,5.0) 16 %
Rmr(-10.0,5.0) 17 %
Rmr(-11.0,5.0) 19 %
Rmr(-12.0,5.0) 22 %
Rmr(-13.0,5.0) 25 %

Rdc list
Rdc(5.0, 15) 8.28 µm
Rdc( 20, 80) 26.6 µm
Rdc( 85, 98) 14.8 µm

Rmr curve
Lc              0.800 mm
VER              25.0 µm
HOR                20 %
```

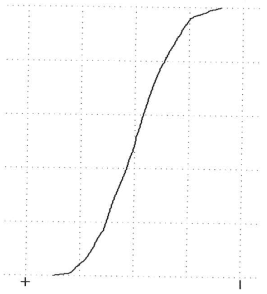

```
R Profile
Lc              0.800 mm
VER              25.0 µm
```

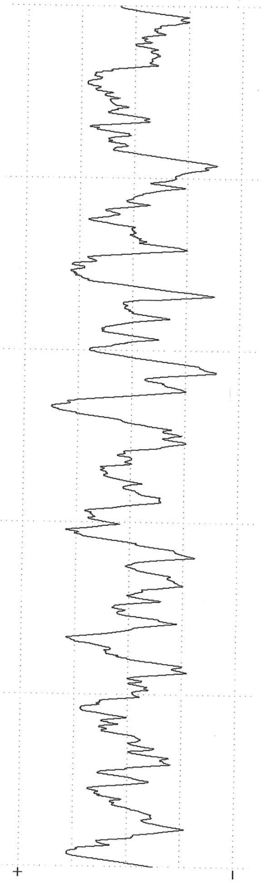

2.75° CH
AS-B

```
    Perthometer M2
Object
Name
#
Date          09/01/2020
Time               14:43
Lt              5.600 mm
Ls Standard       2.5 µm
Lc              0.800 mm
Ra              15.93 µm
Rq              19.74 µm
Rz               79.3 µm
RzJ              49.9 µm
Rt                110 µm

Rmr list
Rmr( 0.00,5.0)*** %
Rmr( 0.00,5.0)*** %
Rmr(-1.00,5.0)*** %
Rmr(-2.00,5.0)*** %
Rmr(-3.00,5.0)*** %
Rmr(-4.00,5.0)*** %
Rmr(-5.00,5.0)*** %
Rmr(-6.00,5.0)*** %
Rmr(-7.00,5.0)*** %
Rmr(-8.00,5.0)*** %
Rmr(-9.00,5.0)*** %
Rmr(-10.0,5.0)*** %
Rmr(-11.0,5.0)*** %
Rmr(-12.0,5.0)*** %
Rmr(-13.0,5.0)*** %

Rdc list
Rdc(5.0, 15)***** µm
Rdc( 20, 80)***** µm
Rdc( 85, 98)***** µm

Rmr curve
Lc              0.800 mm
VER              50.0 µm
HOR                20 %
```

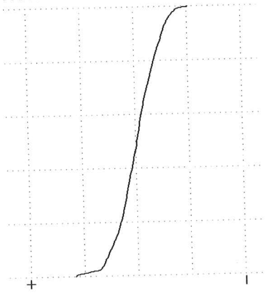

```
R Profile
Lc              0.800 mm
VER              50.0 µm
```

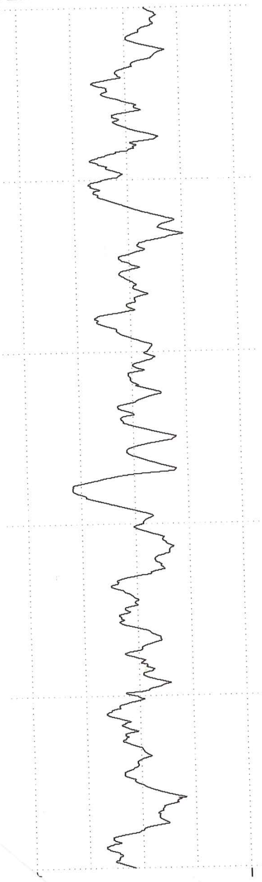

3.60° CH
AS-B

```
    Perthometer M2
Object
Name
#
Date          09/01/2020
Time               14:46
Lt              5.600 mm
Ls Standard       2.5 µm
Lc              0.800 mm
Ra              13.44 µm
Rq              16.42 µm
Rz               65.2 µm
RzJ              45.7 µm
Rt               84.5 µm

Rmr list
Rmr( 14.9,5.0)0.0 %
Rmr( 0.00,5.0)5.0 %
Rmr(-1.00,5.0)5.4 %
Rmr(-2.00,5.0)6.1 %
Rmr(-3.00,5.0)6.7 %
Rmr(-4.00,5.0)7.3 %
Rmr(-5.00,5.0)7.9 %
Rmr(-6.00,5.0)9.3 %
Rmr(-7.00,5.0) 10 %
Rmr(-8.00,5.0) 12 %
Rmr(-9.00,5.0) 14 %
Rmr(-10.0,5.0) 15 %
Rmr(-11.0,5.0) 17 %
Rmr(-12.0,5.0) 19 %
Rmr(-13.0,5.0) 21 %

Rdc list
Rdc(5.0, 15) 9.71 µm
Rdc( 20, 80) 30.4 µm
Rdc( 85, 98) 11.8 µm

Rmr curve
Lc              0.800 mm
VER              25.0 µm
HOR                20 %
```

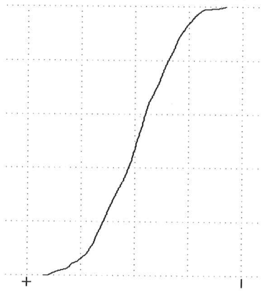

```
R Profile
Lc              0.800 mm
VER              25.0 µm
```

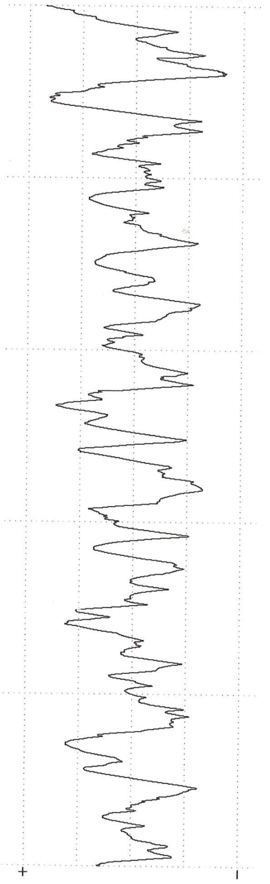

4.45° CH
AS-B

```
    Perthometer M2
Object
Name
#
Date          09/01/2020
Time               14:53
Lt              5.600 mm
Ls Standard       2.5 µm
Lc              0.800 mm
Ra              9.788 µm
Rq              12.46 µm
Rz               54.8 µm
RzJ              31.6 µm
Rt               73.8 µm

Rmr list
Rmr( 11.4,5.0)0.0 %
Rmr( 0.00,5.0)5.0 %
Rmr(-1.00,5.0)5.5 %
Rmr(-2.00,5.0)6.7 %
Rmr(-3.00,5.0)7.5 %
Rmr(-4.00,5.0)8.5 %
Rmr(-5.00,5.0) 10 %
Rmr(-6.00,5.0) 12 %
Rmr(-7.00,5.0) 13 %
Rmr(-8.00,5.0) 14 %
Rmr(-9.00,5.0) 15 %
Rmr(-10.0,5.0) 17 %
Rmr(-11.0,5.0) 18 %
Rmr(-12.0,5.0) 20 %
Rmr(-13.0,5.0) 22 %

Rdc list
Rdc(5.0, 15) 8.80 µm
Rdc( 20, 80) 19.7 µm
Rdc( 85, 98) 12.1 µm

Rmr curve
Lc              0.800 mm
VER              25.0 µm
HOR                20 %
```

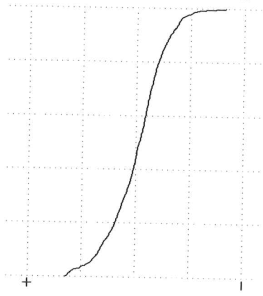

```
R Profile
Lc              0.800 mm
VER              25.0 µm
```

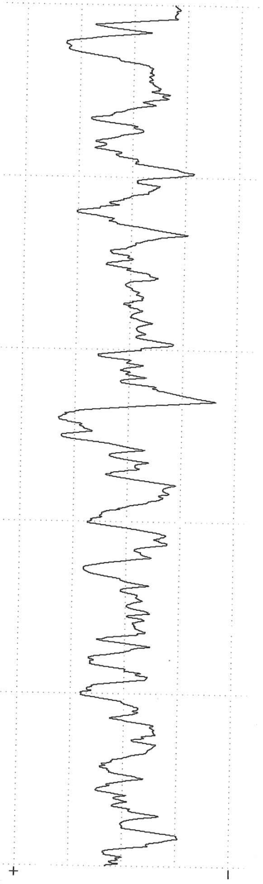

Machined

1.90°

CH
M

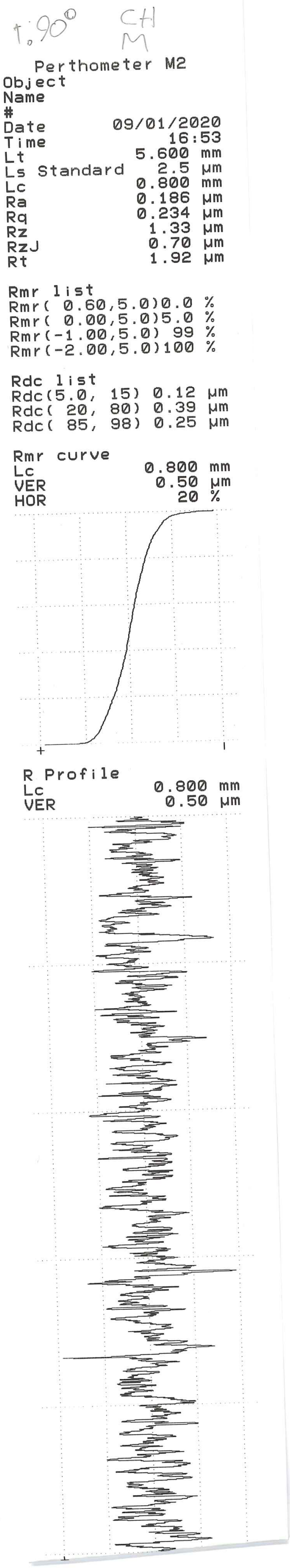

```
   Perthometer M2
Object
Name
#
Date          09/01/2020
Time               16:53
Lt               5.600 mm
Ls Standard        2.5 µm
Lc               0.800 mm
Ra               0.186 µm
Rq               0.234 µm
Rz                1.33 µm
RzJ               0.70 µm
Rt                1.92 µm

Rmr list
Rmr( 0.60,5.0)0.0 %
Rmr( 0.00,5.0)5.0 %
Rmr(-1.00,5.0) 99 %
Rmr(-2.00,5.0)100 %

Rdc list
Rdc(5.0, 15) 0.12 µm
Rdc( 20, 80) 0.39 µm
Rdc( 85, 98) 0.25 µm

Rmr curve
Lc               0.800 mm
VER               0.50 µm
HOR                 20 %

R Profile
Lc               0.800 mm
VER               0.50 µm
```

2,75°

CH
M

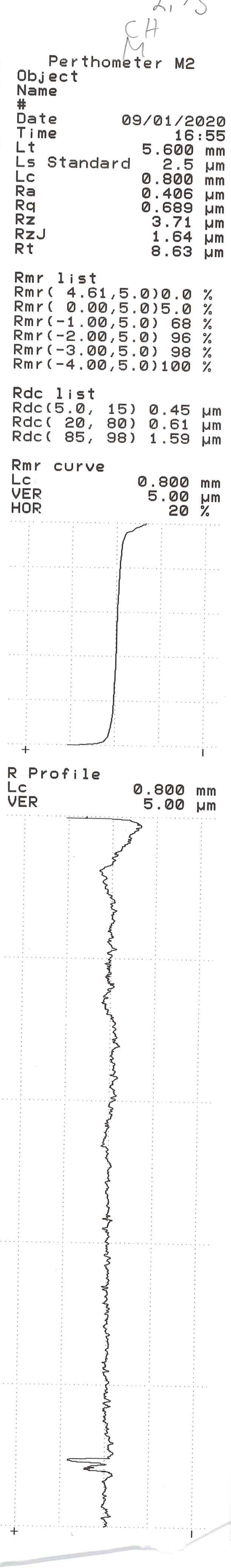

```
   Perthometer M2
Object
Name
#
Date          09/01/2020
Time               16:55
Lt               5.600 mm
Ls Standard        2.5 µm
Lc               0.800 mm
Ra               0.406 µm
Rq               0.689 µm
Rz                3.71 µm
RzJ               1.64 µm
Rt                8.63 µm

Rmr list
Rmr( 4.61,5.0)0.0 %
Rmr( 0.00,5.0)5.0 %
Rmr(-1.00,5.0) 68 %
Rmr(-2.00,5.0) 96 %
Rmr(-3.00,5.0) 98 %
Rmr(-4.00,5.0)100 %

Rdc list
Rdc(5.0, 15) 0.45 µm
Rdc( 20, 80) 0.61 µm
Rdc( 85, 98) 1.59 µm

Rmr curve
Lc               0.800 mm
VER               5.00 µm
HOR                 20 %

R Profile
Lc               0.800 mm
VER               5.00 µm
```

3.60°

CH
M

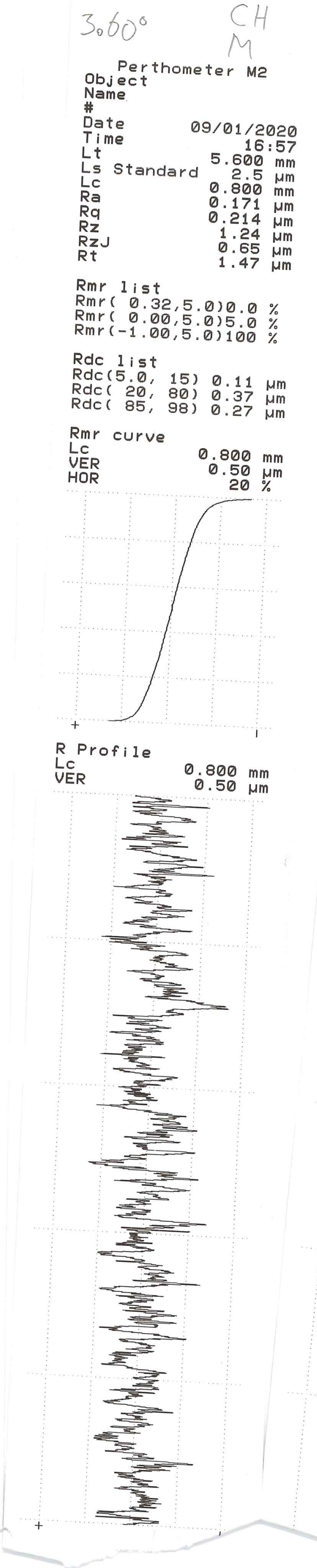

```
   Perthometer M2
Object
Name
#
Date          09/01/2020
Time               16:57
Lt               5.600 mm
Ls Standard        2.5 µm
Lc               0.800 mm
Ra               0.171 µm
Rq               0.214 µm
Rz                1.24 µm
RzJ               0.65 µm
Rt                1.47 µm

Rmr list
Rmr( 0.32,5.0)0.0 %
Rmr( 0.00,5.0)5.0 %
Rmr(-1.00,5.0)100 %

Rdc list
Rdc(5.0, 15) 0.11 µm
Rdc( 20, 80) 0.37 µm
Rdc( 85, 98) 0.27 µm

Rmr curve
Lc               0.800 mm
VER               0.50 µm
HOR                 20 %

R Profile
Lc               0.800 mm
VER               0.50 µm
```

4.45°

CH
M

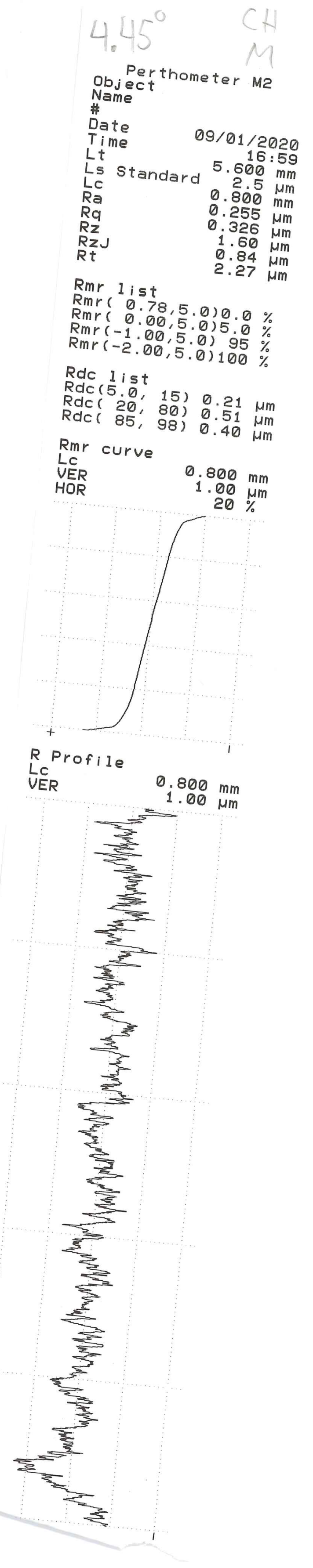

```
   Perthometer M2
Object
Name
#
Date          09/01/2020
Time               16:59
Lt               5.600 mm
Ls Standard        2.5 µm
Lc               0.800 mm
Ra               0.255 µm
Rq               0.326 µm
Rz                1.60 µm
RzJ               0.84 µm
Rt                2.27 µm

Rmr list
Rmr( 0.78,5.0)0.0 %
Rmr( 0.00,5.0)5.0 %
Rmr(-1.00,5.0) 95 %
Rmr(-2.00,5.0)100 %

Rdc list
Rdc(5.0, 15) 0.21 µm
Rdc( 20, 80) 0.51 µm
Rdc( 85, 98) 0.40 µm

Rmr curve
Lc               0.800 mm
VER               1.00 µm
HOR                 20 %

R Profile
Lc               0.800 mm
VER               1.00 µm
```

5.30° CH M

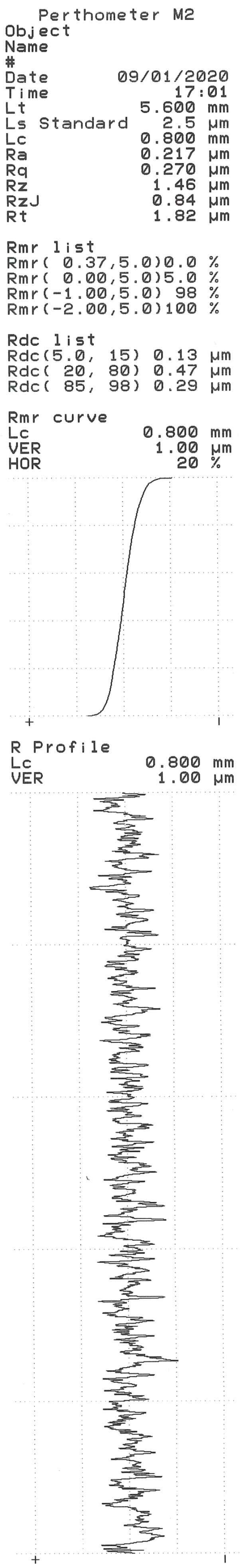

```
   Perthometer M2
Object
Name
#
Date        09/01/2020
Time             17:01
Lt            5.600 mm
Ls Standard     2.5 µm
Lc            0.800 mm
Ra            0.217 µm
Rq            0.270 µm
Rz             1.46 µm
RzJ            0.84 µm
Rt             1.82 µm

Rmr list
Rmr( 0.37,5.0)0.0 %
Rmr( 0.00,5.0)5.0 %
Rmr(-1.00,5.0) 98 %
Rmr(-2.00,5.0)100 %

Rdc list
Rdc(5.0, 15) 0.13 µm
Rdc( 20, 80) 0.47 µm
Rdc( 85, 98) 0.29 µm

Rmr curve
Lc            0.800 mm
VER            1.00 µm
HOR              20 %

R Profile
Lc            0.800 mm
VER            1.00 µm
```

6.15° CH M

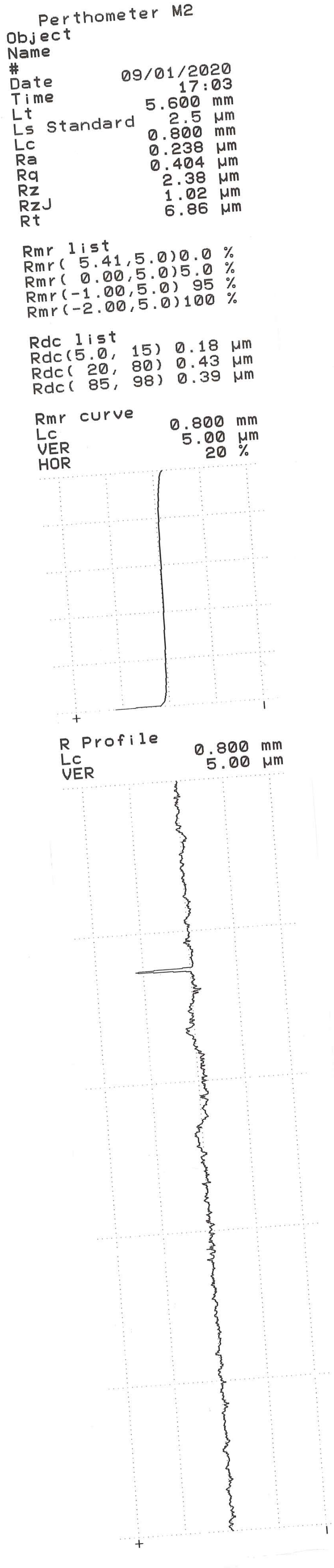

```
   Perthometer M2
Object
Name
#
Date        09/01/2020
Time             17:03
Lt            5.600 mm
Ls Standard     2.5 µm
Lc            0.800 mm
Ra            0.238 µm
Rq            0.404 µm
Rz             2.38 µm
RzJ            1.02 µm
Rt             6.86 µm

Rmr list
Rmr( 5.41,5.0)0.0 %
Rmr( 0.00,5.0)5.0 %
Rmr(-1.00,5.0) 95 %
Rmr(-2.00,5.0)100 %

Rdc list
Rdc(5.0, 15) 0.18 µm
Rdc( 20, 80) 0.43 µm
Rdc( 85, 98) 0.39 µm

Rmr curve
Lc            0.800 mm
VER            5.00 µm
HOR              20 %

R Profile
Lc            0.800 mm
VER            5.00 µm
```

7.0° CH M

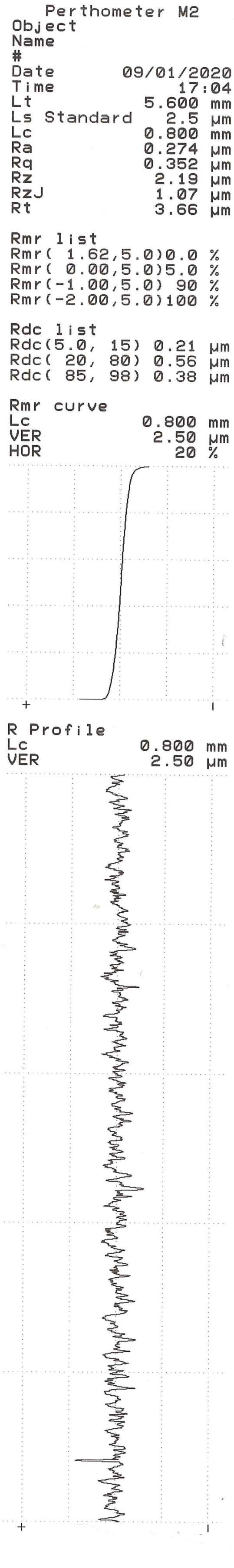

```
   Perthometer M2
Object
Name
#
Date        09/01/2020
Time             17:04
Lt            5.600 mm
Ls Standard     2.5 µm
Lc            0.800 mm
Ra            0.274 µm
Rq            0.352 µm
Rz             2.19 µm
RzJ            1.07 µm
Rt             3.66 µm

Rmr list
Rmr( 1.62,5.0)0.0 %
Rmr( 0.00,5.0)5.0 %
Rmr(-1.00,5.0) 90 %
Rmr(-2.00,5.0)100 %

Rdc list
Rdc(5.0, 15) 0.21 µm
Rdc( 20, 80) 0.56 µm
Rdc( 85, 98) 0.38 µm

Rmr curve
Lc            0.800 mm
VER            2.50 µm
HOR              20 %

R Profile
Lc            0.800 mm
VER            2.50 µm
```

C Test Results

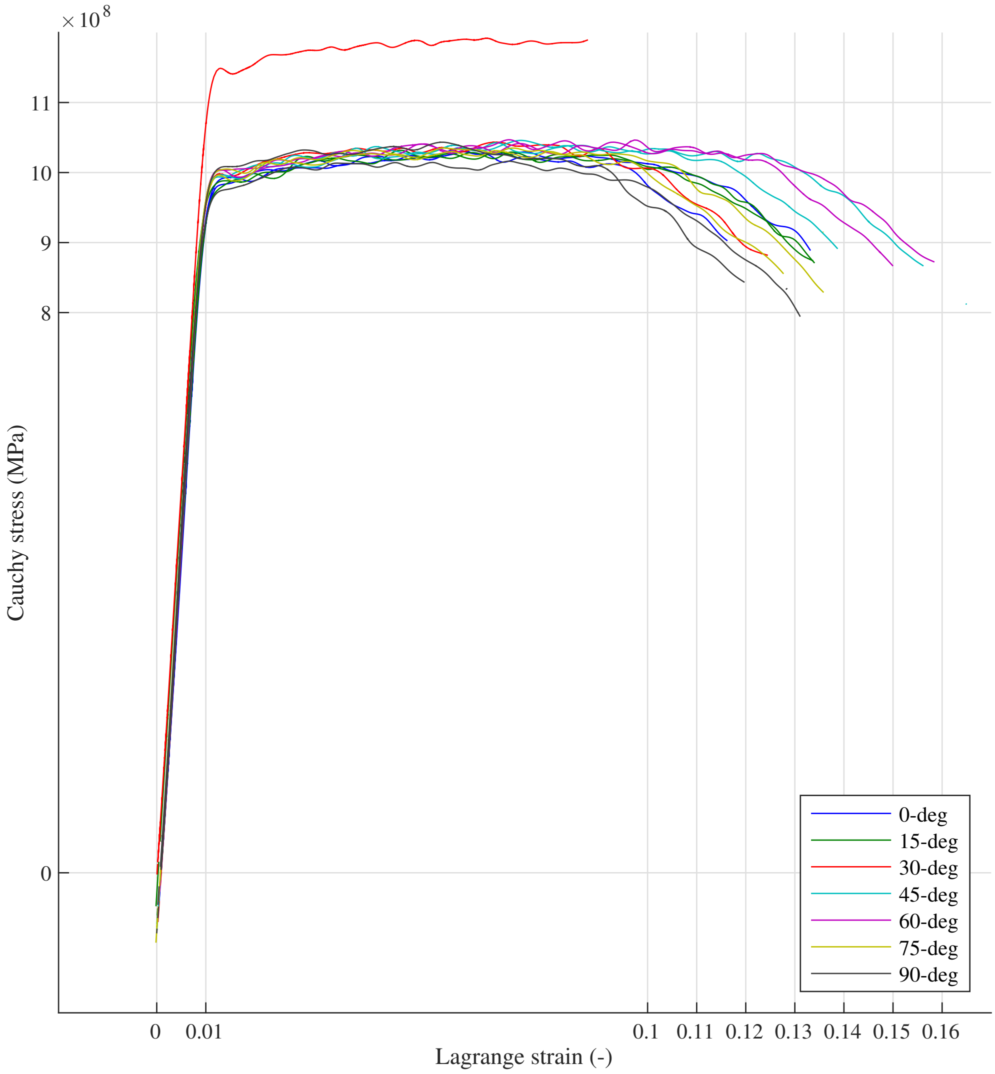

Figure 6.1: Cauchy stress plotted against the Lagrange strain for all the tensile specimens, including the 30° specimen which has been excluded from the result section.

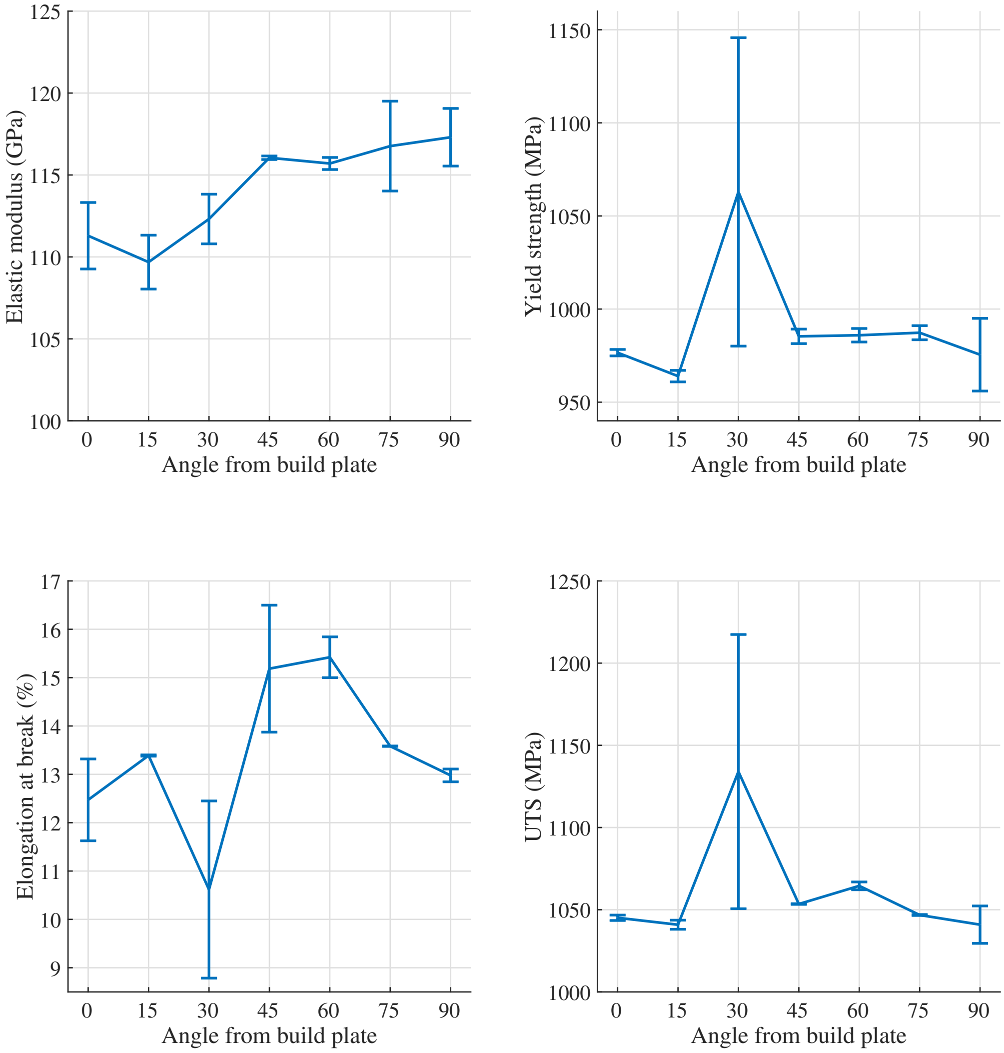

Figure 6.2: Tensile properties plotted with respect to build orientation, including the 30° specimen which has been excluded from the result section.

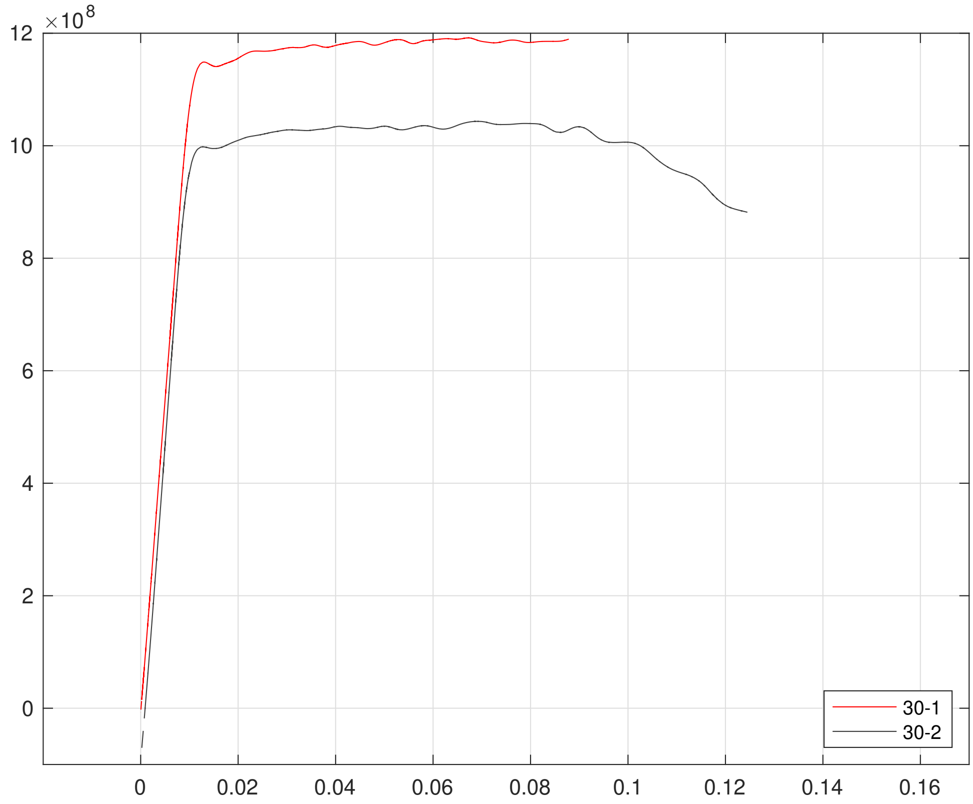

Figure 6.3: Cauchy stress plotted against the Lagrange strain for both 30^{circ} specimens.

NTNU
Norwegian University of
Science and Technology